Copyright

by

Jianhe Guo

2018

The Dissertation Committee for Jianhe Guo Certifies that this is the approved version of the following Dissertation:

High-Performance Artificial Micro/Nanomachines and Their Bioapplications

Committee:

Donglei (Emma) Fan, Supervisor

Paulo Jorge Ferreira

Brian Korgel

Desiderio Kovar

Arumugam Manthiram

High-Performance Artificial Micro/Nanomachines and Their Bioapplications

by

Jianhe Guo

Dissertation

Presented to the Faculty of the Graduate School of
The University of Texas at Austin
in Partial Fulfillment
of the Requirements
for the Degree of

Doctor of Philosophy

The University of Texas at Austin
August 2018

Dedication

This dissertation is dedicated to my wife, Jing Liu,
my parents, Jianmin Guo and Shuzhen Lin,
my grandparents, Jinbang Guo and Yajin Huang,
for their constant support and unconditional love.

Acknowledgements

First and foremost, I would like to express my sincere gratitude and appreciation to my supervisor Dr. Donglei Fan. Thanks to her creative inspirations in generating ideas, valuable suggestions in solving problems, patient guidance in revising writings, and constant support in recommending me for awards/fellowships to ensure my funding, without which it would have never been possible for me to complete my graduate study. She has also shown a lot of grace and support to me beyond research, such as treating us with delicious food on festivals, and helping me find jobs upon graduation. As a scientist and researcher, she is a combination of beauty, integrity, talent and diligence that I rarely see in others. I am very fortunate to be one of her Ph.D. students. In addition, I wish to acknowledge all my colleagues in Dr. Fan's lab: Kwanoh Kim, Xiaobin Xu, Chao Liu, Wesker Lei, Weigu Li, Zexi Liang, Yun Huang, Andrew Chan, Jeremie Gallegos, and Ashley Tom. Both Kwanoh and Xiaobin offered much help in cooperation during the early days when I was still adjusting to the research environment. Thanks to the contributions of Andrew, Jeremie, and Ashley in my research works, who are the best undergraduate students I have worked with. Special thanks to Chao for being my best friend at UT.

My research was supported by Howard Hughes Medical Institutes (HHMI) International Student Research Fellowship, Welch Foundation (F-1734) and National Science Foundation (CMMI 1150767, EECS 1710922, EECS 1446489).

I am also very grateful to my dissertation committee members: Dr. Paulo Jorge Ferreira, Dr. Brian Korgel, Dr. Desiderio Kovar, and Dr. Arumugam Manthiram, for their valuable time and advice to improve my dissertation.

Finally, but by no means least, I would like to thank my family for their infinite love, which is the most important support through my graduate study. Thanks to my parents, who are always with me in whatever I pursue. Thanks to my wife, who is my perfect partner in both life and research.

Abstract

High-Performance Artificial Micro/Nanomachines and Their Bioapplications

Jianhe Guo, Ph.D.
The University of Texas at Austin, 2018

Supervisor: Donglei (Emma) Fan

Artificial micro/nanomachines are micrometer or nanometer scale mechanical devices that convert diverse energy sources into controlled mechanical motions. The development and applications of these micro/nanomachines are among the most pressing challenges in the research field of nanoscience and nanotechnology.

In this dissertation, we report innovative designs and operations of artificial micro/nanomachines for bioapplications in biochemical sensing, biomolecule capture, drug delivery and release. Based on the electric tweezers, innovative rotary nanomotors are bottom-up assembled with high efficiency from nanoscale building blocks, which are massively fabricated and less than 1 μm in all dimensions. After assembling, the rotary nanomotors achieve an ultrafast speed up to 18,000 rpm, an ultradurable operation lifetime of 80 hours, and over 1.1 million rotation cycles. To explore diverse alternative energy inputs for nanomotors, we also applied electric tweezers in the guided manipulation of chemical nanomotors: the motions of chemical nanomotors are aligned along the direction of AC electric fields and their speeds are modulated by the DC electric fields. The prowess of the manipulation of chemical nanomotors by the electric tweezers is demonstrated for applications in cargo delivery to designated microdocks and assembling of chemical nanomotors for powering rotary nanoelectromechanical system (NEMS) devices. To integrate the function of Raman sensing on the micro/nanomachines, plasmonic nanomotors and bio-photonic-plasmonic micromotors with silver (Ag) nanoparticle coating are designed and fabricated, which provide ultrasensitive detection of biochemicals by Surface-enhanced Raman spectroscopy (SERS). The plasmonic nanomotors are designed with nanoporous superstructures, providing high capacities of drug loading and large numbers of hotspots. The plasmonic nanomotors also actively manipulate molecules and tune the release rate in electric fields due to the induced electrokinetic effect. The bio-photonic-plasmonic micromotors based on biosilica diatom frustules are applied in the capture and detection of DNA molecules, which are significantly accelerated during the rotation of the micromotors. The fundamental mechanism is investigated and attributed to the reduction of Nernst diffusion layer caused by the rotation. The innovations of artificial micro/nanomachines including concept, design, fabrication, manipulation, and bioapplications in this dissertation, are expected to inspire various research areas including NEMS, nanorobotics, microfluidics, biochemical delivery, and diagnostic sensing.

Table of Contents

List of Figures x

Chapter 1: Introduction of artificial micro/nanomachines 1

- 1.1 Manipulation techniques 2
  - 1.1.1 Electric manipulation 2
  - 1.1.2 Magnetic manipulation 5
  - 1.1.3 Optical manipulation 9
  - 1.1.4 Acoustic manipulation 12
  - 1.1.5 Chemical manipulation 16
- 1.2 Bioapplications: biochemical delivery and diagnostic sensing 19

Chapter 2: Rotary nanomotors driven by electric fields 24

- 2.1 Design and assembly of rotary nanomotors from nanoscale building blocks 25
- 2.2 Large-scale fabrication of the nanomotor components 27
- 2.3 Ultrasmall rotary nanomotors 28
- 2.4 Ultrafast rotary nanomotors 30
- 2.5 Ultradurable rotary nanomotors 31
- 2.6 Rotation dynamics during long-term operation 34

Chapter 3: Chemical nanomotors manipulated by the electric tweezers 45

- 3.1 Strategy of manipulation 47
- 3.2 Directional guidance of chemical nanomotors 49
- 3.3 Size-dependence study of chemical nanomotors 55
- 3.4 Speed modulation of chemical nanomotors 58
- 3.5 Reversible collection behaviors of chemical nanomotors 61

3.6 Application I: targeted cargo delivery 63

3.7 Application II: assembly of rotary nanomotors driven by chemical reactions ...66

3.8 Conclusions..69

Chapter 4: Plasmonic nanomotors for tunable biochemical release and *in-situ* sensing ...70

4.1 Introduction of surface-enhanced Raman spectroscopy (SERS)........................72

4.2 Design and fabrication of plasmonic nanomotors 72

4.3 Loading capacity of biomolecules on plasmonic nanomotors...........................77

4.4 Characterization and simulation of SERS 78

4.5 Tunable biochemical release from plasmonic nanomotors 84

4.6 Manipulations of plasmonic nanomotors..88

4.7 Conclusions..90

Chapter 5: Bio-photonic-plasmonic micromotors for DNA capture and detection...........92

5.1 Introduction..92

5.2 Design and fabrication of bio-photonic-plasmonic micromotors.......................94

5.3 Characterization and simulation of SERS 96

5.4 Magnetic manipulation and individual self-assembly of micromotors 98

5.5 Mechanically accelerated capture and detection of DNA molecules...................102

5.6 Conclusions..111

Chapter 6: Conclusions..113

Appendix: List of publications..114

References..117

Vita..148

List of Figures

Figure 1.1: Electric tweezers. (a-c) Illustration and (d-f) overlaid sequential optical images of translational motions of nanowires in combined AC and DC electric fields with different configurations, *i.e.*, (a and d) AC ∥ DC, (b and e) AC ⊥ DC, or (c and f) DC only. Reproduced with permission.[8] Copyright 2008, AIP Publishing LLC. 3

Figure 1.2: Magnetic tweezers. (a-b) Magnetic manipulation based on magnetic gradients with (a) horizontally aligned magnetic moments and (b) vertically aligned magnetic moments, respectively. (c) Magnetic manipulation based on magnetic torques. Reproduced with permission.[22] Copyright 2016, Sarkar and Rybenkov, Frontiers Media. 6

Figure 1.3: Magnetically actuated micro/nanomachines. (a) Transport of a magnetic microsphere and rotation of assembled microspheres. Reproduced with permission.[27] Copyright 2002, Elsevier. (b) Scanning electron microscopy (SEM) images and trajectories of nanoswimmers in cork-screw-like motions. Reproduced with permission.[31] 2009, American Chemical Society. (c) Schematic diagrams of flexible nanowire nanomotors moving forward (top) or backward (bottom) in flexible-oar-like motions. Reproduced with permission.[17] Copyright 2010, American Chemical Society. (d) Linear transport of a magnetic nanowire rotating near a vertical wall. Reproduced with permission.[24] Copyright 2010, American Chemical Society.. 8

Figure 1.4: Schematic diagrams of manipulation mechanisms of optical tweezers. (a-b) For particles of sizes in the Mie scattering regime, the refraction of non-uniform light by the particles generates a net force along the optical field gradient towards the highest optical intensity. (c) The reflection of light results in a radiation pressure along the laser beam axis. (d) For particles with Rayleigh scattering, the electric force on light-induced electric dipoles in the particles compel the particles to transport along the gradient towards the highest electric field. Reproduced with permission.35 Copyright 2008, Royal Society of Chemistry. 10

Figure 1.5: Optical manipulation of micro/nanoentities. (a) Nanowire manipulated by optical traps. Reproduced with permission.[39] Copyright 2006, Nature Publishing Group. (b) The principle of torque generation by linear light momenta. Reproduced with permission.[40] Copyright 1997, AIP Publishing LLC. (c) Schematic of a structurally birefringent microgear driven by transfer of spin angular momentum. Reproduced with permission.[46] Copyright 2005, Nature Publishing Group. (d) Generation of helical light modes carrying orbital angular momentum, and the trapping and rotation of microparticles by transfer of orbital angular momentum. Reproduced with permission.[47] Copyright 2003, Nature Publishing Group. 12

Figure 1.6: Acoustic tweezers. (a) Schematic of the standing surface acoustic waves based patterning design of IDTs. Top: one-dimensional patterning using two parallel IDTs. Bottom: two-dimensional patterning using two orthogonal IDTs. Reproduced with permission.[50] Copyright 2009, Royal Society of Chemistry. (b) Schematics of device structure and working mechanism of the four-IDTs acoustic tweezers. Bottom: a standing surface acoustic wave field generated by driving chirped IDTs at two different frequencies. Reproduced with permission.[51] Copyright 2012, Proc. Natl. Acad. Sci. USA. 14

Figure 1.7: Various movement modes of ultrasound-propelled nanomotors: (a) schematic and (d) optical images of chain assembly and axial rotation; (b-c) directional motion, in-plane rotation and pattern formation, respectively. Inset: SEM image of asymmetric nanorods with one of the tips concaved. Reproduced with permission.[54] Copyright 2012, American Chemical Society. 15

Figure 1.8: Schematic of chemical manipulations based on (a) self-electrophoretic mechanism, and (b) bubble recoil mechanism, respectively. 17

Figure 1.9: Direction control on chemical micro/nanomotors. (a-b) Control based on magnetic tweezers: (a) schematics of the distribution of magnetic moments and the deterministic motion of the Janus nanomotor guided by an external magnetic field; (b) on/off controlled motion of the Janus nanomotor. Reproduced with permission.[68] Copyright 2012, American Chemical Society. (c-d) Control based on acoustic tweezers: (c) schematics of acoustic device and the alignment of nanomotors; (d) demonstration of aligned motion of two nanomotors that have different initial orientation. Reproduced with permission.[69] Copyright 2017, American Chemical Society. 18

Figure 1.10: (a) Schematic and overlapped optical images of nanowires precisely transported onto a selected cell following prescribed trajectory using electric tweezers. Reproduced with permission.[7] Copyright 2011, Elsevier. (b) A helical magnetic microswimmer (i) approaching, (ii) capturing, (iii, iv) transporting, and (v) dropping off targets in DI water. The microswimmer moved between the regions A and B with step height. The inset SEM image shows the structure of the helical microswimmer with the cargo holder. Reproduced with permission.[19] Copyright 2012, Wiley-VCH. 21

Figure 1.11: (a) Schematic diagram of motion-based nucleic acid detection relying on the silver-induced speed enhancement. Reproduced with permission.[85] Copyright 2010, Macmillan Publishers Limited. (b) Illustration of the acoustically propelled nanomotors for single-cell real-time miRNA detection. Reproduced with permission.[88] Copyright 2015, American Chemical Society. (c-d) Schematic of plasmonic-active nanocapsules assembled in order arrays by electric tweezers for SERS detection. Reproduced with permission.[89] Copyright 2012, Wiley-VCH. (e) Overlaid microscopic images of a plasmonic nanocapsule transported to a live cell by magnetic manipulation. (f) Raman spectrum of the cell membrane detected from the plasmonic nanocapsule. Reproduced with permission.[90] Copyright 2013, Wiley-VCH. 22

Figure 2.1: (a) Schematic diagram of a rotary nanomotor. (b) Overlapped images of a nanowire rotor transported and assembled on a nanobearing by the electric tweezers. Inset: schematic diagram of electric tweezers manipulating a nanowire rotor. Reproduced with permission.[95] Copyright 2014, Macmillan Publishers Ltd. (c) Sequential optical images of a nanomotor rotating clockwise (CW) and counterclockwise (CCW) every 60 ms. The positions of the bearing are highlighted by red dots. Reproduced with permission.[96] Copyright 2015, Royal Society of Chemistry. 26

Figure 2.2: Fabrication process of (a) multi-segment nanowires as rotors in the rotary nanomotors and (b) multilayer magnetic nanodisks as bearing in the rotary nanomotors. (c-d) SEM images of (c) Au/Ni/Au multi-segment nanowires and (d) magnetic nanobearings. 28

Figure 2.3: (a) SEM images of the as-synthesized Au/Ni/Au nanowires. The Au (bright) and Ni (dark) segments are 350-400nm and 100 nm, respectively. (b-c) Close-up SEM image of (b) a single nanowire and (c) a magnetic bearing. (d) Rotation speed of a nanomotor made of nanowires and magnetic bearings shown in (a-c) *versus* applied electric frequency. (e) Rotation angle as a function of time for both CW and CCW rotation of a nanomotor. Reproduced with permission.[95] Copyright 2014, Macmillan Publishers Ltd. 29

Figure 2.4: Ultrafast rotation. (a) Rotation speed of nanomotors from 10 to 17V at 30 kHz in a 100-mm-gapped quadruple microelectrode. Inset: angle *versus* time of the nanomotor rotating CW with a speed of ~18,000 rpm. (b) Enhanced snapshot images taken every 0.8 ms of the same nanomotor rotating at ~18,000 rpm at 17V and 30 kHz. Reproduced with permission.[95] Copyright 2014, Macmillan Publishers Ltd. 30

Figure 2.5: Rotation speed *versus* time, and SEM images of the as-made nanobearings (top) and the nanobearings after long-term rotation (bottom). inset: schematic diagram of the nanomotors. (a-b) Rotor: Au (350~400 nm)/Ni (100 nm)/Au (350~400 nm), 165 nm in diameter; bearing: 200 nm in diameter, thin-film stack of Au (40 nm)/Ni (80 nm)/Cr (6 nm). Reproduced with permission.[95] Copyright 2014, Macmillan Publishers Ltd. (c-d) Rotor: Au (1.8 μm)/Ni (500 nm)/Au (1.8 μm), 165 nm in diameter; bearing: 500 nm in diameter, thin-film stack of Au (60 nm)/Ni (80 nm)/Cr (6 nm). (e-f) rotor: Au (1.8 μm)/Ni (500 nm)/Au (1.8 μm), 165 nm in diameter; bearing: 500 nm in diameter, thin-film stack of Ti (60 nm)/Cr (6 nm)/Ni (80 nm)/Cr (6 nm). Reproduced with permission.[96] Copyright 2015, Royal Society of Chemistry. 33

Figure 2.6: (a) Average rotation speed *versus* applied voltage^2 for nanowire rotors (wine red) and free suspending nanowires (orange). (b) Rotation speed *versus* angular position at different times and the corresponding Fourier transform showing the primary periodicity. (c) Amplitude of the magnetic and frictional torques *versus* time during the 22.6-hour rotation. Reproduced with permission.[96] Copyright 2015, Royal Society of Chemistry. 35

Figure 2.7: (a) Instant center of rotation of the nanomotor primarily formed at the bottom right corner of the magnetic nanobearing (at 22.6 hours). (b) AFM image obtained by taping mode showing the wear of the magnetic bearing after 22.6-hour rotation. (c) Time-dependent change of the thickness of the Au spacer layer determined from the evolving magnetic torque during the rotation. (d) Log-log plot of the amplitude of frictional torque *versus* that of the magnetic force showing a power dependence of ~1 (slope of the plot). Reproduced with permission.[96] Copyright 2015, Royal Society of Chemistry.. 40

Figure 2.8: (a) Time-dependent change of the thickness of the Ti spacing layer determined from the magnetic torque during rotation of the nanomotor, insert: the amplitude of the angle-dependent magnetic torque *versus* time. (b) Log-log plot of the amplitude of frictional torque *versus* that of the magnetic force showing a power dependence of ~1 (slope of the plot). Reproduced with permission.[96] Copyright 2015, Royal Society of Chemistry. 42

Figure 3.1: (a) Schematic diagram of 3D manipulations of Pt-Au chemical nanomotors in H_2O_2 fuel with AC E-fields. (b) SEM and (c) EDS images of Pt-Au chemical nanomotors (250 nm in diameter, 5 μm in length; consisting of 2-μm Pt segment and 3-μm Au segment). (d) Overlapped snapshots of a chemical nanomotor guided by AC E-fields. Reproduced with permission.[145] Copyright 2018, American Chemical Society.. 47

Figure 3.2: Scheme of 3-D orthogonal microelectrode setup. Reproduced with permission.[145] Copyright 2018, American Chemical Society. 48

Figure 3.3: (a) Speed of chemical nanomotors *versus* concentration of H_2O_2 with/without AC E-fields (5 MHz, 15 V). (b) Speed *versus* peak-to-peak voltage of AC E-fields (500KHz) in 7.5 wt% H_2O_2 solution. Reproduced with permission.[145] Copyright 2018, American Chemical Society. 50

Figure 3.4: (a-e) Angular velocity (ω) of nanomotors *versus* angle (θ) during the alignments at different AC frequencies. (f) Speed *versus* frequency of AC E-fields (20 V) in 7.5 wt% H_2O_2 solution. Inset: electric torque *versus* frequency of AC E-field. Reproduced with permission.[145] Copyright 2018, American Chemical Society. 52

Figure 3.5: Angular velocity (ω) *versus* angle (θ) during the alignment of nanomotors by a AC *E*-field of 20 V and 500 KHz at different NaCl media. Reproduced with permission.[145] Copyright 2018, American Chemical Society. 53

Figure 3.6: The Zeta potential measurement of Pt-Au nanorod chemical nanomotors of different lengths in DI water. The measurements were conducted by Dynamic Light Scattering Zetasizer Nano ZS, Malvern. The size range is from 1 nm to 5 μm. The Zeta potentials for nanomotors with lengths of 0.82, 2.50 and 4.78 μm are -31.28±6.64 mV, -28.50±5.03 mV and -31.77±4.43 mV, respectively. Reproduced with permission.[145] Copyright 2018, American Chemical Society.. 55

Figure 3.7: SEM (left) and EDS (right) images of chemical nanomotors of different lengths. Reproduced with permission.[145] Copyright 2018, American Chemical Society. 56

Figure 3.8: (a) Trace of chemical nanomotors of different length in 7.5 wt% H_2O_2 solution with AC E-fields (5 MHz, 15 V) in 2 seconds. The lengths of nanomotors (from right to left) are 0.82, 2.50, 4.78, 6.68 and 8.96 μm, respectively. The green dashed line shows the starting position. (b) Log-log plot of speed *versus* length of nanomotors in (a). The slope is -0.98. Reproduced with permission.[145] Copyright 2018, American Chemical Society. 57

Figure 3.9: (a) Speed of Au nanorods and Pt-Au chemical nanomotors of same dimensions *versus* DC E-fields in different suspension mediums. (b) Zeta potentials of Au nanorods and Pt-Au chemical nanomotors in different suspensions. Reproduced with permission.[145] Copyright 2018, American Chemical Society. 59

Figure 3.10: Reversible collection and dispersion behaviors of chemical nanomotors. (a) Autonomous motion of nanomotors before AC electric fields are applied. (b) Rapid attraction and assembly of nanomotors when AC electric fields are on. (c) Re-dispersion after turning off AC electric fields. Applied AC field is 50 KHz and 10 Vpp, and the concentration of H_2O_2 is 7.5 wt%. Top: 10 μm×50 μm microislands arrays with 20 μm and 50 μm gaps in X and Y directions, respectively. Bottom: 10 μm×120 μm microislands arrays with 20 μm and 50 μm gaps in X and Y directions, respectively. Scale bar: 100 μm. 62

Figure 3.11: (a) Scheme of targeted cargo delivery. (b-f) Optical microscopy images show the dynamic process of a Pt-Au chemical nanomotor when picking up, pushing, and delivering a nanorod cargo to the designated microdock. (g) Speed of the nanomotor in the cargo delivery process. Reproduced with permission.[145] Copyright 2018, American Chemical Society. 64

Figure 3.12: (a) Schematic diagram of the rotary NEMS device with chemical nanomotor assembled as the powering component. (b) SEM images of the multi-segment nanowire rotor. The segments from left to right are 200 nm Au, 50 nm Ni, 3.5 μm Au, 500 nm Ni, 3.5 μm Au, 50 nm Ni and 200 nm Au. (c-d) SEM and EDS images of the Pt-Ag/Au chemical nanomotor. The segments from left to right are 400 nm Au, 1.7 μm Ag-Au alloy, 500 nm Ni, 400 nm Au, and 2 μm Pt. (e) Overlapped snapshots showing the assembling process of a chemical nanomotor on a rotary NEMS device. Reproduced with permission.[145] Copyright 2018, American Chemical Society. 66

Figure 3.13: (a) Snapshots of a rotating NEMS device driven by a chemical nanomotor taken every 2 seconds. (b) Rotation angle *versus* time of the rotating NEMS device. (c) Rotation speed *versus* time of the rotating NEMS device. Reproduced with permission.[145] Copyright 2018, American Chemical Society. 68

Figure 4.1: Flowchart of the fabrication process of the nanoporous superstructural plasmonic nanomotors. Reproduced with permission. Copyright 2018, American Chemical Society. 73

Figure 4.2: SEM images of (a) Au nanorod with a silica nanoshell. (b) Assembling of the first layer of PS nanospheres on the Au/silica core-shell nanostructure. (c) Assembling of the second layer of PS nanospheres on the Au/silica core-shell nanostructure. (d) 3D nanoporous superstructure with large arrays embedded nanocavities. (e) Ag-nanoparticles on the outer surface of the superstructure. (f) Cross-sectional view of the superstructure with Ag nanoparticles in the embedded nanocavities arranged in two concentric nanorings. (g) Close-up view of a few nanocavities with filled Ag nanoparticles (in pseudocolor) of narrow junctions of a few nanometers. Reproduced with permission. Copyright 2018, American Chemical Society. 74

Figure 4.3: Size distribution of (a) Ag nanoparticles and (b) nanojunctions between them. Reproduced with permission. Copyright 2018, American Chemical Society. 76

Figure 4.4: (a) Fluorescence spectra and (b) average fluorescent intensity of R-6G molecules obtained from the porous Au/silica nano superstructures, solid control samples and natively oxidized silicon substrate. Reproduced with permission. Copyright 2018, American Chemical Society. 77

Figure 4.5: SERS spectra of R-6G molecules of different concentrations determined from the porous superstructural plasmonic nanomotors (a) and the control samples made of solid plasmonic nanomotors (b). Inset in (b): SEM image of the control samples. Reproduced with permission. Copyright 2018, American Chemical Society. 79

Figure 4.6: SERS spectra of BPE molecules with different concentrations detected from the porous plasmonic nanomotors. Reproduced with permission. Copyright 2018, American Chemical Society. 79

Figure 4.7: (a) Raman spectrum of 1 M BPE in ethanol solution (integration time 10 seconds). SERS spectra on (b) solid and (c) porous plasmonic nanomotors with saturated adsorption of BPE, respectively (integration time 5 seconds). Reproduced with permission. Copyright 2018, American Chemical Society. 80

Figure 4.8: (a-c) Simulations of the electric field distribution in (a) a nanoporous superstructural plasmonic nanomotors, (b) a solid plasmonic nanomotors, and (c) a porous superstructural plasmonic nanomotors without Ag nanoparticles in the second layer of embedded nanocavities. The 532-nm laser is in the vertical direction with an in-plane polarization. (d) Optical image of a porous plasmonic nanomotor and (e) Raman mapping of R-6G (10^{-6} M, 1644 cm^{-1}). (f) Intensity of Raman signals along the length of the porous plasmonic nanomotor in (d). Reproduced with permission. Copyright 2018, American Chemical Society. 82

Figure 4.9: Finite Element Modeling with COMSOL: (a) electric field distribution around a pair of Ag nanoparticles and attraction of molecules towards the location with the highest electric field. (b) The distribution of electromagnetic field due to an incidental laser around a pair of Ag nanoparticles. The laser is in the vertical direction with an in-plane polarization. Reproduced with permission. Copyright 2018, American Chemical Society. 84

Figure 4.10: (a) Raman intensities of Nile Blue (595 cm^{-1}) at different concentrations detected from the plasmonic nanomotors. (b) Linear dependence of Raman intensity on concentrations of Nile Blue from 25 nM to 500 nM. Reproduced with permission. Copyright 2018, American Chemical Society. 85

Figure 4.11: (a) Release rate of NB from plasmonic nanomotors at different AC frequencies. (b) Raman detection of the release of NB molecules with time in an external electric field of 50V, 50- 400 kHz. Reproduced with permission. Copyright 2018, American Chemical Society. 86

Figure 4.12: (a) Voltage-dependent release rate *versus* applied voltage at 200 kHz and (d) Raman detection of the release of NB molecules with time in an external electric field of 0 to 75 V, 200 kHz. Reproduced with permission. Copyright 2018, American Chemical Society. 87

Figure 4.13: (a) Intensity of Raman spectra of adenine at 720 cm^{-1} at different concentrations detected from the plasmonic nanomotors. (b) Raman intensity of adenine is linearly proportional to concentration from 0 to 500 nM. (c) Raman detection of release of adenine molecules *versus* time when an AC electric field of 500KHz 50V is turned on and off. Reproduced with permission. Copyright 2018, American Chemical Society. 88

Figure 4.14: (a) Schematic of a plasmonic nanomotor manipulated by the electric tweezers. (b) Transport speed of a plasmonic nanomotor *versus* applied DC voltage. (c) Overlapped snapshots of a plasmonic nanomotor transported along the letter "U". (d) Rotation angle profile at different AC electric field voltages (50 KHz), inset: overlapped snapshots. (e) Rotation speed *versus* frequencies of AC electric fields (14V). (f) Rotation speed *versus* the square of applied voltages (50 KHz). Reproduced with permission. Copyright 2018, American Chemical Society. 89

Figure 5.1: (a) Schematic of a rotating bio-photonic-plasmonic micromotor in DNA solutions. (b-d) SEM images of the porous periodic microstructure of diatom frustule at (b) low magnification and (c) high magnification, and (d) Ag nanoparticles synthesized on the surface. 94

Figure 5.2: (a) SERS spectra of DNA from 80 nM to 4 μM. (b) Raman mapping of DNA (4 μM, 724 cm^{-1}) on a micromotor after 2-hour incubation. (c) SERS spectra of 4 μM DNA on a micromotor (blue) and on a Ag-nanoparticle coated flat glass substrate (green), respectively. (d) Simulations of electric field distributions around a pair of Ag nanoparticle dimer placed on a diatom frustule substrate (top) and a flat glass substrate (bottom), respectively. Insets are the schematics of the simulated structures with Ag nanoparticles highlighted. The out-plane incident laser is polarized horizontally. 97

Figure 5.3: Schematic of the experimental setup for robotization. 98

Figure 5.4: (a) Magnetic field strength (*B*) *versus* the distance (*d*) between permanent magnet on magnetic stirrer and micromotors. (b) Rotation angle *versus* time at different rotation speed. 99

Figure 5.5: (a) Snapshots of a micromotor rotating and self-assembling into a microwell. First 5 snapshots are taken every 1 second and others are taken every 0.05 second. (b) Snapshots of a micromotor rotating in a microfluidic channel every 0.025 second. (c) Snapshots of a micromotor rotating at 300 rpm and passing by an occupied microwell every second. Scalebar in all is 30 μm. 101

Figure 5.6: Simulation of the fluidic fields around two approaching micromotors rotated at (a) 0˚ (end by end), (b) 45˚, (c) 90˚ (side by side), and (d) 135˚, respectively. 102

Figure 5.7: Raman intensity of DNA at 724 cm^{-1} *versus* DNA concentration. 104

Figure 5.8: Capture dynamics of DNA revealed by SERS on (a) a static micromotor and (b-f) rotating micromotors at 60-1200 rpm, respectively. 105

Figure 5.9: Time needed to attain 95% of the final equilibrium DNA capture *versus* rotation speed of micromotors. 106

Figure 5.10: Schematic model of the DNA capture dynamics including convection, diffusion and adsorption. 107

Figure 5.11: Capture dynamics of DNA at different temperatures: DNA concentrations in bulk solution *versus* time measured by UV spectroscopy. 109

Figure 5.12: Log-log plot of capture rate (k) *versus* rotation speed (ω in rpm) of micromotors. The orange dash line is the linear fitting of data ranging from 60 rpm to 300 rpm. 110

Figure 5.13: Raman spectra of DNA (80 nM) measured at premeditated moments in an hour after mixing on both static and rotating micromotors at a rotation speed of 630 rpm. 111

Chapter 1: Introduction of artificial micro/nanomachines*

Artificial micro/nanomachines are mechanical devices ranging from micrometer to submicrometer scale that can harness power from various types of energy sources to generate mechanical motion in a controlled manner.[1-2] The concept of miniaturizing conventional machines to such a small scale has greatly fascinated the research community. Although biological systems in nature have created sophisticated molecular machines that could work within cells, *e.g.*, myosin, kinesin, dynein, and other motor proteins, for many years, artificial micro/nanomachines had been largely imagined in science fiction movies from Fantastic Voyage in the 1960s to the recent Ant-Man. The difficulties in creating artificial micro/nanomachines lie in their small scale. It not only makes the fabrication and assembling of machine components extremely arduous but also presents new challenges that are not encountered in the macroscopic world. For instance, micro/nanoscale objects are often suspended in liquid, such as water suspension, to avoid adhesion when directly contacting solid substrates. However, due to the small sizes, the micro/nanoobjects are often subjected to low Reynolds number in liquids, where viscous forces dominate over inertial forces. It is extremely challenging to robotize and manipulate micro/nanoobjects.[3-4] Over the past decades, different working mechanisms have been explored to power and manipulate artificial micro/nanomachines with a variety of energy sources such as electrical field, magnetic field, optical field, ultrasonic wave, and chemical reaction in the environment.

---

* Portions of this chapter have been previously published in K. Kim, **J. Guo**, X. Xu, D. Fan, Small, 11, 4037 (2015); K. Kim, **J. Guo**, Z. Liang, D. Fan, Advanced Functional Materials, 28, 1705867 (2017). As the second author of both invited reviews, J. Guo reviewed recent advances in artificial micro/-nanomachines and wrote the drafts of several chapters. K. Kim led the writing. As the faculty author, Professor D. Fan supervised the projects, conceived the outlines and revised the review articles.

1.1 MANIPULATION TECHNIQUES

1.1.1 Electric manipulation

Micro/nanomachines can be robotized and manipulated by direct current (DC) and alternating current (AC) electric fields in the range of KHz to MHz generated *via* patterned microelectrodes. Micro/nanoentities suspended in a liquid medium can be transported by DC electric fields due to electrophoretic (EP) effect, moved with liquid flow due to the electroosmotic (EO) effect in a DC or low-frequency AC electric field (<10 KHz), and translocated due to the interaction between the electrically polarized micro/nanoentities and non-uniform high frequency electric field (10 KHz to 10 MHz), so-called dielectrophoretic (DEP) effect.[5-7]

The phenomena of EP and EO effects rely on the formation of electric double layer (EDL) at the solid/liquid interface due to local charging. An external electric field (E) can drive the ions in the EDL and thus drag the surrounding fluid. The resultant fluid flow, known as EO flow, has a slip velocity (v_{EO}) given by the Helmholtz-Smoluchowski equation in thin-double-layer limit:[5]

$$\boldsymbol{v}_{EO} = -\frac{\varepsilon_m \zeta}{\eta}\boldsymbol{E} \qquad (1.1)$$

where ε_m and η are the dielectric constant and viscosity coefficient of the liquid media, respectively, and ζ is the zeta potential. Here zeta potential is defined as the electrokinetic potential difference between the liquid media and the stationary layer in EDL. The surface EO flow in one direction will give rise to motion of the micro/nanoentities in the opposite direction, generating EP effect. Therefore, regardless of shape and size of the micro/nanoentities, the EP velocity (v_{EP}) is given by Smoluchowski's equation as:[5]

$$\boldsymbol{v}_{EP} = \frac{\varepsilon_m \zeta}{\eta}\boldsymbol{E} \qquad (1.2)$$

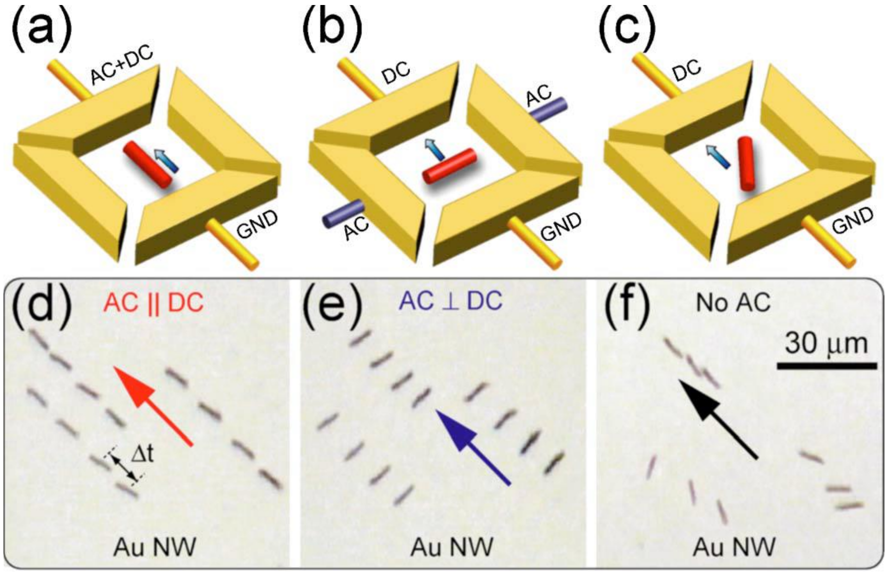

Figure 1.1: Electric tweezers. (a-c) Illustration and (d-f) overlaid sequential optical images of translational motions of nanowires in combined AC and DC electric fields with different configurations, *i.e.*, (a and d) AC ∥ DC, (b and e) AC ⊥ DC, or (c and f) DC only. Reproduced with permission.[8] Copyright 2008, AIP Publishing LLC.

In the interaction between the dipoles induced in the micro/nanoentities and a non-uniform electric field, the forces acting on the two poles are not the same due to the gradient in the electric field. This leads to the emergence of DEP effect. Therefore, the DEP force on the induced dipole moment is proportional to the electric field gradient:[5]

$$F_{DEP} = (p \cdot \nabla)E = 3\varepsilon_m V Re(K)(E \cdot \nabla)E = \frac{3}{2}\varepsilon_m V Re(K)\nabla E^2 \qquad (1.3)$$

where $p = 3\varepsilon_m V Re(K) E$ is the effective induced dipole moment of micro/nanoentities, V is the volume of micro/nanoentities, and $Re(K)$ is the real part of the Clausius-Mossotti factor K. The Clausius-Mossotti factor is defined as:[5]

$$K = \frac{\varepsilon_p^* - \varepsilon_m^*}{\varepsilon_m^* + L_i(\varepsilon_p^* - \varepsilon_m^*)} \qquad (1.4)$$

where ε_m^* and ε_p^* are the frequency dependent dielectric constant of the media and micro/nanoentities, respectively, and L_i is the depolarization factor. If micro/nanoentities are more polarizable than the media ($Re(K) > 0$), they will move along the gradient into the areas of highest field intensities, generating positive DEP effect. On the contrary, micro/nanoentities that are less polarizable than the media ($Re(K) < 0$) are pushed away from these areas, generating negative DEP effect. DEP phenomena usually occur in AC electric fields at high frequency, which circumvent the screening effect of water.

Although the aforementioned effects can transport nanoparticles, their applications towards assembling and powering nanomachines have been largely restricted by the limited versatility in manipulation.[9-10] For instance, DEP effects can transport nanoparticles in a pre-set direction along an electric field gradient, but it is arduous to alter the moving direction once the electrodes are fixed.[11] Therefore, the interaction of the dipoles induced in the micro/nanoentities with electric fields has been most useful for aligning and positioning micro/nanoentities or separating and sorting cells rather than transporting or actuating micro/nanomachines.[12] Recently Fan *et al.* reported a unique approach, electric tweezers, to manipulate nanoentities with combined DC and AC electric fields in quadruple microelectrodes, demonstrating highly efficient and fully controlled manipulations of longitudinal nanoentities in two dimensions(Figure 1.1).[8, 13] The electric tweezers utilize EP and EO effects to transport the nanoentities in a DC electric field, and the interaction of the induced dipoles with electric fields to align the nanoentities in their long direction in an AC electric field. Note that, in the case of a uniform AC electric field where the average field gradient is zero, there is no DEP force. However, the electric field still generates an electric torque, which compels the micro/nanoentities to rotate and align its longitudinal axis with the field. Therefore, by strategically applying DC and AC electric fields, one can not only transport micro/nanoentities along prescribed trajectories with defined alignment, but also rotate nanoparticles with the controlled angle, speed, and chirality. Such high versatility makes the electric tweezers highly suitable for the manipulation and actuation of nanoentities for various applications.

1.1.2 Magnetic manipulation

The micro/nanomanipulation technique actuated by magnetic fields is usually referred to magnetic tweezers, which was first demonstrated by applying magnetic fields to drag and twist magnetic particles for studying physical properties of cytoplasm in 1950.[14] Within magnetic fields, paramagnetic or ferromagnetic micro/nanoentities can be driven to align, transport, drag, and rotate in three dimensions.[15-21] Owing to their commercially available setup, commonsensible mechanisms, and advantageous biocompatibility, magnetic fields activated micro/nanorobots hold considerable promise for biomedical applications. Based on the mechanisms, magnetic actuation of micro/nanoentities are usually categorized into gradient-driven manipulations (non-uniform magnetic field), and torque-driven manipulations (both uniform and non-uniform magnetic field).[22]

The principle of magnetic tweezers has a large similarity to that of the interaction between electric induced dipole moment and electric fields, where the magnetic micro/nanoentities of interest are aligned in the direction of the magnetic field and transported by the magnetic field gradient due to interactions between the magnetic dipoles of the micro/nanoentities and the field generated by the magnetic tweezers. Magnetic micro/nanoentities in a non-uniform external magnetic field ($\boldsymbol{B}$) receives a force proportional to field gradient, which is given by:[22-23]

$$F_{mag} = (\boldsymbol{m} \cdot \nabla)\boldsymbol{B} \qquad (1.5)$$

where $\boldsymbol{m}$ is the magnetic moment of the micro/nanoentities. As a result, magnetic micro/nanoentities would move towards the region of the strongest gradient [Figure 1.2(a-b)]. The magnetic field gradient is inversely proportional to the distance, resulting in the force applied on the magnetic particles as a function of the displacement. In additional to the magnetic force, magnetic particles in a magnetic field (no matter it is uniform or not) also experience an alignment torque ($\boldsymbol{\tau}_{mag}$) given by:[23-24]

$$\boldsymbol{\tau}_{mag} = \boldsymbol{m} \times \boldsymbol{B} \qquad (1.6)$$

which tends to align the micro/nanoentities with magnetic field [Figure 1.2(c)].

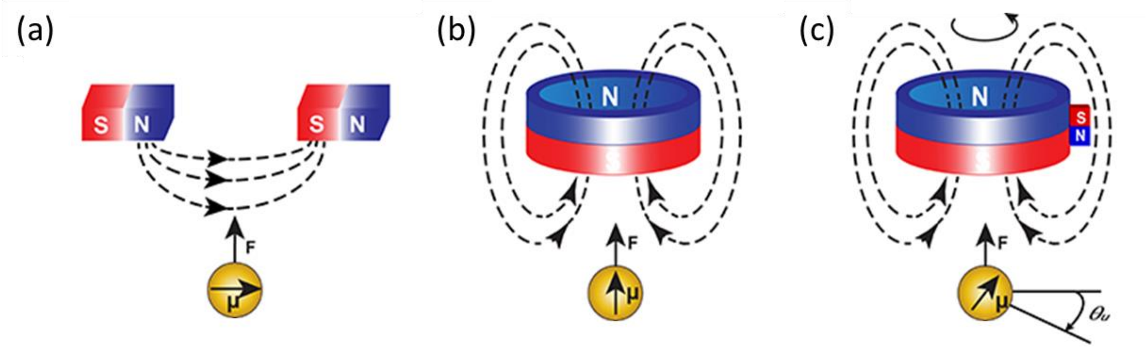

Figure 1.2: Magnetic tweezers. (a-b) Magnetic manipulation based on magnetic gradients with (a) horizontally aligned magnetic moments and (b) vertically aligned magnetic moments, respectively. (c) Magnetic manipulation based on magnetic torques. Reproduced with permission.[21] Copyright 2016, Sarkar and Rybenkov, Frontiers Media.

The magnetic fields can be generated from either permanent magnets or electromagnets.[25] However, permanent magnets are less often used compared to electromagnets, which can turn on, turn off, and vary the magnitude of the applied force. By strategically applying the magnetic force and torque within three pairs of independently controllable electromagnets, Gosse *et al.* demonstrated the manipulations of microparticles in arbitrary direction such as moving along trajectories of letters and rotating with controlled angles [Figure 1.3(a)].[26] Since it is not viable to generate strong magnetic field gradients over a wide distance, uniform magnetic fields are more often applied to enable the orientation and transport of micro/nanoentities.[24, 27] Inspired by swimming strategies of living microorganisms at low Reynolds numbers, researchers employ rotating uniform magnetic field to actuate motions of micro/nanoentities in three behaviors: cork-screw-like motions, flexible-oar-like motions, and surface-assisted motions. Cork-screw like motions of micro/nanorobots [Figure 1.3(b)] with spiral structures are most widely investigated in manipulation driven by magnetic fields.[28-30] The magnet moment of the magnetic helices strongly couples with the rotating magnetic field, and thus the spiral structures rotate in synchrony with the rotation of external field. The rotation generates forward or backward thrust perpendicular to the rotary plane. The translational behaviors such as orientation and velocity not only depend on the direction, frequency, and strength of external rotating magnetic fields, but also correlate to the helicity of spiral structures. The mechanism of flexible-oar-like motions is similar to that of cork-screw-like motions.[15-16, 31] Instead of rotating the rigid cork-screw-like structure, the flexible-oar-like motions are promoted by flexible oars or tails. Figure 1.3(c) shows an example of flexible-oar-like motions.[16] The nanoswimmers were comprised of rigid gold (Au) “head” and nickel (Ni) “tail” linked by partially dissolved silver (Ag) “joints”. Owing to the flexible Ag segment, the cone-shape rotation of Ni segments driven by magnetic field also maneuvered the rotation of Au segment. The distinct amplitudes resulting from the different length of each segment led to asymmetric thrusts, which eventually gave rise to unidirectional propulsion. The moving direction could be modified by adjusting either the length of Au and Ni segments or the direction of external fields, and the translational velocity could be tuned by controlling the frequency of rotating magnetic fields. The last type of motion driven by rotating magnetic field is the surface-assisted transport of micro/nanorobots [Figure 1.3(d)].[23, 32-33] The linear propulsion on the nanowire can be attributed to the asymmetric fluidic boundary conditions on the nanowire when it is rotating. Due to the larger hydrodynamic drag force near the microfluidic wall, distinct velocities can be induced on each end of the nanowire. Consequently, the center of rotation of the nanowire changes continuously, and results in a net in-plane motion.

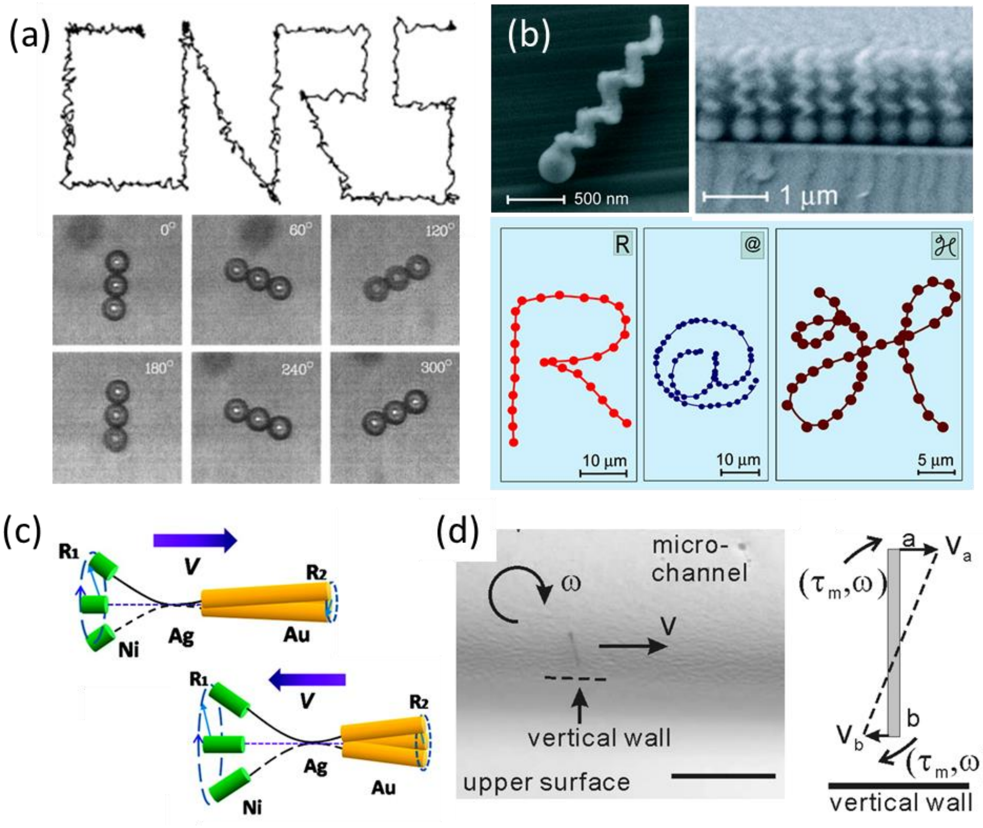
(a)
0°
60°
120°
180°
240°
300°
(b)
500 nm
1 µm
R
@
ℋ
10 µm
10 µm
5 µm
(c)
R1
V
R2
Ni
Ag
Au
R1
V
R2
Ag
Au
Ni
(d)
micro-channel
ω
V
vertical wall
upper surface
a
V_a
(τ_m,ω)
b
V_b
(τ_m,ω)
vertical wall

Figure 1.3: Magnetically actuated micro/nanomachines. (a) Transport of a magnetic microsphere and rotation of assembled microspheres. Reproduced with permission.[26] Copyright 2002, Elsevier. (b) Scanning electron microscopy (SEM) images and trajectories of nanoswimmers in cork-screw-like motions. Reproduced with permission.[28] 2009, American Chemical Society. (c) Schematic diagrams of flexible nanowire nanomotors moving forward (top) or backward (bottom) in flexible-oar-like motions. Reproduced with permission.[16] Copyright 2010, American Chemical Society. (d) Linear transport of a magnetic nanowire rotating near a vertical wall. Reproduced with permission.[23] Copyright 2010, American Chemical Society.

1.1.3 Optical manipulation

The most well-known optical technique for manipulating micro/nanomachines is the so-called "optical tweezers", which are also referred as "single-beam gradient force traps". The manipulation is based on forces exerted by a highly focused laser beam. These forces can trap and transport micro/nanoscale objects. The involved optical forces can be categorized into two types: scattering optical forces and gradient optical forces. A proper fundamental understanding of the optical forces depends on the size of the trapped objects relative to the wavelength of the employed lasers as shown in Figure 1.4.[34] In the Mie scattering regime, where the objects are much larger than the wavelength of laser beam, scattering optical forces dominate the trapping effect. The refraction and reflection of light by the trapped objects cause redirection of photon momentum. According to Newton's third law, the objects receive a backward momentum of equal magnitude. As a result, the refraction light induces the attraction of the objects to the region of highest light intensity and the reflected light compels the objects along the direction of laser beam propagation [Figure 1.4(a-c)]. For particles smaller than the wavelength of light, where Rayleigh scattering dominates, the scattering forces can be determined by the Fresnel equations and geometrical optics. The propulsion force F_{scat} along the axis of the laser beam is given by:[35]

$$F_{scat} = \frac{I_0}{c} \frac{128\pi^5 r^6}{3\lambda^4} \left(\frac{m^2-1}{m^2+2}\right) n_b \qquad (1.7)$$

where I_0 is the intensity of laser beam, r is the radius of the trapped particle, m is the ratio of the refraction index of the particles and the medium, λ is the wavelength in vacuum and n_b is the refraction index of the medium. In the Rayleigh scattering mode, the trapping of objects is mainly due to the gradient of the optical forces. As shown in Figure 1.4(d), the objects are electrically polarized by the electric component of the optical field. The interaction of the polarized objects with the electric component of the optical field results in the transport of the object along the gradient to the highest intensity of the optical field. The gradient force (F_{grad}) for a spherical particle due to Rayleigh scattering is given by:[35]

$$F_{grad} = -\frac{n_b^3 r^3}{2}\left(\frac{m^2-1}{m^2+2}\right)\nabla E^2 \qquad (1.8)$$

where E is the electric field of the laser beam.

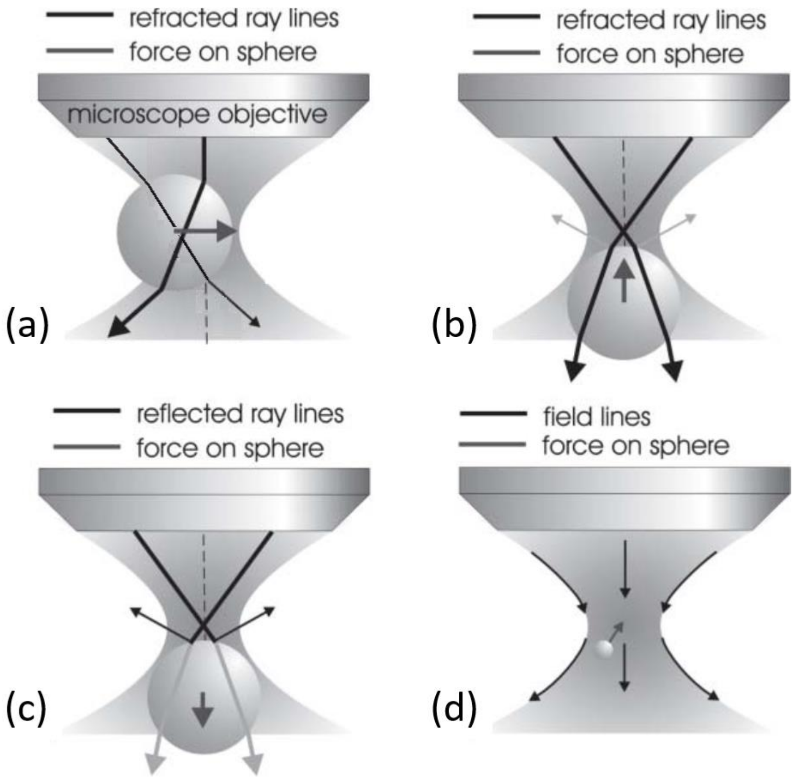
refracted ray lines
force on sphere
microscope objective
(a)
refracted ray lines
force on sphere
(b)
reflected ray lines
force on sphere
(c)
field lines
force on sphere
(d)

Figure 1.4: Schematic diagrams of manipulation mechanisms of optical tweezers. (a-b) For particles of sizes in the Mie scattering regime, the refraction of non-uniform light by the particles generates a net force along the optical field gradient towards the highest optical intensity. (c) The reflection of light results in a radiation pressure along the laser beam axis. (d) For particles with Rayleigh scattering, the electric force on light-induced electric dipoles in the particles compel the particles to transport along the gradient towards the highest electric field. Reproduced with permission.[34] Copyright 2008, Royal Society of Chemistry.

Although optical traps created by focused laser beams are generally considered as a static trapping technique, the control of physical motion of the optical traps has been widely used in manipulating various micro/nanoparticles.[36-38] Figure 1.5(a) presents the optical manipulation of a semiconductor nanowire in three dimensions by controlling the position and height of the focusing point of laser beam.[38] When one end of the nanowire was docked, the nanowire could be rotated around the tethered end by trapping and translating of its free end. Micro/nanoentities can also be manipulated by their interaction with the optical momentum carried by an incident light. Optical momentum has both linear and angular components. As shown in Figure 1.5(b), an optical torque is generated on the asymmetric micro/nano objects due to the change of the linear momentum of photons in refracted/reflected optical beams.[39] In general, linear momentum induced torques require a structural design with rotational symmetry but not bilateral symmetry. The rotation is usually along one direction only, either clockwise or counterclockwise, which is determined by the designed geometry.[40-41] The forces and torques generated by the interaction with angular photon momentum are more complicated. Angular momentum consists of a spin component and an orbital component. The former is associated with optical field gradient and polarization state of light.[42-43] Orbital angular momentum, on the other hand, is not associated with polarization but, rather, depends on spatial distribution of the field. The transfer of both forms of angular momenta to a trapped micro/nanoobject through birefringence or absorption can compel micro/nanoobjects into circular motion.[44-49] For instance, microgears designed with photonic nanostructures that exhibit birefringent characteristics could be rotated by circularly polarized light that carries spin angular momenta [Figure 1.5(c)].[46] In Figure 1.5(d), laser beams carrying orbital angular momenta show a helical wave front and focus into a ring rather than a point.[47-48] These helical light modes, also known as optical vortices, exhibit ring intensity patterns that can facilely actuate micro/nanodevices.[49] Micro/nanoobjects smaller than the ring are trapped in optical vortices and compelled to orbit around the ring pattern.

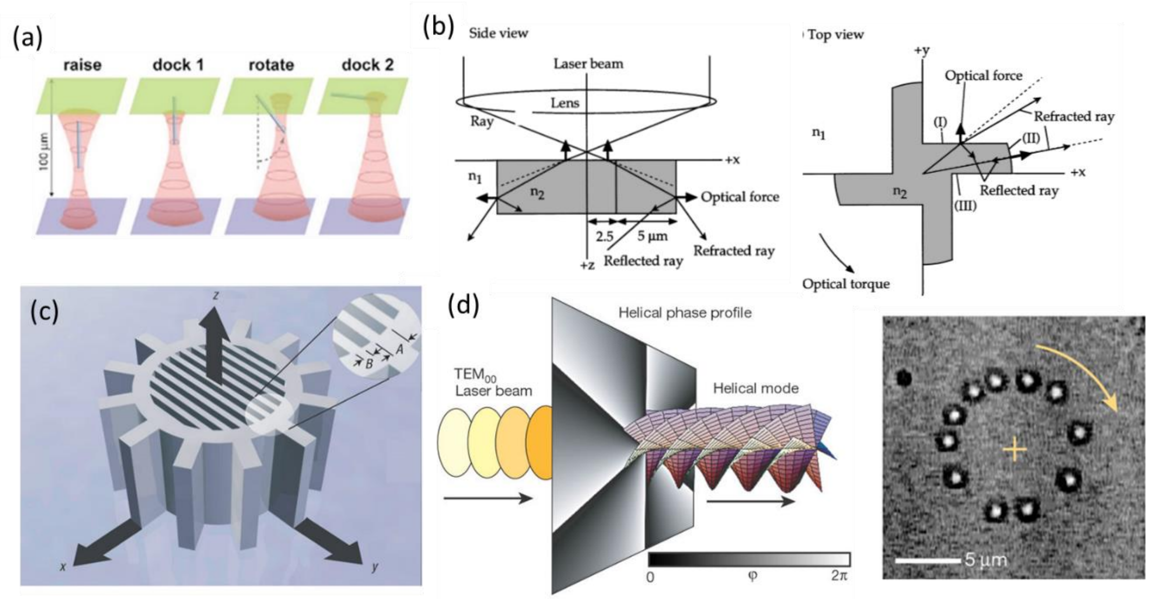
(a)
raise
dock 1
rotate
dock 2
100 μm
(b)
Side view
Laser beam
Lens
Ray
n_1
n_2
+x
Optical force
2.5
5 μm
+z
Reflected ray
Refracted ray
Top view
+y
Optical force
Refracted ray
(I)
(II)
(III)
Reflected ray
Optical torque
(c)
z
A
B
x
y
(d)
Helical phase profile
TEM$_{00}$
Laser beam
Helical mode
0
φ
2π
5 μm

Figure 1.5: Optical manipulation of micro/nanoentities. (a) Nanowire manipulated by optical traps. Reproduced with permission.[38] Copyright 2006, Nature Publishing Group. (b) The principle of torque generation by linear light momenta. Reproduced with permission.[39] Copyright 1997, AIP Publishing LLC. (c) Schematic of a structurally birefringent microgear driven by transfer of spin angular momentum. Reproduced with permission.[46] Copyright 2005, Nature Publishing Group. (d) Generation of helical light modes carrying orbital angular momentum, and the trapping and rotation of microparticles by transfer of orbital angular momentum. Reproduced with permission.[47] Copyright 2003, Nature Publishing Group.

1.1.4 Acoustic manipulation

Acoustic (or ultrasonic) manipulation of micro/nanoentities has recently been spotlighted due to their powerful propulsion force and great biocompatibility.[50-53] Acoustic tweezers based on standing surface acoustic waves are the most widely used acoustic micro/nano manipulation techniques. Surface acoustic waves are generated by interdigital transducers (IDTs) deposited on a piezoelectric substrate with designed arrangement and boundary conditions. As shown in Figure 1.6 (a), the IDTs can be arranged in either parallel or orthogonal manners on the piezoelectric substrate surround the microfluidic channels.[50] When a radio frequency signal is applied, two surface acoustic waves will be generated and propagate in antiparallel directions and in orthogonal directions, respectively. In both cases, standing surface acoustic waves will be formed due to the interference of two surface acoustic waves, with ordered arrays of pressure nodes (locations with the pressure amplitude is minimum) and antinodes (locations with the maximum pressure amplitude). The longitudinal-mode leakage waves from the standing surface acoustic waves will result in the fluctuation of pressure in the medium, and thus exert acoustic radiation forces on the particles in suspension. The primary acoustic force exerted on an object can be written as:[50]

$$F_r = -\left(\frac{\pi p_0^2 V_c \beta_w}{2\lambda}\right) \cdot \phi(\beta,\rho) \cdot \sin(2kx) \qquad (1.9)$$

$$\phi(\beta,\rho) = \frac{5\rho_c - 2\rho_w}{2\rho_c + \rho_w} - \frac{\beta_c}{\beta_w} \qquad (1.10)$$

where p_0 and λ are the acoustic pressure and wavelength, V_c is the volume of object, and ρ_c, ρ_w, β_c, β_w are the density of object and medium, compressibility of the object and medium, respectively. The balanced position of particles can be either pressure nodes or antinodes determined by the sign of ϕ: if $\phi > 0$, pressure nodes will be the trapping positions, and vice versa. Further, Huang and co-workers demonstrated flexible two-dimensional manipulation of microentities in an acoustic tweezers with four chirped IDTs [Figure 1.6(b)].[51-52] Chirped IDTs have a linear gradient in its finger period structure, which offers a much wider range of resonant frequencies. By tuning the input radio signal frequency, the pressure nodes positions will shift accordingly, thus achieving the dexterous transport of trapped particles. However, the displacement is proportional to the node order and thus is different for each pressure node. A phase shift strategy can also realize the in-plane manipulation and even uniform displacement. By tuning the phase shift, microparticles or cells could be move to any location smoothly along an arbitrary path within the microfluidic chamber with great improvement in dexterity and accuracy.

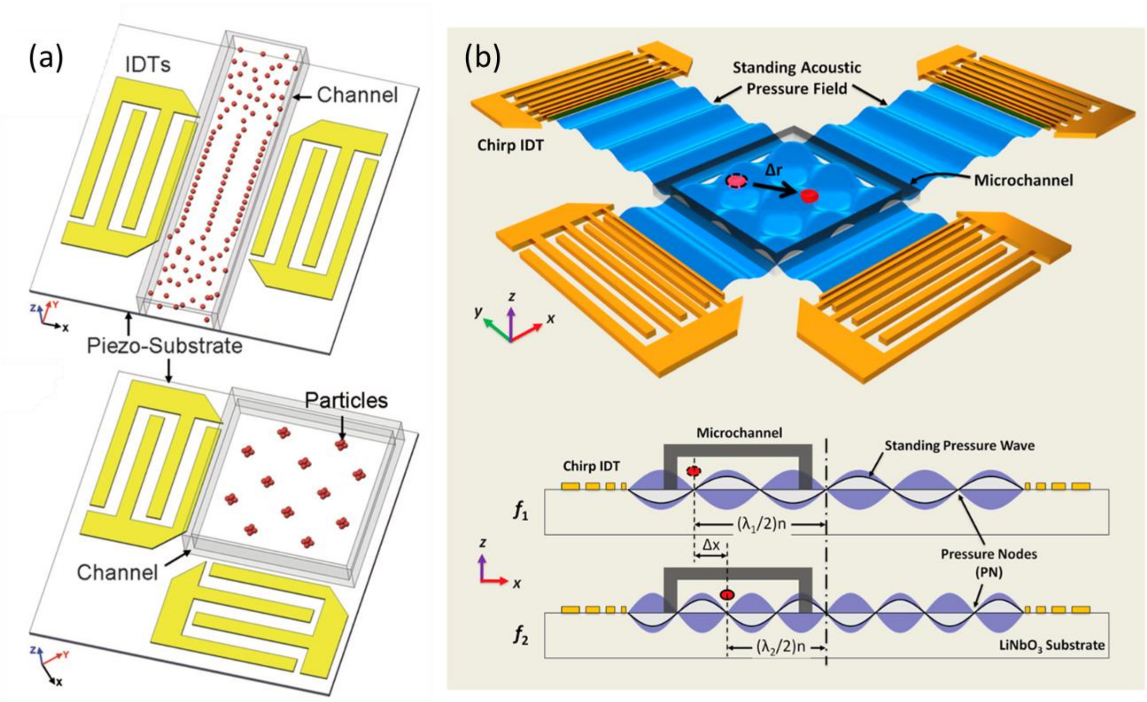
(a)
IDTs
Channel
Piezo-Substrate
Particles
Channel
(b)
Standing Acoustic Pressure Field
Chirp IDT
Δr
Microchannel
y
z
x
Microchannel
Chirp IDT
Standing Pressure Wave
f_1
$(\lambda_1/2)n$
Δx
Pressure Nodes (PN)
f_2
$(\lambda_2/2)n$
$LiNbO_3$ Substrate

Figure 1.6: Acoustic tweezers. (a) Schematic of the standing surface acoustic waves based patterning design of IDTs. Top: one-dimensional patterning using two parallel IDTs. Bottom: two-dimensional patterning using two orthogonal IDTs. Reproduced with permission.[50] Copyright 2009, Royal Society of Chemistry. (b) Schematics of device structure and working mechanism of the four-IDTs acoustic tweezers. Bottom: a standing surface acoustic wave field generated by driving chirped IDTs at two different frequencies. Reproduced with permission.[51] Copyright 2012, Proc. Natl. Acad. Sci. USA.

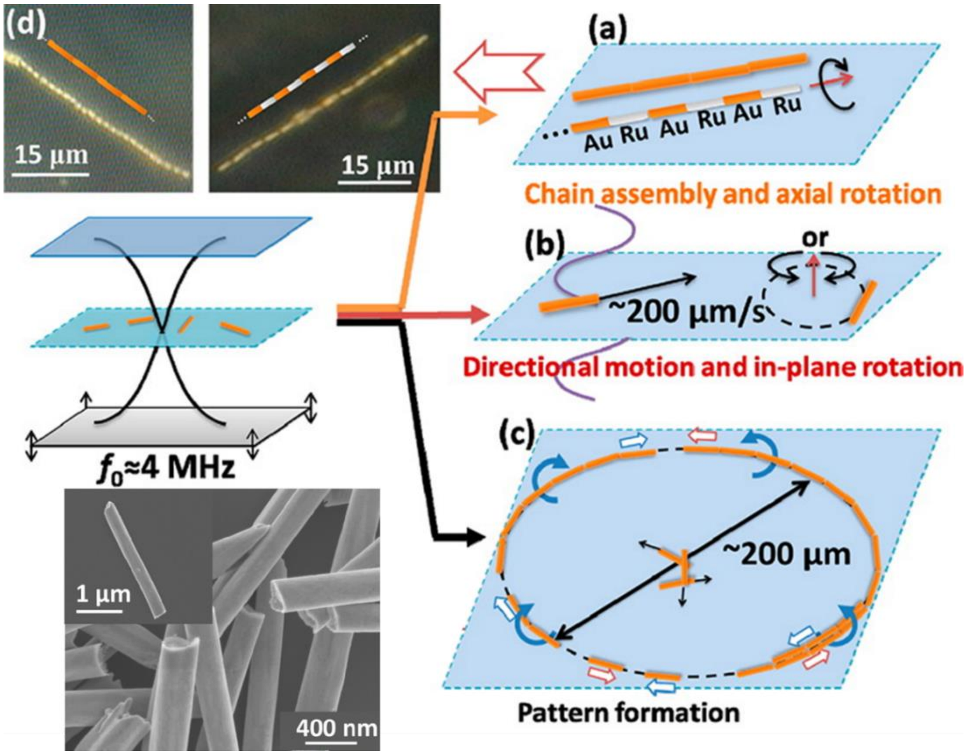
(d)
15 µm
15 µm
(a)
Au Ru Au Ru Au Ru
Chain assembly and axial rotation
(b)
or
~200 µm/s
Directional motion and in-plane rotation
(c)
~200 µm
Pattern formation
f_0≈4 MHz
1 µm
400 nm

Figure 1.7: Various movement modes of ultrasound-propelled nanomotors: (a) schematic and (d) optical images of chain assembly and axial rotation; (b-c) directional motion, in-plane rotation and pattern formation, respectively. Inset: SEM image of asymmetric nanorods with one of the tips concaved. Reproduced with permission.[54] Copyright 2012, American Chemical Society.

Despite the standing surface acoustic wave based manipulation, ultrasound can also directly provide powerful propulsion for the transport of micro/nanomotors.[54-56] Mallouk *et. al.* first described the autonomous motion of metallic microrods that were propelled by ultrasound in MHz frequency range [Figure 1.7].[54] Depending on the geometry and material of the nanorods and frequencies of the ultrasound, complex behaviors of the nanowires could be realized, including directional transport, axial and in-plane rotation, as well as chaining and pattern formation. The mechanism was attributed to self-acoustophoresis, where an acoustic pressure gradient, *i.e.*, acoustophoresis, is induced on individual nanoparticles with asymmetrical geometries that result in propulsion. Nanorods with asymmetric shape were fabricated *via* template electrodeposition method. The concave geometry on one end of nanorod concentrated acoustic energy when scattering the ultrasound waves; while the other end is flatter, thus with lower weaker energy density. Therefore, the asymmetric shapes led to unbalanced pressure that propelled the nanorods with the flat end constantly facing forward.

1.1.5 Chemical manipulation

One of the most intensively explored types of micro/nanomachines is so-called chemical micro/nanomotors, which convert chemical energy from surrounding chemical reactions into mechanical motions, mimicking biomolecular motors in nature.[57-61] Depending on the designs of micro/nanomotors and the reactions involved, two mechanisms have been proposed for their self-propelling behaviors: self-electrophoretic mechanism based on the establishment of concentration gradients, and bubble recoil mechanism based on the production of bubbles [Figure 1.8]. In self-electrophoresis, the chemical reactions involving both oxidation and reduction, *e.g.*, the decomposition of hydrogen peroxide, occur on the different material segments of the chemical motors, *e.g.*, platinum (Pt) and Au segments of nanowires as shown in Figure 1.8 (a), respectively.[59] An effective voltage is formed across the distinct material regions that interact with the liquid suspension surrounding of the nanowires, and propels their motions. This mechanism is similar to that of electrophoresis in Section 1.1.1, while the electric field herein is generated locally from chemical reactions and does not require external power supplies. Therefore, the velocity of the nanomotors due to self-electrophoresis is given by:[62]

$$v_{SEP} \sim \frac{\varepsilon_m \zeta}{\eta} E \sim \frac{\varepsilon_m \zeta \Delta\phi}{\eta l} \qquad (1.11)$$

where ε_m and η are the dielectric constant and viscosity coefficient of the liquid media, respectively, ζ is the zeta potential. The self-generated electric field E is approximated as the potential drop $\Delta\phi$ divided by the length of the nanorods l. $\Delta\phi$ is determined by the chemical potential of the two metal segments of a nanomotors. Therefore, the velocity of nanomotors can be significantly enhanced by optimizing the materials with a large chemical potential difference. In the bubble-propulsion based driving mechanism, it was found that growth and burst of gas microbubbles (*e.g.* oxygen) produced during the rapid chemical reactions can evidently propel nanomotors due to the induced local pressure gradient [Figure 1.8(b)].[63] This effect is more observed in nanomotors with complex geometries, *e.g.*, nanotube structures, and tailored distribution of the reactive or catalytic elements on the surfaces.[64-67]

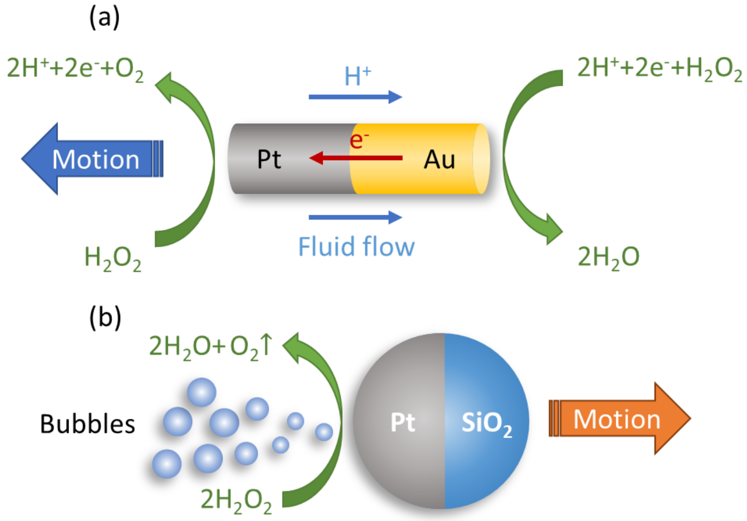
(a)
$2H^+ + 2e^- + O_2$
H^+
$2H^+ + 2e^- + H_2O_2$
Motion
Pt
e^-
Au
H_2O_2
Fluid flow
$2H_2O$
(b)
$2H_2O + O_2\uparrow$
Bubbles
Pt
SiO_2
Motion
$2H_2O_2$

Figure 1.8: Schematic of chemical manipulations based on (a) self-electrophoretic mechanism, and (b) bubble recoil mechanism, respectively.

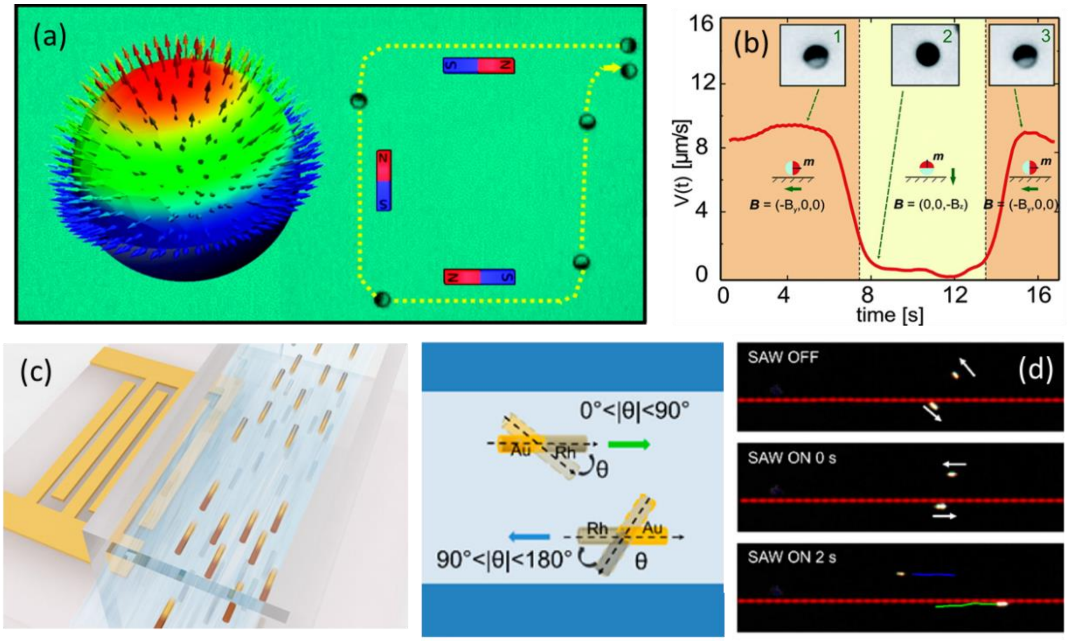

Figure 1.9: Direction control on chemical micro/nanomotors. (a-b) Control based on magnetic tweezers: (a) schematics of the distribution of magnetic moments and the deterministic motion of the Janus nanomotor guided by an external magnetic field; (b) on/off controlled motion of the Janus nanomotor. Reproduced with permission.[68] Copyright 2012, American Chemical Society. (c-d) Control based on acoustic tweezers: (c) schematics of the acoustic device and the alignment of nanomotors; (d) demonstration of aligned motion of two nanomotors that have different initial orientation. Reproduced with permission.[69] Copyright 2017, American Chemical Society.

During the transport of the chemical micro/nanomotors, their movement directions are usually random and constantly changing with time. Different mechanisms have been developed for controlling their transport orientation.[42, 69-71] The magnetic tweezers is the most widely used technique that guides the moving directions, with magnetic segments integrated into the chemical nanomotors.[42, 70-71] For instance, by coating magnetic metallic thin films with the average magnetic moment orientation coinciding with its main symmetry axis, the Janus nanomotors could be aligned along the external magnetic field, as shown in Figure 1.9(a).[42] The reorientation of the magnetic field with a magnitude smaller than the coercive field redirected the movement of the Janus nanomotors but not changed the orientation of its magnetic moment. Guided by the magnetic tweezers and fueled by the chemical reaction, the nanomotors could pick up and transport cargos, and realize on/off control on their motions [Figure 1.9(b)]. A guidance strategy based on acoustic tweezers was also reported recently as shown in Figure 1.9(c-d).[69] The surface acoustic wave aligned the long axis of micromotors to the pressure node line on a short timescale. The asymmetry of bimetallic micromotors led to two kinds of orientations, which were determined by the initial angle between the long axis of the nanorod and the pressure node line.

1.2 BIOAPPLICATIONS: BIOCHEMICAL DELIVERY AND DIAGNOSTIC SENSING

With the advantageous manipulation mechanisms and operation versatility, these micro/nanomachines offer promising solutions for the next-generation technology in a variety of disciplines including analytical chemistry,[72] environment science,[73] biochemical delivery,[74-75] biomedicine, and diagnosis.[76-77] The fascinating biomedical applications of artificial micro/nanomachines in therapeutic drug delivery and diagnostic biochemical sensing have been of particular interest.

The precise control in both the propulsion thrusts and alignment direction of micro/nanomachines, *i.e.*, driving along arbitrary trajectories in two dimensions with controlled speed and orientation, allows the delivery and release of drugs to designated locations *in vitro*. One of the first demonstrations of single-cell biosubstance delivery was demonstrated by electric tweezers, which manipulated drug-loaded nanowires precisely for drug delivery to a targeted cell amid many [Figure 1.10(a)].[78] Multiple nanowires could be delivered to the targeted single cell one after another. As a result, the dose of the drug was controlled by the number of nanowires delivered. The drug stimulation was localized to the targeted cell without an observable response from cells close by. Similar functions can also be realized by a type of helical magnetic microswimmers [Figure 1.10(b)].[79-81] They showed directional corkscrew motions at elevated frequencies of 10 to 60 Hz. They could even climb up and down along the vertical direction. With drug molecules embedded in temperature-sensitive liposomes, the helical microswimmers transported and delivered the drug-loaded liposomes to a target cell, and released the drugs triggered by temperature stimulation. In addition, the versatility of micro/nanomachines that are powered by acoustic fields or chemical reactions and guided by magnetic fields has been demonstrated in the applications of target drug delivery.[55, 66, 82-83]

The applications of chemical micro/nanomachines are not limited to the delivery and release of micro/nanoparticles or biochemical substances. Their responsiveness to the surrounding environment has opened up new opportunities for applications in mechanical motion-based sensing. Highly sensitive changes in speed or traveling distance of chemical micro/nanomotors (traced by an optical microscope) are used to reveal the presence of targeted analytes.[84-87] The signal transduction from chemical concentration to the change of motion behaviors provides a new type of analytical approach that does not require sophisticated instrumentation. The possibility of mass production of chemical micro/nanomotors supports their great potential for practical applications in analytical chemistry and diagnostic biochemical sensing. Figure 1.11(a) presents an example of novel nanomotor-based sensing strategy for specific DNA and RNA detection.[85] The presence and capture of target nucleic acid would lead to the attachment of Ag nanoparticles. The subsequent dissolution of Ag nanoparticles in the hydrogen peroxide fuel released Ag ions, which increased the potential difference and led to a dramatical enhancement in the speed of nanomotors.[87] The speed of nanomotors was proportional to the concentration of target nucleic acid, which could be as low as attomole level for the detection.

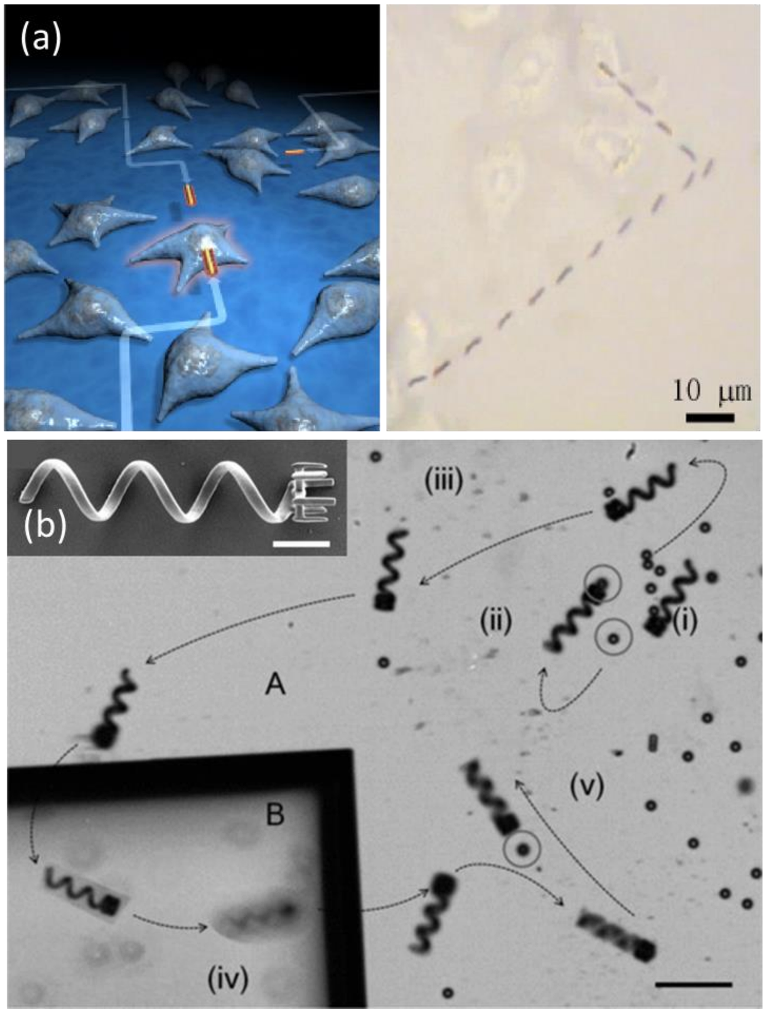

Figure 1.10: (a) Schematic and overlapped optical images of nanowires precisely transported onto a selected cell following prescribed trajectory using electric tweezers. Reproduced with permission.[7] Copyright 2011, Elsevier. (b) A helical magnetic microswimmer (i) approaching, (ii) capturing, (iii, iv) transporting, and (v) dropping off targets in DI water. The microswimmer moved between the regions A and B with step height. The inset SEM image shows the structure of the helical microswimmer with the cargo holder. Reproduced with permission.[18] Copyright 2012, Wiley-VCH.

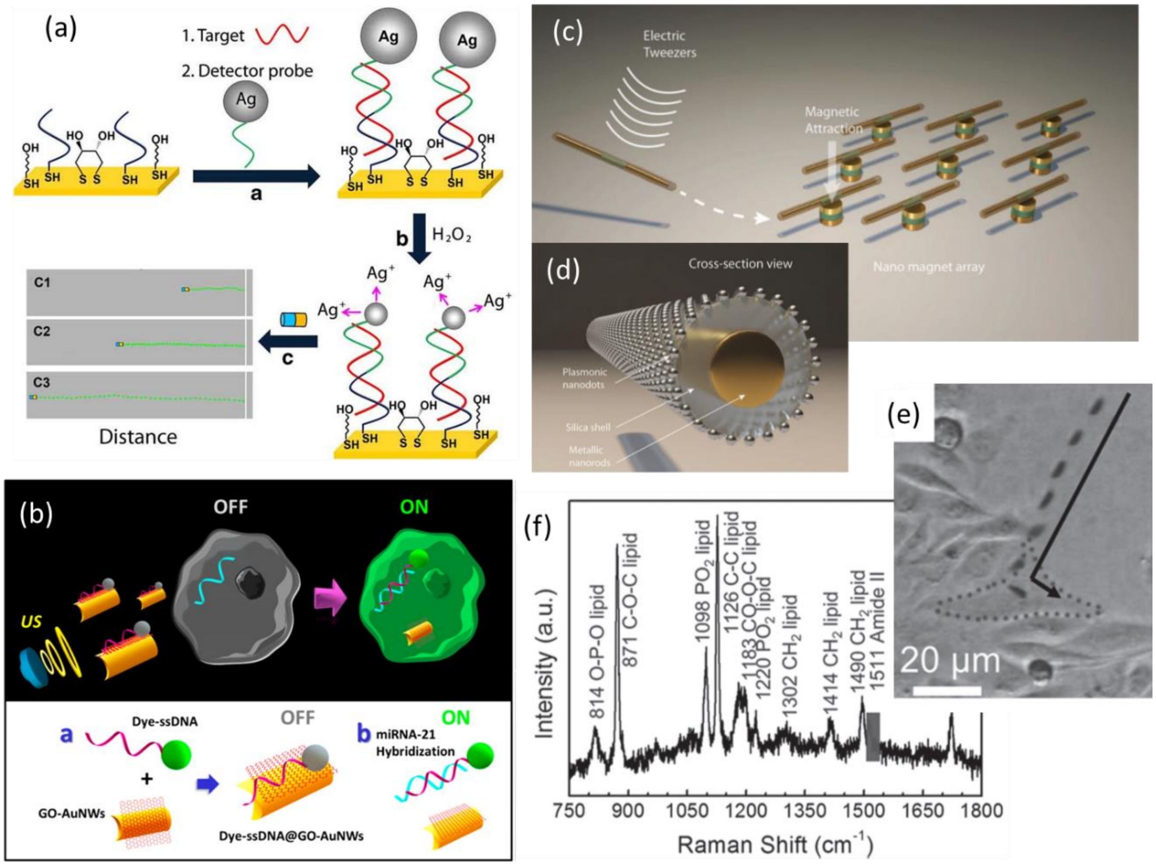
(a)
1. Target
2. Detector probe
Ag
a
b
H_2O_2
Ag^+
c
C1
C2
C3
Distance
HO
OH
SH
S S
(b)
OFF
ON
US
a
Dye-ssDNA
+
GO-AuNWs
Dye-ssDNA@GO-AuNWs
b
miRNA-21 Hybridization
(c)
Electric Tweezers
Magnetic Attraction
Nano magnet array
(d)
Cross-section view
Plasmonic nanodots
Silica shell
Metallic nanorods
(e)
20 µm
(f)
814 O-P-O lipid
871 C-O-C lipid
1098 PO_2 lipid
1126 C-C lipid
1183 CO-O-C lipid
1220 PO_2 lipid
1302 CH_2 lipid
1414 CH_2 lipid
1490 CH_2 lipid
1511 Amide II
Intensity (a.u.)
750
900
1050
1200
1350
1500
1650
1800
Raman Shift (cm^{-1})

Figure 1.11: (a) Schematic diagram of motion-based nucleic acid detection relying on the silver-induced speed enhancement. Reproduced with permission.[85] Copyright 2010, Macmillan Publishers Limited. (b) Illustration of the acoustically propelled nanomotors for single-cell real-time miRNA detection. Reproduced with permission.[88] Copyright 2015, American Chemical Society. (c-d) Schematic of plasmonic-active nanocapsules assembled in order arrays by electric tweezers for SERS detection. Reproduced with permission.[89] Copyright 2012, Wiley-VCH. (e) Overlaid microscopic images of a plasmonic nanocapsule transported to a live cell by magnetic manipulation. (f) Raman spectrum of the cell membrane detected from the plasmonic nanocapsule. Reproduced with permission.[90] Copyright 2013, Wiley-VCH.

Besides the motion-based sensing discussed above, micro/nanomachines can also work as motorized platforms, which carry and transport different types of nanosensors to designated locations.[91] Such mobile sensing platform can address issues of traditional stationary nanosensors by offering at least two advantages. The robotized biochemical sensors can (1) actively transport to regions of interest and perform location predictable sensing, and (2) increase the likelihood of analyte molecules in contact with the sensors. J. Wang *et al.* successfully employed acoustic driven nanorods as mobile platforms and developed single-cell miRNA sensors [Figure 1.11(b)].[88] The surfaces of nanomotors were modified with graphene oxide for attachment of biomolecules and suppressing their fluorescence. After entering cells, the fluorescent probes were released and bound to target miRNA in cell plasma. This process restored the fluorescence. Such “Off-On” switching in fluorescence enabled real-time detection of target miRNA within a few minutes. Electrical fields and magnetic fields have also been exploited to develop robotized biochemical sensors [Figure 1.11(c-f)].[89-90] Fan *et al.* designed motorized plasmonic nanocapsules that can controllably transport, assemble, and detect biochemicals in a position deterministic manner with Raman spectroscopy.[89-90] Dense arrays of Ag nanoparticles were conformally grown on the outer surfaces of nanomotors, serving as hotspots for Surface Enhanced Raman Scattering (SERS) detection [Figure 1.11(d)]. Manipulated by either electric fields or magnetic fields, the plasmonic nanocapsules could be transported and assembled to designated magnetic micropatterns, or be transported to a single live cell, laying on the membrane and analyzing the cell membrane composition [Figure 1.11(e-f)].

Chapter 2: Rotary nanomotors driven by electric fields[†]

Rotary nanomotors, which can convert diverse input energy sources to mechanical rotary motions, are a type of device critical for advanced micro/nanomachines.[92] Various approaches have been explored to rotate nanoentities, including nanospheres, nanowires, nanotubes, and helical, crossed, and gear-shaped structures, by using chemical/biochemical propulsion or external physical fields (light, magnetic fields, electrical fields, or ultrasonic waves). However, the applications of rotary nanomotors are still greatly hindered by several difficulties:[93-94] (1) first, it remains extremely difficult to use the as-synthesized micro/nanoparticles as rotary micro/nanomotors that can stably operate at fixed positions, which is essential for effectively localized operations, such as localized release of drug, transmitting forces and torques, as well as coupling nanomotors with other devices; (2) moreover, traditional fabrication and assembly of miniature motors require complex design and arduous processes, which lead to high costs and low yield, and is not suitable for massive production and further application; (3) finally, all the current nanomotor devices also suffer from a short lifetime (only a few minutes), which significantly limit their practical applications.

In this chapter, an innovative type of nanomotors is proposed and demonstrated to be efficiently assembled and stably rotated at designated locations by utilizing nanoscale building blocks with nanowires as rotors and patterned nanomagnets as bearings.[95-97] Based on the electric tweezers, the employed field-assisted assembling strategy greatly reduces the difficulties in fabricating rotary NEMS devices compared with traditional top-down fabrication technologies. The building blocks of the rotary nanomotors can be fabricated in massive production. We achieved a rotation speed up to 18,000 rpm and a lifetime of 80 hours and over 1.1 million rotation cycles. To the best of our knowledge, the demonstrated lifetime and operating cycles are the best among rotary nanomotors of similar dimensions. We also investigated the rotation characteristics including the time-dependent speeds, forces, and torques during the long-term operation of the nanomotors.

[†] Portions of this chapter have been previously published in K. Kim[#], X. Xu[#], **J. Guo**[#], D. Fan, Nature Communications, 5, 3632 (2014); **J. Guo**, K. Kim, K. W. Lei, D. Fan, Nanoscale, 7, 11363-11370 (2015). In the work published on Nature Communications, J. Guo, K. Kim, and X. Xu carried out the experiments on different aspects of this project and contributed equally. They are listed as co-first authors. In the work published on Nanoscale, J. Guo is the leading student author, who designed and performed the experiments, modelled the system, and analyzed the data. He wrote the first draft of the manuscript. K. Kim taught J. Guo the experimental techniques and assisted with data analysis. As the faculty author of both articles, Professor D. Fan conceived the research and supervised both projects. She analyzed the results, modeled the systems, and revised both manuscripts.

2.1 DESIGN AND ASSEMBLY OF ROTARY NANOMOTORS FROM NANOSCALE BUILDING BLOCKS

The rotary nanomotors are designed to consist of multi-segment Au/Ni/Au nanowires acting as rotors, patterned nanomagnets acting as bearings and quadruple microelectrodes acting as stators [Figure 2.1(a)]. The patterned nanomagnets are the core components for the assembly of the nanoscale building blocks into rotary nanomotors. The nanomagnets consist of tri-layer thin-film stacks: spacer layer, magnetic layer, and adhesion layer. Each layer in the nanomagnets serves a purpose as follows: the bottom chromium (Cr) layer adheres to the substrate, the middle magnetic layer (Ni) provides the magnetic field, and the top spacer layer, such as Au or titanium (Ti), is used for adjusting the spacing between the magnetic layer and the nanowires in order to tune the magnetic attraction. The magnetic attraction can be adjusted so precisely that it can anchor the nanowires to the bearings, but not too tightly to prevent the nanowires from rotating.

The rotary nanomotors are assembled by software-controlled electric tweezers, which could align and transport longitudinal nanoentities with a resolution of ~300 nm [Figure 2.1(b)].[8] The nanowire rotors suspended in deionized (DI) water are transported in both the X and Y directions to the vicinity of the magnetic bearings. The transport velocity and alignment orientation can be separately controlled by the applied DC and AC voltages, respectively.[8] When a nanowire rotor is approaching a nanomagnet, the strong magnetic attraction between the Ni segment in the nanowire and the Ni layer in the magnetic bearing swiftly assembles the nanowire rotor atop the magnetic bearing and forms a nanomotor. By applying four AC electric voltages with sequential 90° phase shift on the quadruple microelectrodes, the rotary nanomotor can be compelled to rotate with controlled angle, speed, and orientation [Figure 2.1(c)].

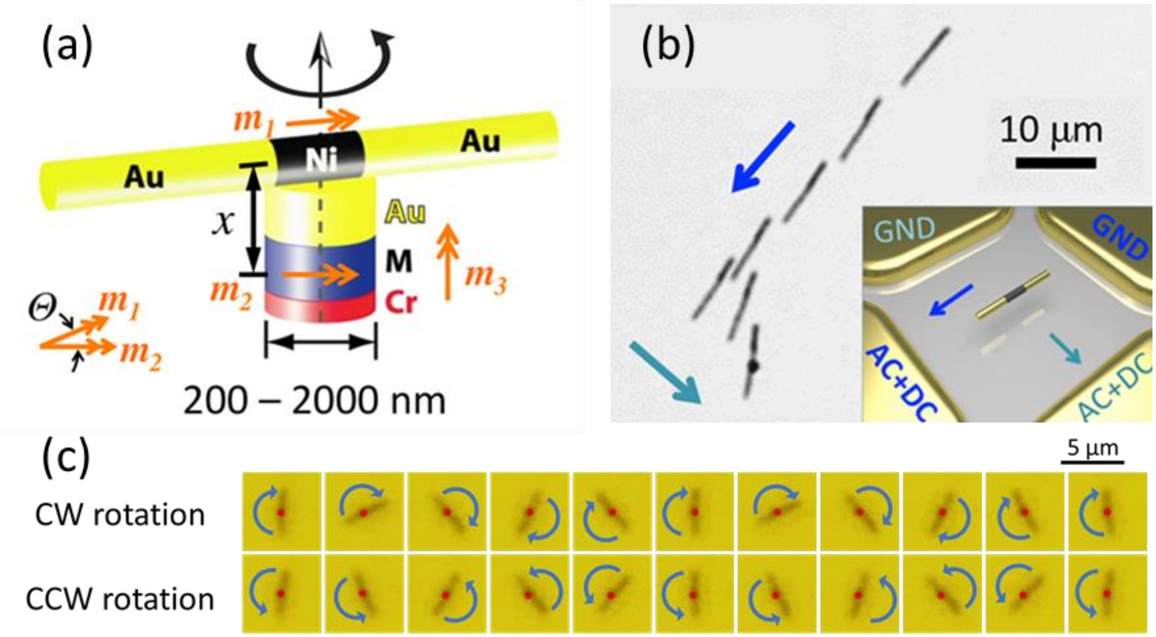

Figure 2.1: (a) Schematic diagram of a rotary nanomotor. (b) Overlapped images of a nanowire rotor transported and assembled on a nanobearing by the electric tweezers. Inset: schematic diagram of electric tweezers manipulating a nanowire rotor. Reproduced with permission.[95] Copyright 2014, Macmillan Publishers Ltd. (c) Sequential optical images of a nanomotor rotating clockwise (CW) and counterclockwise (CCW) every 60 ms. The positions of the bearing are highlighted by red dots. Reproduced with permission.[96] Copyright 2015, Royal Society of Chemistry.

2.2 LARGE-SCALE FABRICATION OF THE NANOMOTOR COMPONENTS

The building blocks of the rotary nanomotors, including multi-segment nanowires and magnetic nanobearings, are obtained by large-scale bottom-up synthesis, which could be scaled up for mass production.

Arrays of multi-segment nanowires are fabricated by electrodeposition into nanoporous templates in a three-electrode setup as shown in Figure 2.2(a).[35, 40] The three electrode system consists of a copper (Cu) layer on the back of polycarbonate nanoporous template as the working electrode, Pt mesh as the counter electrode, and Ag/AgCl electrode as the reference electrode. The deposition of materials is initiated from the Cu film at the bottom of nanopores, the size of which determines the diameter of the nanowires. The amount of electric charges passing through the circuit controls the length of each segment of the nanowires. After the nanoporous template is dissolved, arrays of nanowires can be readily synthesized [Figure 2.2(c)].

The patterned magnetic nanobearings are fabricated by using poly-methyl methacrylate (PMMA)/Cr templates prepared *via* colloidal lithography [Figure 2.2 (b)]. The fabrication consists of following steps: first, a polystyrene (PS) nanosphere monolayer is uniformly dispersed on the surface of PMMA films. Then, a thin layer of Cr is deposited on top of the PMMA film. After the removal of the PS nanospheres and oxygen reactive ion etching (RIE) with the Cr layer as the etch mask, arrays of nanoholes are formed on the PMMA film. Next, the multi-layer metal thin films are deposited into the nanoholes, which form into a large array of nanodisks after selective dissolution of the PMMA template. The density and size of the magnetic bearings can be well controlled by the concentration and the size of the PS nanospheres in the suspension. The as-obtained magnetic bearings are mono-dispersed in both diameters and thicknesses. The quality is comparable to those fabricated by the conventional electron-beam lithography, while the productivity is significantly improved [Figure 2.2(d)].

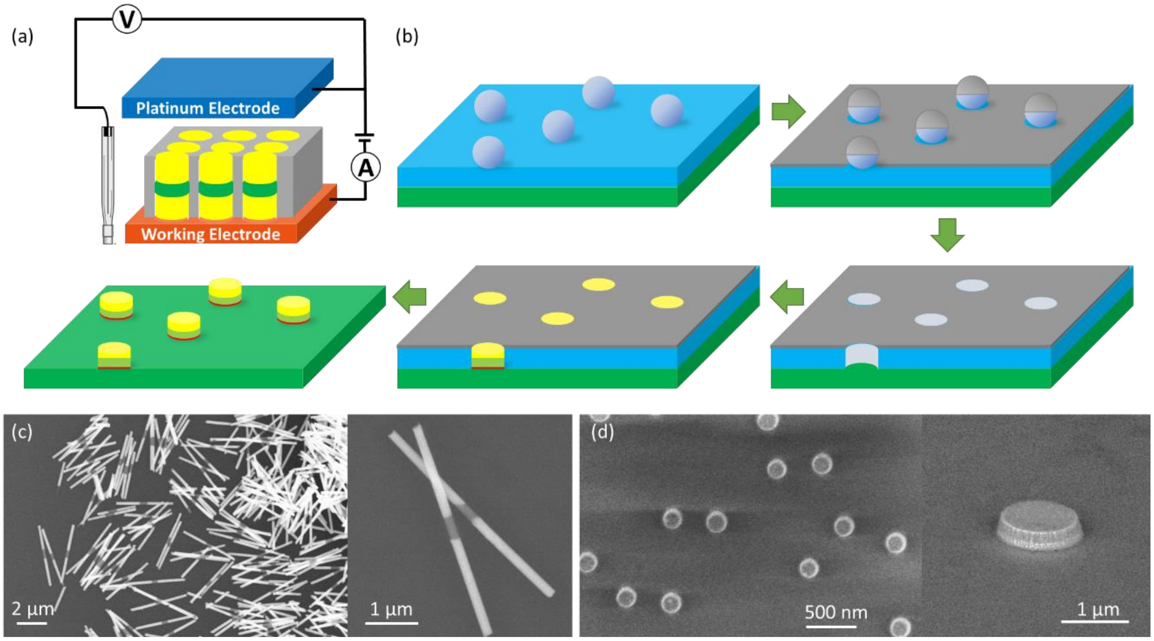

Figure 2.2: Fabrication process of (a) multi-segment nanowires as rotors in the rotary nanomotors and (b) multilayer magnetic nanodisks as bearing in the rotary nanomotors. (c-d) SEM images of (c) Au/Ni/Au multi-segment nanowires and (d) magnetic nanobearings.

2.3 ULTRASMALL ROTARY NANOMOTORS

One of the biggest advantages of nanomotors is their small footprint. However, the smaller size will lead to stronger Brownian motion, which may disturb and limit the operation of these nanomotors. Using a microscope equipped with a 100× oil-immersion objective and thin coverslips as substrates, we clearly observed controllable rotation of nanomotors made of three-segment nanowire rotors of 165 nm in diameter and 800~900 nm in total length [Au (350~400 nm)/Ni (100 nm)/Au (350~400 nm)] and magnetic bearings of 200 nm in diameter [made of tri-layer thin-film stack of Au (20 nm)/Ni (80 nm)/Cr (6 nm)] as shown in Figure 2.3(a-c). All characteristic dimensions of the nanomotors are less than 1 μm, which is at least 10 times smaller than that of the state-of-the-art micromotors fabricated through the top-down approach. The nanomotors are even smaller than the motors made from nanotubes.[94] The optimized electric frequency for the fastest rotation of nanomotors was found at ~100-120 kHz [Figure 2.3(d)]. The nanomotor could rotate in both clockwise and counterclockwise directions as shown in Figure 2.3(e). The rotation speed is not as uniform as those of nanomotors of a few micrometers in length, which can be attributed to stronger Brownian motions found in smaller objects in suspension.

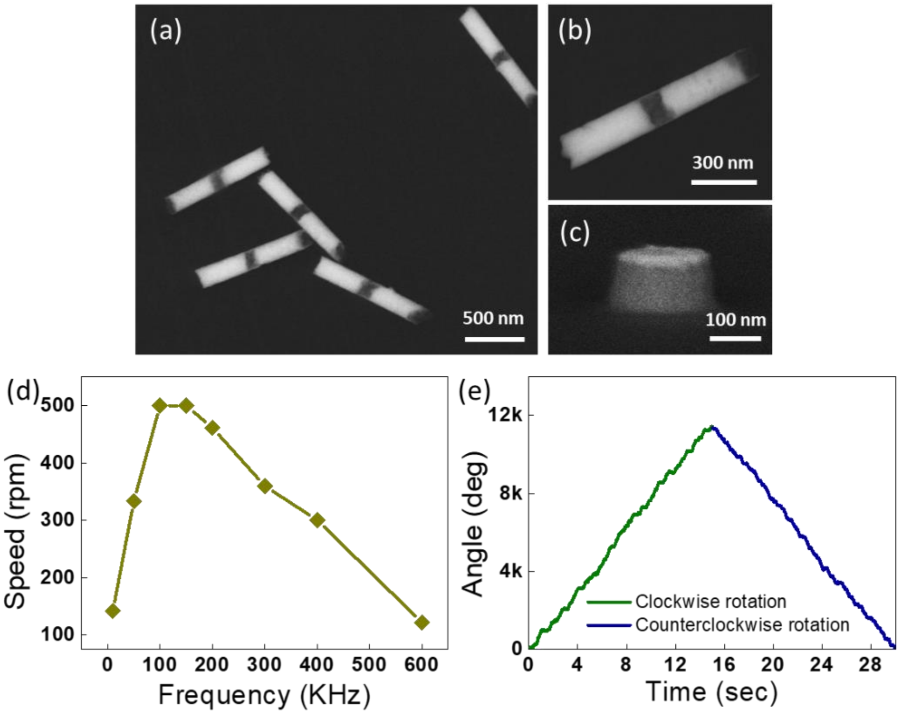

Figure 2.3: (a) SEM images of the as-synthesized Au/Ni/Au nanowires. The Au (bright) and Ni (dark) segments are 350~400nm and 100 nm, respectively. (b-c) Close-up SEM image of (b) a single nanowire and (c) a magnetic bearing. (d) Rotation speed of a nanomotor made of nanowires and magnetic bearings shown in (a-c) *versus* applied electric frequency. (e) Rotation angle as a function of time for both CW and CCW rotation of a nanomotor. Reproduced with permission.[95] Copyright 2014, Macmillan Publishers Ltd.

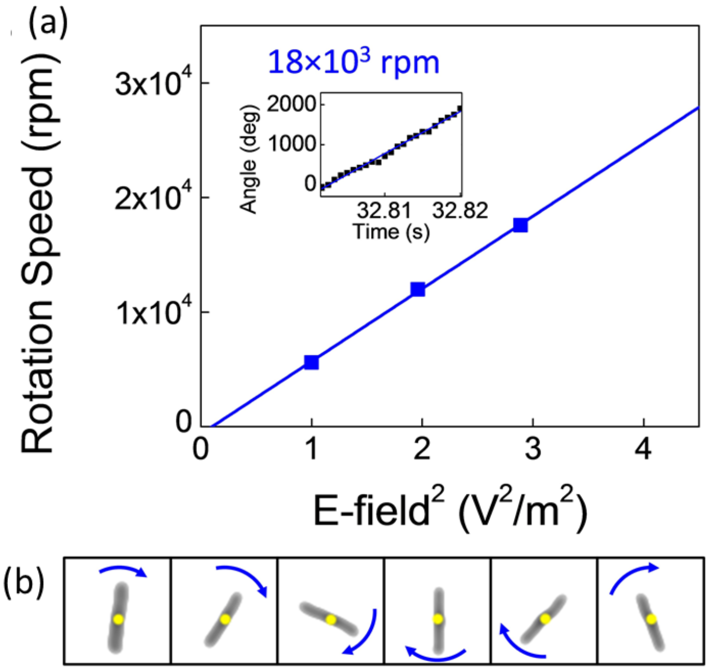

Figure 2.4: Ultrafast rotation. (a) Rotation speed of nanomotors from 10 to 17V at 30 kHz in a 100-mm-gapped quadruple microelectrode. Inset: angle *versus* time of the nanomotor rotating CW with a speed of ~18,000 rpm. (b) Enhanced snapshot images taken every 0.8 ms of the same nanomotor rotating at ~18,000 rpm at 17V and 30 kHz. Reproduced with permission.[95] Copyright 2014, Macmillan Publishers Ltd.

2.4 ULTRAFAST ROTARY NANOMOTORS

How fast can the nanomotors ultimately rotate? To test the limit, we optimized the AC E-field intensity and frequency. The rotation speed of nanomotors should increase with E-field with a quadratic power dependence ($v \sim E^2$) according to our understanding of the rotation electric torques, which will be discussed later. Simply narrowing the gap distance of the quadrupole electrodes could greatly enhance the E-field. For instance, narrowing the gap distance from 500 to 100 µm, we readily increased E^2 by 25 times. For 10 µm Au/Ni/Au nanowires in DI water, the maximum rotation speed was obtained experimentally at an E-field of 30 kHz. Applying these optimized conditions, we rotated nanomotors to a speed of at least 18,000 rpm at 17V as shown in Figure 2.4. The rotation orientation is CW as determined from the slowed motion. As expected, the rotation speeds (to at least 18,000 rpm) are proportional to E^2. It counts for the ultrahigh-speed rotation at only 17V. As far as we know, such a rotation speed is the highest achieved in natural or man-made motors of the same scale. It is of the same speed level of jet engine, but is still not the limit. In comparison, the highest speed of nanomotors with bearings for position fixed rotation is 498 rpm, obtained from the organic-inorganic hybrid nanomotors.[93]

2.5 ULTRADURABLE ROTARY NANOMOTORS

How durable are these nanomotors? We performed lifetime test on three types of rotary nanomotors rotating continuously without any interruption. The first type is the nanomotors mentioned in Section 2.3, which were made of three-segment nanowire rotors of 165 nm in diameter and 800~900 nm in total length [Au (350~400 nm)/Ni (100 nm)/Au (350~400 nm)] and magnetic bearings of 200 nm in diameter [made of tri-layer thin-film stack of Au (20 nm)/Ni (80 nm)/Cr (6 nm)]. This ultrasmall nanomotor could keep rotating for up to 15 h, which results in >240,000 cycles in total [Figure 2.5(a)]. This performance has surpassed the recent top-down-made Si micromotors,[98] showing the realistic potential of our nanomotors. After 15 h rotation, the Au cap layer on magnetic bearing was significantly thinned by frictional wearing. The SEM image in Figure 2.5(b) reveals the final Au thickness of ~15 nm, reduced from its original thickness of 40nm. No clear wear was found on the nanowire rotor, which can be attributed to the fact that Au (Element Vickers. hardness: 216 MPa) is much softer than Ni (Element Vickers hardness: 638 MPa).[99] The rotation of nanomotors was finally terminated by the increased magnetic attraction force and the consequential larger friction between rotors and bearings because of the reduced thickness of the Au layer.

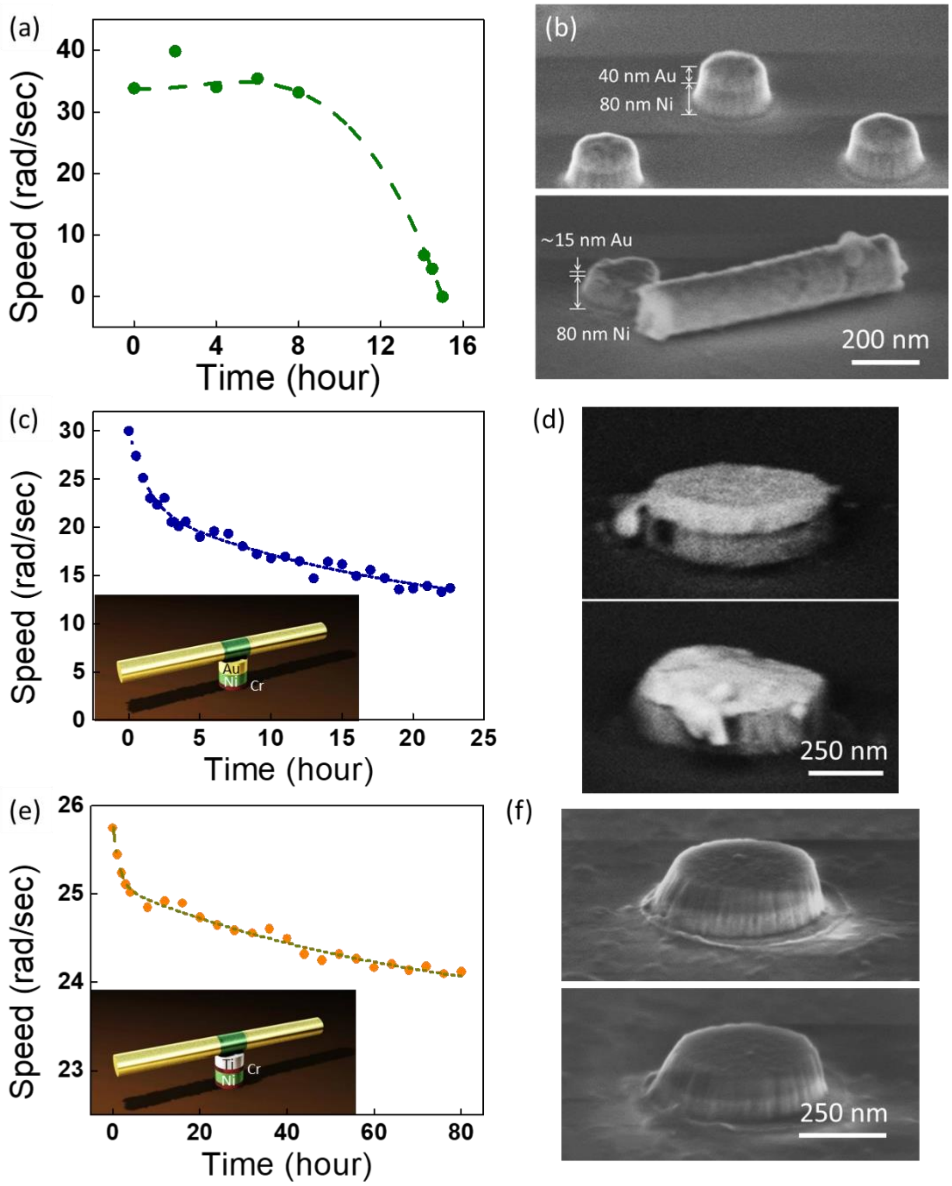
(a)
Speed (rad/sec)
40
30
20
10
0
0
4
8
12
16
Time (hour)
(b)
40 nm Au
80 nm Ni
~15 nm Au
80 nm Ni
200 nm
(c)
Speed (rad/sec)
30
25
20
15
10
5
0
0
5
10
15
20
25
Time (hour)
Au
Ni
Cr
(d)
250 nm
(e)
Speed (rad/sec)
26
25
24
23
0
20
40
60
80
Time (hour)
Ti
Cr
Ni
(f)
250 nm

Figure 2.5: Rotation speed *versus* time, and SEM images of the as-made nanobearings (top) and the nanobearings after long-term rotation (bottom). inset: schematic diagram of the nanomotors. (a-b) Rotor: Au (350~400 nm)/Ni (100 nm)/Au (350~400 nm), 165 nm in diameter; bearing: 200 nm in diameter, thin-film stack of Au (40 nm)/Ni (80 nm)/Cr (6 nm). Reproduced with permission.[95] Copyright 2014, Macmillan Publishers Ltd. (c-d) Rotor: Au (1.8 μm)/Ni (500 nm)/Au (1.8 μm), 165 nm in diameter; bearing: 500 nm in diameter, thin-film stack of Au (60 nm)/Ni (80 nm)/Cr (6 nm). (e-f) rotor: Au (1.8 μm)/Ni (500 nm)/Au (1.8 μm), 165 nm in diameter; bearing: 500 nm in diameter, thin-film stack of Ti (60 nm)/Cr (6 nm)/Ni (80 nm)/Cr (6 nm). Reproduced with permission.[96] Copyright 2015, Royal Society of Chemistry.

The size of the second type of nanomotors is larger for both rotor and bearing components. The nanomotors consist of a 165-nm-diameter nanowire rotor [Au (1.8 μm)/Ni (500 nm)/Au (1.8 μm)] and a 500-nm-diameter bearing [nanodisk made of a thin film stack of Au (60 nm)/Ni (80 nm)/Cr (6 nm)]. These larger nanomotors could rotate for as long as 22.6 hours and ~227,000 cycles in total [Figure 2.5(c)]. Similar to the case of ultrasmall nanomotors, during the 22.6-hour rotation, the average rotation speed decreased monotonically with time till the nanorotor was finally arrested on the bearing. Significant wear of the Au bearing was observed after 22.6-hour rotation as shown in the SEM images [Figure 2.5(d)]. Three nanomotors of this type were tested, which continuously rotated for 16.4, 21.1, and 22.6 hours, respectively. All of these motors showed the same decreasing trends in speed due to the wear of the bearings. The tested lifetime in the range of 16.4 to 22.6 hours demonstrated fairly good repeatability of our nanomotor devices.

To solve the wearing issues of the bearings after long-term rotation, we modified the design of the nanomotors to improve durability by replacing the Au layer with the much harder Ti (Element Vickers hardness: 970 MPa)[99] as the top layer of the bearing. This third type of nanomotors had a similar geometry to the second type, with a 500-nm-diameter contact area between the rotors and bearings. The rotors were Au/Ni/Au nanowires of 165 nm in diameter and 4.1 μm in length [Au (1.8 μm)/Ni (500 nm)/Au (1.8 μm)], and the bearings were 500-nm-diameter nanodisks made of thin film stacks of Ti (60 nm)/Cr (6 nm)/Ni (80 nm)/Cr (6 nm). The additional Cr layer between Ti and Ni was used to enhance the adhesion of the films. We rotated nanomotors on Ti-protected bearing both clockwise and counterclockwise. The rotation continued for 80 hours over 1.1 million cycles in total [Figure 2.5(e)]. The speed during the 80-hour rotation just decreased less than 10% from the original value. Both the duration and the number of cycles were around 4 times those of the Au-spaced nanomotors with a similar geometry. As far as we know, this is a new record in both duration and the number of cycles among reported rotary motors made from synthesized nanoparticles. After 80-hour rotation, the nanomotor was dissembled. It could be possibly due to a small bubble generated in the sealed chamber because of water evaporation. The SEM images do not show obvious thickness reduction of the Ti layer on top of the magnetic bearing [Figure 2.5(f)], indicating that the nanomotor could potentially rotate with a much longer lifetime than 80 hours. The results demonstrated that the replacement of the spacer layer with Ti can indeed increase the lifetime of nanomotors significantly.

2.6 ROTATION DYNAMICS DURING LONG-TERM OPERATION

We investigate the evolution of the nanoscale interactions between the rotors and bearings during long-term rotation of two types of nanomotors mentioned in Section 2.5, which have different contact materials on top of the bearings. We note that the rotation speed oscillated sinusoidally with a primary periodicity of 360° and the speed oscillation amplitude increased with time during long-term rotation. The evolution of the torques involved in the rotation was investigated, which governs the observed rotation dynamics, device wear, and lifetime.

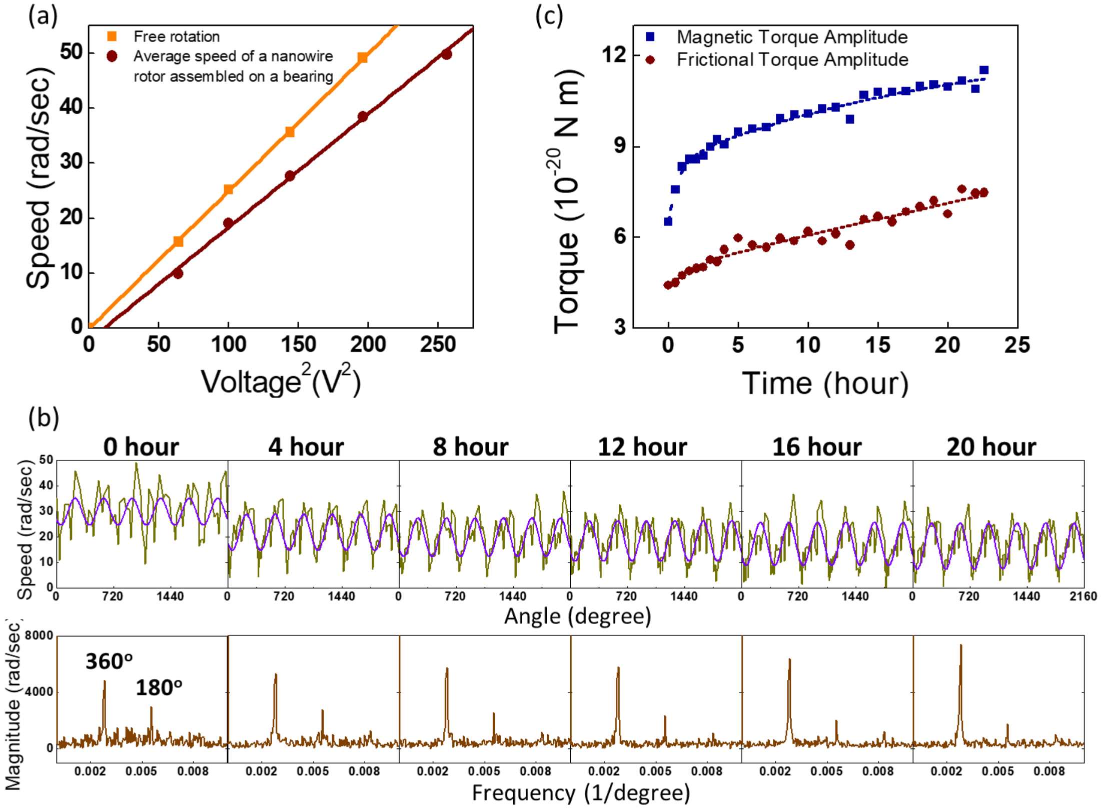

Figure 2.6: (a) Average rotation speed *versus* applied voltage^2 for nanowire rotors (wine red) and free suspending nanowires (orange). (b) Rotation speed *versus* angular position at different times and the corresponding Fourier transform showing the primary periodicity. (c) The amplitude of the magnetic and frictional torques *versus* time during the 22.6-hour rotation. Reproduced with permission.[96] Copyright 2015, Royal Society of Chemistry.

In brief, five torques could be identified in the system. The magnetic forces that anchor the nanorotors on the bearings result in angle dependent magnetic (τ_M) and frictional torques (τ_f). The nanomotors are rotated by the electric torque (τ_e) induced by the external *E*-field. The electric torque depends on the relative polarization of the nanowire in the water suspension and is proportional to the square of the *E*-field intensity (E^2) as well as the square of the AC voltage (V^2) ($\tau_e \sim V^2$).[100] Noteworthy, the external *E*-field also induces electric polarization between the metallic rotor and bearing and results in a non-negligible induced torque ($\tau_{e\prime}$), which is also proportional to V^2. Also, we need to consider the viscous torque (τ_η) from the water medium given by:[101]

$$\tau_\eta = a\omega = \frac{1}{3}\omega\pi\eta l^3 \frac{N^3-N}{N^3\left[\ln\left(\frac{l}{Nr}\right)+0.5\right]} \text{ [N·m]} \qquad (2.1)$$

where ω is rotation speed, η is the viscosity of DI water, a is a constant for a nanorotor with a radius of r, length of l, and the number of segments N. The segments are not separated by the composition and set as $N = 2$ in this study for calculation purpose only. The aforementioned five torques balance in a nanomotor and can be given as[102] $\tau_\eta = \tau_e + \tau_{e\prime} + \tau_M + \tau_f$. It can be rewritten as $a\omega = bV^2 + cV^2 + \tau_M + \tau_f$, where b and c are constants and the sum of b and c can be readily determined from the slopes of ω-V^2 for the rotation of a nanowire rotor assembled on a bearing in Figure 2.6(a).

To calculate the magnetic forces and torques, we employed a simplified magnetic dipole-dipole model with the horizontal magnetic moments of the nanowire and bearing taken as m_1 and m_2, respectively.[103] The analytical solution of the magnetic torque and force can be readily determined as below:[102]

$$\tau_M(r, \Theta, m_1, m_2) = \mu_0(m_1 m_2 \sin\Theta)/(4\pi x^3) \qquad (2.2)$$

$$F_M(r, \Theta, m_1, m_2) = 3\mu_0(m_1 m_2 \cos\Theta)/(4\pi x^4) + f \qquad (2.3)$$

where μ_0 is the magnetic permittivity of vacuum, Θ and x are the angle and the separation distance between m_1 and m_2, respectively, and f is the force due to the non-angle-dependent vertical magnetic moments and other factors. Theoretical research indicates that the frictional force (F_f) in nanoscale contacts should linearly or sub-linearly increase with the load depending on the nature of the contact.[104-108] Therefore, the frictional torque (τ_f) due to the angle-dependent magnetic force (F_M) should have a dominating factor proportional to $(\cos\Theta)^z$. Experimentally, we found the rotation speed of nanomotors showed a strong 360° ($z = 1$) periodicity as given in the Fourier transform in Figure 2.6(b). Also note that nanomotors did not have clear periodicities related to $z < 1$, (*e.g.*, $z = 2/3$, sublinear dependence, 480° periodicity for a non-adhesive single-asperity contact according to theoretical study[105]), although a low-level 180° periodicity (corresponds to $z = 2$) was found and could be attributed to axial rolling of the nanorotor due to small transverse magnetic moments possibly existing in the nanowires.[97] This suggests that the frictional force that contributes to the fluctuation of the rotation speed of the nanomotors should have a 360° periodicity. Then $z = 1$. Therefore, the frictional force (F_f) should be linearly proportional to the loading force.

In such a case, according to theoretical study, the nature of the contact in our nanomotors is multi-asperity and non-adhesive.[108] In the multi-asperity model, a contact between objects consists of multiple much smaller contacting points. If they are non-adhesive, the actual contact area is proportional to the loading force.[41] Also the frictional force is proportional to the actual contact areas. Therefore, the frictional force linearly depends on the loading force in the non-adhesive multi-asperity mode. We note that the nature of contacts in our nanomotors is consistent with that of the non-adhesive multi-asperity conditions. The surfaces of neither the rotors nor the bearings are perfectly smooth and the size of the contacts is at least 500 nm in diameter. The rotors and bearings can hardly form a single asperity contacting point when having relative motions. Multiple much smaller contacts are expected between the rotors and bearings. Moreover, the adhesion in the contacts is also low due to the natural lubrication effect of liquid when the nanomotors operate in an aqueous solution. As a result, the sum of the magnetic and frictional torques can be readily written as, $\tau_M + \tau_f = d\sin(\theta - \theta_M) + e\cos(\theta - \theta_M) + g$, where d, e, and g are constants, θ and θ_M are the angular positions of magnetic orientation of the nanowire and the nanobearing, respectively, and $\Theta = \theta - \theta_M$. Therefore, we can obtain:

$$a\omega = d\sin(\theta - \theta_M) + e\cos(\theta - \theta_M) + g + (b + c)V^2 \qquad (2.4)$$

By fitting the oscillating speed of the nanomotors during the long-term rotation according to Equation (2.4), the time-dependent coefficients of d, e, and g can be readily determined. The videos recording the long-term rotation were analyzed by a professionally developed software based on classical image recognition techniques, which generates the raw data of angle *versus* frame. The average speeds of nanomotors were calculated by linearly fitting of plots of angle *versus* time at tested time intervals, while the instant speeds were obtained by the first derivative of the angle-time curves. The Equation (2.4) could be rewritten into:

$$\omega = \frac{d}{a}\sin(\theta - \theta_M) + \frac{e}{a}\cos(\theta - \theta_M) + C \qquad (2.4)$$

where $\mathrm{C} = (g + (b + c)V^2)/a$. The constant a was calculated as $1.49 \times 10^{-20}\ N \cdot m \cdot sec/rad$ for a rotor of 165-nm-diameter Au (1.8 um)/Ni (500 nm)/Au (1.8 um) nanowire, and the magnetic orientation angles of the nanobearing θ_M were from the initial aligned angle of the rotor. With known constants of a a and initial aligned angle θ_M, the value of magnetic torque amplitude d and frictional torque amplitude e could be readily obtained by fitting the speed-angle curves (20 sequential rotation cycles) with Equation (2.4). The values of d and e are amplitudes of the angle-dependent magnetic and frictional torques, respectively as shown in Figure 2.6(c). We note that there are high frequency noises in addition to the strong 360° periodicity of the rotation speed, which can be attributed to factors such as Brownie motions, uncontrolled surfaces roughness and imperfectness of the nanowires and magnetic nanobearing, as well as instant liquid agitations. These factors cannot be easily modelled and not considered in the fitting Equation (2.4). They contributed to the slight differences of the fitting curves from the experimentally determined rotation speed in Figure 2.6(b). However, the strong 360° periodicity of the rotation speed can be just attributed to the magnetic and the resultant frictional torques in the nanomotors, and make the method feasible. As shown in Figure 2.6(c), both the amplitude of the magnetic torque (*d*) and frictional torque (*e*) monotonically increase during the 22.6-hour rotation. Our calculation shows that the levels of the magnetic and frictional forces are 1.0 ~ 2.2×10^{-12} and 0.9 ~ 1.5×10^{-13} N, respectively. Herein, the amplitude of magnetic load force is calculated according to the following equation:

$$F_M = 3\mu_0 m_1 m_2/(4\pi x^4) \qquad (2.5)$$

With known magnetic torque and the separation distance at the beginning of the rotation, the value of $3\mu_0 m_1 m_2/(4\pi)$ can be readily calculated. For instance, it is calculated as $1.24\times10^{-39}\ N\cdot m^4$ for the nanomotors with 500-nm-diameter Au as the top layer of the magnetic bearing. Now, with the experimentally determined time-dependent magnetic torque (F_M) and the calculated value of $3\mu_0 m_1 m_2/(4\pi)$, the instant separation distance (x) as well as the amplitude of the angle-dependent-component of the magnetic load can be readily determined by Equation (2.3). The amplitude of the frictional force is estimated from $F_f = \tau_f/l$, where l is the diameter of the contact area. Therefore, the amplitudes of the frictional force could be calculated with the known frictional torque.

Even with such low interfacial forces, significant wear of the bearing was observed after 22.6-hour rotation. It was found that the Au spacing layer had an obvious thickness reduction and deformation. Especially, the wear on the bottom right corner of the magnetic bearing was more severe than the other regions. It could be attributed to the center of rotation of the nanorotor located close to that region of the magnetic bearing, *i.e.*, the bottom right corner [Figure 2.7(a)]. An average thickness of ~ 26 nm in the most worn region was obtained by the Atomic Force Microscopy (AFM) characterization [Figure 2.7(b)]. We designed nanomotors with the length of the Ni segments of the nanowires the same as the diameters of magnetic nanobearings so that Ni segments could be in full contact with Au spacer layer during rotation. However, the rotation of rotors may not always perfectly center on the bearings. It could be due to the strong magnetic dipole interaction between tips of the magnetic segment of the nanowire and edge of the magnetic bearing, causing the rotation of magnetic segment off the center. From the distribution of the rotation center of the nanomotor in Figure 2.7(a), we can find two extremes: (1) rotation at the center, (2) rotation around the edge. If the rotation center is at the center of the bearing, Ni segment is always on Au during the entire rotation cycle. If it is at the edge, we can say that the Ni segment is on Au for at least 50% of a rotation cycle. Therefore, we could roughly estimate that Ni is in full contact with Au for 75% of the rotation time.

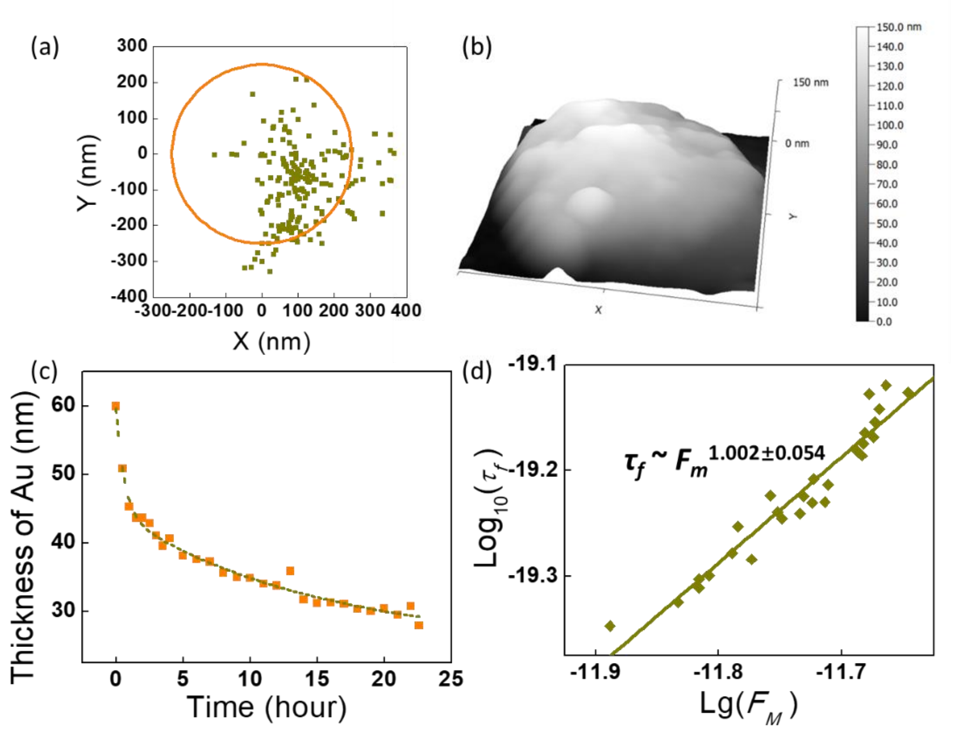

Figure 2.7: (a) Instant center of rotation of the nanomotor primarily formed at the bottom right corner of the magnetic nanobearing (at 22.6 hours). (b) AFM image obtained by taping mode showing the wear of the magnetic bearing after 22.6-hour rotation. (c) Time-dependent change of the thickness of the Au spacer layer determined from the evolving magnetic torque during the rotation. (d) Log-log plot of the amplitude of frictional torque *versus* that of the magnetic force showing a power dependence of ~1 (slope of the plot). Reproduced with permission.[96] Copyright 2015, Royal Society of Chemistry.

Although there is a certain extent of Au-on-Au contact during the rotation, neither Ni nor Au segments on the rotors have clearly observable wear according to our SEM characterization. We attribute this to two factors: (1) it is found that the hardness of electroplated Au (~80 HV) can be 33% higher than that of the high-vacuum evaporated Au (~60 HV) due to impure elements incorporated during the electrodeposition process.[109-110] Also when making the multi-segment nanowires, we altered electrolytes in the same container after careful washing with D. I. water. These factors both make the Au segments in the nanowires less pure and harder than that of evaporated Au; (2) the intermetallic diffusion at the interface of Au and Ni segments of the nanowire can greatly enhance the hardness of Au next to the Ni segment. It is reported that 1 wt% Ni could increase the hardness of Au by 30% and 2 wt % Ni could increase the hardness by 80%.[111-112] The hardness of electroplated Ni (200-500 HV) is higher than that of either electrodeposited or evaporated Au.[113]

According to Equations (2.2-2.4), it can be readily understood that the increase of the values of d and e during nanomotors rotation is due to the wear and thickness reduction of the Au separation layer. The magnetic and frictional torques increase with the decrease of the separation distance (x) between the two magnetic moments in the rotor and bearing, with a dependence of $1/x^3$ and $1/x^4$, respectively. Note that the separation distance (x) is calculated from the middle of the Ni segment of the nanowire to the center of the magnetic Ni layer in the bearing. From Equation (2.4) and the time-dependent amplitude of the magnetic torque (d), we can readily determine the separation distance (x) and thus the thickness of the Au layer during the rotation of the nanomotor as shown in Figure 2.7(c). The final thickness of the Au layer was determined as 29 nm, which well agreed with the average thickness obtained by the AFM characterization. The consistent calculation and experimental results well support our modeling. Moreover, we found the amplitude of the magnetic load and the frictional torque obtained from experiments linearly depend on each other as shown in the log-log plot in Figure 2.7(d). This provides another proof of our understanding and modeling of the system, where the frictional torque linearly increases with the load.

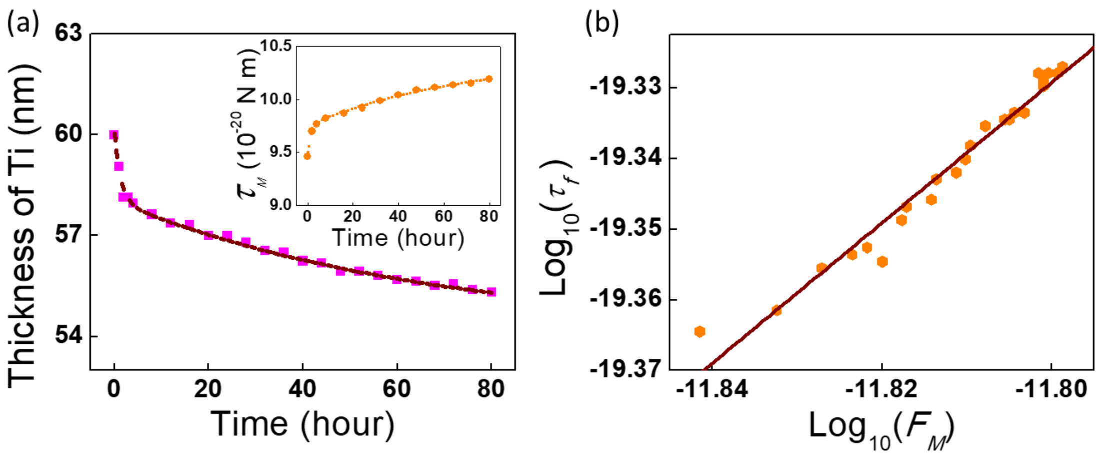

Figure 2.8: (a) Time-dependent change of the thickness of the Ti spacing layer determined from the magnetic torque during rotation of the nanomotor, insert: the amplitude of the angle-dependent magnetic torque *versus* time. (b) Log-log plot of the amplitude of frictional torque *versus* that of the magnetic force showing a power dependence of ~1 (slope of the plot). Reproduced with permission.[96] Copyright 2015, Royal Society of Chemistry.

How much heat is generated due to friction during the long-term rotation of this nanomotor? Would this heat result in the temperature change around the nanomotor? Since all the work done by the friction force transfers into heat, the friction heat power is given as:

$$P_{heat} = \tau_f \cdot \omega \qquad (2.6)$$

Knowing the maximum friction torque τ_f of $7.5 \times 10^{-20}\ N \cdot m$ and the maximum rotation speed ω of 30 rad/sec for this nanomotor, the maximum friction heat power

P_{heat} is calculated as $2.25 \times 10^{-18}\,J/sec$. Would the heat dissipate quickly or accumulate to increase the temperature? Herein we assume that the nanomotor is rotated in the center of a water surrounding in hemisphere shape with diameter (R) of 2 mm, and the surface of water droplet is at room temperature. The temperature difference at equilibrium from the nanomotor to the boundary of water surrounding can be estimated as:

$$\Delta T = \int_{r_0}^{R} \nabla T dr = -\int_{r_0}^{R} \frac{q}{\kappa} dr = -\int_{r_0}^{R} \frac{P_{heat}}{\kappa \cdot 2\pi r^2} dr \qquad (2.7)$$

where ∇T is temperature gradient, r_0 is the diameter of the nanomotor bearing (250 nm), κ is thermal conductivity of water (0.6 W/m/K), and q is heat flux. Therefore, ΔT is calculated as $-2.39 \times 10^{-12}\,K$, indicating that the temperature change is ignorable during the long-term rotation.

For the long-term rotation of nanomotors with Ti as the top layer of the bearing, the time-dependent magnetic and frictional torques were also determined from the rotation speed. Similar to that found in the Au-supported nanomotor, the magnetic torque monotonically increases with time [inset of Figure 2.8(a)]. The frictional force goes up with the magnetic torque with a power-law dependence of 0.994±0.036 [Figure 2.8(b)]. This further confirms the consistency with the non-adhesive multi-asperity friction theory we discussed previously. As mentioned in Section 2.5, after 80-hour rotation, the nanomotor was dissembled, instead of being arrested on the bearing. Neither the magnetic bearing nor nanowire rotor was obviously worn after such a long-term rotation. The SEM images do not show obvious thickness reduction of the Ti layer on top of the magnetic bearing, consistenting with the prediction of only 4.68 nm decrease in thickness derived from the time-dependent magnetic torques with our modeling. From the above analysis, we can estimate the wear rate of the motor as 0.0585 nm/hour. This value can assist to estimate the lifetime of the micromotors as 632 hours (26.3 days) given the final thickness of 29 nm of the separation layers (Au) before the nanowire rotor is arrested due to the increased magnetic/frictional forces between the rotor and bearing. Alternatively, by directly extrapolating the thickness *versus* time curve for the Ti micromotor in Figure 2.8(a), the lifetime of such micromotors can be estimated as 1088 hours (45.3 days). Both estimation methods suggest the lifetime is ultralong, *i.e.* at least hundreds of hours. Note that the estimations have simple assumptions that the frictional coefficients of Au and Ti are the same, the wear rate is constant, and the nanowire rotors do not wear. A more accurate lifetime can be calculated if we know the wear rate of the nanowire rotor with consideration of the reduced magnetic force and thus frictional force during its wear. Herein, employing mechanically hard materials between the contact of rotors and bearings, we significantly reduced the wear of the nanomotors and improved the operation lifetime. The achievement is critical for practical applications of this new type of nanomotors.

Chapter 3: Chemical nanomotors manipulated by the electric tweezers‡

Chemical micro/nanomotors represent an important class of autonomous nanomotors that convert chemical energy into mechanical motions, mimicking biomolecular motors in nature.[59-62, 114-118] Billions of chemical nanomotors can be facilely fabricated by using a variety of techniques, such as electrodeposition into nanoporous templates and electron beam deposition on monolayer nanospheres.[57, 119] They self-propel by harvesting chemical energies from fuels in suspension, such as hydrogen peroxide.[118, 120] Recently, substantial research efforts have been focused on strategically designing and fabricating chemical nanomotors with an array of compositions and geometries, such as bimetallic nanorods,[118, 120-121] catalytic microtubes,[122-124] and Janus particles.[68, 125-127] The efforts lead towards dramatic improvement of propulsion speeds up to hundreds of μm/sec (or 100 body lengths per second),[120-122] and readiness in harnessing energy from a variety of fuels, such as hydrazine,[128] urea[129-130] and even pure water.[61, 126, 131] More importantly, vast applications of chemical nanomotors have been demonstrated, such as on-chip cargo transport,[68, 70] drug delivery,[132-133] microchip repair,[134] nanolithography,[135] biomolecular sensing and *in-vivo* disease treatment.[136]

However, it remains challenging to align chemical nanomotors with high precision and modulate their moving speeds facilely and instantly. The ability to achieve this could open unprecedented opportunities. Innovatively, magnetic fields have been exploited in guiding chemical nanomotors, however, this strategy requires the integration of magnetic elements in the nanomotors and precise alignment of magnetic moments.[68, 70] Also, to generate magnetic forces, bulky electromagnets are often employed, which could be the bottleneck when developing portable nanomotor based devices. Acoustic tweezers have been used in guiding chemical nanomotors to aggregate and disperse,[137] while, the resolution in manipulation is restricted by the large wavelength of acoustic waves. Besides controlling the orientation of chemical nanomotors, it is of paramount importance to facilely tune their speed. Several unique approaches have been exploited to control locomotion speed of chemical nanomotors. With the strong dependence on chemical reactivity, the speed of chemical micro/nanomotors can be tuned by localized stimuli, including fuel concentration,[118] temperature,[138] and light illumination.[126, 139-141] Furthermore, by applying electrical potentials to create chemical gradient,[142] or generating ultrasonic waves,[137, 143] the speed of micro/nanomotors can also be modulated. However, it remains difficult to realize both the guiding and speed tuning of chemical nanomotors with high accuracy, facileness, and in an all-on-chip manner.

---

‡ Portions of this chapter have been previously published in **J. Guo**, J. J. Gallegos, A. R. Tom, D. Fan, ACS Nano, 12, 2, 1179-1187 (2018). As the first author of the manuscript, J. Guo designed and performed the experiments, analyzed the data and wrote the first draft of the manuscript. He also mentored undergraduate students J. J. Gallegos and A. R. Tom, who are co-authors of this manuscript, in the sample fabrication and data analysis. As the faculty author, Professor D. Fan conceived the research and supervised the project. She analyzed the results and revised the manuscript.

In this chapter, we report a versatile approach for manipulating chemical nanomotors with high precision and facileness. The work is based on strategically combined AC and DC *E*-fields applied *via* a 3-D orthogonal microelectrode setup.[144] Here, the DC *E*-field tunes the transport speed *via* electrophoretic and electroosmosis effects. The AC *E*-field guides the alignment independently *via* electric torques on the induced dipoles of nanomotors. By applying the combined AC and DC *E*-fields in 3-D, chemical nanomotors can instantly align, transport along defined directions, start and stop, and change speeds on demand. The involved various nanoforces governing the motions are investigated. Leveraging the high precision in the alignment, the linear dependence of speed on the inverse of size of nanomotors ($1/l$) down to submicrometers, is experimentally determined, confirming previous theoretical predictions.[62] Finally, the manipulation of chemical nanomotors by *E*-fields is demonstrated for two applications: the dynamic loading, transport, and unloading of micro-targets to pre-patterned microdocks; and assembling and integration of a chemical nanomotor on a rotary NEMS to power its continuous operation.

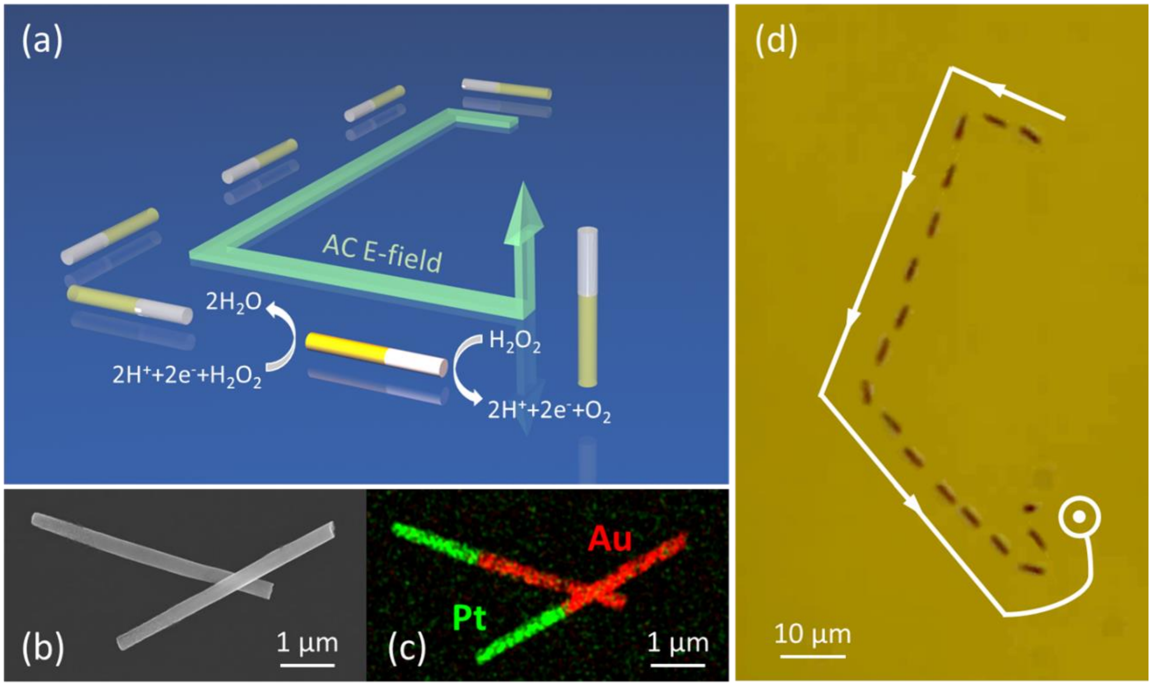

Figure 3.1: (a) Schematic diagram of 3D manipulations of Pt-Au chemical nanomotors in H_2O_2 fuel with AC *E*-fields. (b) SEM and (c) EDS images of Pt-Au chemical nanomotors (250 nm in diameter, 5 µm in length; consisting of 2-µm Pt segment and 3-µm Au segment). (d) Overlapped snapshots of a chemical nanomotor guided by AC *E*-fields. Reproduced with permission.[145] Copyright 2018, American Chemical Society.

3.1 STRATEGY OF MANIPULATION

The demonstrations of transport guidance and speed modulation of chemical nanomotors by *E*-fields are carried out by using the classical Pt-based bimetallic nanorod motors as a model system [Figure 3.1(a)]. Arrays of multi-segmented Pt-Au nanorod motors are synthesized with controlled lengths and diameters by electrodeposition into nanoporous templates in a three-electrode setup, which is the same as the fabrication of nanowire rotors mentioned in Section 2.2.[118, 146] Scanning electron microscopy (SEM) and energy-dispersive X-ray spectroscopy (EDS) in Figure 3.1(b-c) confirm the uniform cylindrical morphology, controlled size and composition of the Pt-Au chemical nanomotors.

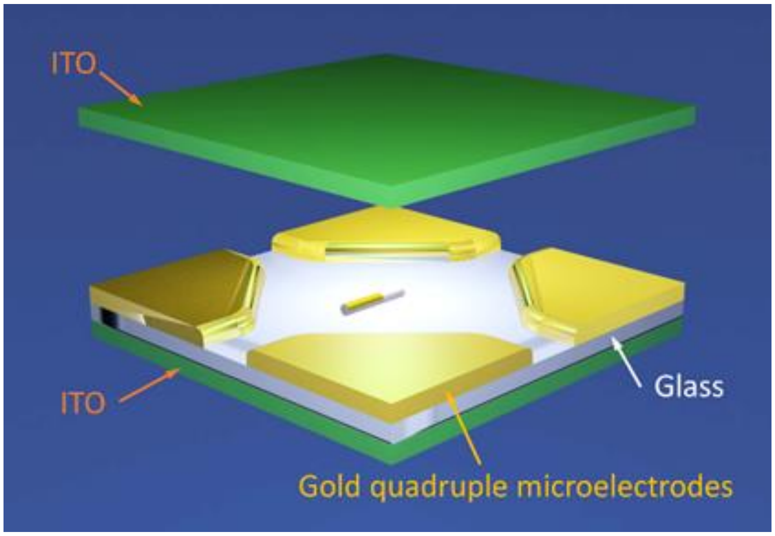

Figure 3.2: Scheme of 3-D orthogonal microelectrode setup. Reproduced with permission.[145] Copyright 2018, American Chemical Society.

A software interfaced 3-D orthogonal microelectrode setup is designed and constructed for guiding the chemical nanomotors as shown in Scheme Figure 3.2. Applying an AC *E*-field on the in-plane quadruple microelectrodes, the chemical nanomotors can be instantly aligned along the direction of the AC *E*-field and move autonomously in the direction with the Pt segment as the front, as shown in the schematic diagram in Figure 3.1(a) and overlapped images in Figure 3.1(d). We found that an AC peak-to-peak voltage of 10 V is sufficient to align the chemical nanomotors and to guide their motions. When superimposing a DC *E*-field on the AC *E*-field, the speed of the nanomotors can increase or decrease instantaneously, and even reverse the moving direction. We characterize the manipulation in detail in the following to unveil the fundamental interactions between the nanomotors and *E*-fields.

3.2 DIRECTIONAL GUIDANCE OF CHEMICAL NANOMOTORS

First, we investigate the dependence of the speed of the chemical nanomotors on the concentration of hydrogen peroxide fuel (H_2O_2), both with and without *E*-fields. The average speed of the chemical nanomotors is determined statistically from the behaviors of 10 nanomotors for 10 seconds. The instantaneous velocity vector of nanomotors $\vec{\boldsymbol{v}}$, which is calculated by the position shift in each frame times frame rate, could be separated into an axial component along the long axis of nanorod $\vec{\boldsymbol{v}}_x$ and a radial component perpendicular to the nanorod $\vec{\boldsymbol{v}}_y$. The axial velocity component $\vec{\boldsymbol{v}}_x$ is contributed by the self-electrophoresis of the catalytic nanorod and also the Brownian motion, while the radial velocity component $\vec{\boldsymbol{v}}_y$ is only contributed by the Brownian motion:

$$\vec{\boldsymbol{v}}_x = \vec{\boldsymbol{v}}_{SEP} + \vec{\boldsymbol{v}}_{Brownian-x} \qquad (3.1)$$

$$\vec{\boldsymbol{v}}_y = \vec{\boldsymbol{v}}_{Brownian-y} \qquad (3.2)$$

Since the instantaneous velocity of Brownian motion has a normal distribution with the mean value of zero, the mean value of the axial velocity component $\vec{\boldsymbol{v}}_x$ in a sufficient period is only contributed by the average self-electrophoretic speed of catalytic nanorod. In this way, we calculated the average self-electrophoretic speed in 10 seconds for each chemical nanomotors. We followed the movements of nanomotors for 10 seconds due to the limited view of the field. In order to analyze the velocity accurately, the movements of nanomotors were recorded by using a relatively high magnification objective setup (50× objective), which restricted the view of the field to 128 μm × 102.4 μm. All the tests for velocity analysis were conducted in the first several minutes after the dispersion of nanomotors in H_2O_2 solutions. The velocity of chemical nanomotors decreases by less than 20% in 30 minutes in our setup. A similar phenomenon is found for those dispersed on glass substrates.

As shown in Figure 3.3(a), regardless whether the *E*-field is applied or not, the speed of the nanomotors increases with the concentration of H_2O_2 and reaches a plateau, which can be attributed to the saturation of catalytic active sites on the nanomotors in high concentration H_2O_2 fuels.[118] Consistently, we find that the speed of these chemical nanomotors under AC *E*-fields is always higher than those without AC *E*-fields. Furthermore, the speed of all nanomotors, regardless of their moving directions, increases when applying a uniform AC *E*-field. Neither the electroosmosis flows nor the induced dielectrophoretic forces could result in the observed behavior, so the dominating factor is the reduction of rotational Brownian motions of nanomotors due to the alignment by AC *E*-fields.

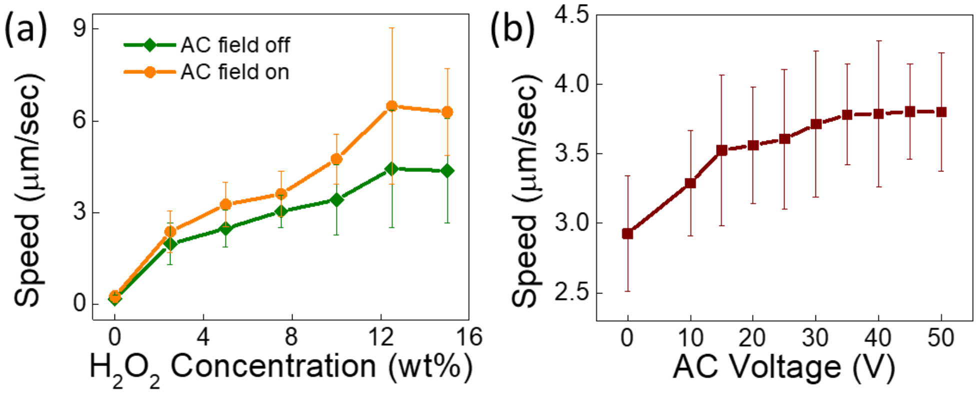

Figure 3.3: (a) Speed of chemical nanomotors *versus* concentration of H_2O_2 with/without AC *E*-fields (5 MHz, 15 V). (b) Speed *versus* peak-to-peak voltage of AC *E*-fields (500KHz) in 7.5 wt% H_2O_2 solution. Reproduced with permission.[145] Copyright 2018, American Chemical Society.

Our experimental results and analysis support this understanding. First, we determine the speed of nanomotors as a function of AC frequency and voltage. It is found that the average speed of nanomotors monotonically increases with AC frequency before reaching a constant at around 500 KHz and 20 V (peak to peak, same for the following AC voltages). At a fixed AC frequency, *i.e.* 500 KHz, the average speed also increases with AC voltage amplitude until reaching a constant at 30 V as shown in Figure 3.3(b). The voltage dependence can be readily understood from the increase of electric torque (τ_e) with applied *E*-field (*E*), which counters the rotational Brownian motions and thus enhances the degree of alignment of a nanomotor, given by:[100]

$$\tau_e = \frac{8\pi l r^2}{3} \cdot P \cdot E^2 \cdot sin2\theta \qquad (3.3)$$

where *l* and *r* are the length and radius of a nanomotor, respectively; θ is the angle between the long axis of nanomotor and the *E*-field; *P* is a value determined by the permittivity and conductivity of the medium and nanomotor as well as the AC frequency. We observe a leveling off of the moving speed when the voltage is adequately high, *i.e.* above 30 V, as shown in Figure 3.3(b). It could be understood that when the electric torque is sufficiently high, the rotational Brownian motion is suppressed to an extent that the increase of speed with voltages is too small to be determined compared to the statistic distributions of the speed of tested nanomotors.

By analyzing electric torques, we can also attribute the observed dependence of nanomotor speed on AC frequency to the suppressed rotational Brownian motions. We experimentally determine electric torques as a function of angular positions when aligning nanomotors at 5 KHz to 50 MHz with Equation (3.3). The τ_e exerted on the chemical nanomotors at an angle of θ can be readily obtained from the angular velocity (ω) *versus* angle (θ), since the viscous torque (τ_η) instantly counters the electric torque (τ_e) as given by $\tau_e = \tau_\eta$ in low Reynolds number environment. Here, the viscous drag torque τ_η on a rotating nanorod is calculated as follows:[147]

$$\tau_\eta = \frac{1}{3}\omega\pi\eta l^3 \frac{N^3 - N}{N^3(\ln\frac{l}{Nr} + 0.5)} = K_1\,\omega \;\; (N\,m) \qquad (3.4)$$

where η is the viscous coefficient of suspension medium and N is the number of nanorod segments, taken as 2 in this calculation. For the nanomotors used in our experiments, the constant K_1 is determined as 2.50×10^{-20}. Therefore, we plot and fit the angular velocity as a function of θ at different frequencies as shown in Figure 3.4. Based on the fitting results, we can readily obtain the coefficient of τ_e at different AC frequencies as shown in Figure 3.4(f). It can be readily found that the dependence of nanomotor speed on AC frequency well matches the dependence of electric torque applied on nanomotors *versus* AC frequency. It well supports the key contribution of alignment by AC *E*-fields to the observed enhanced speed of nanomotors.

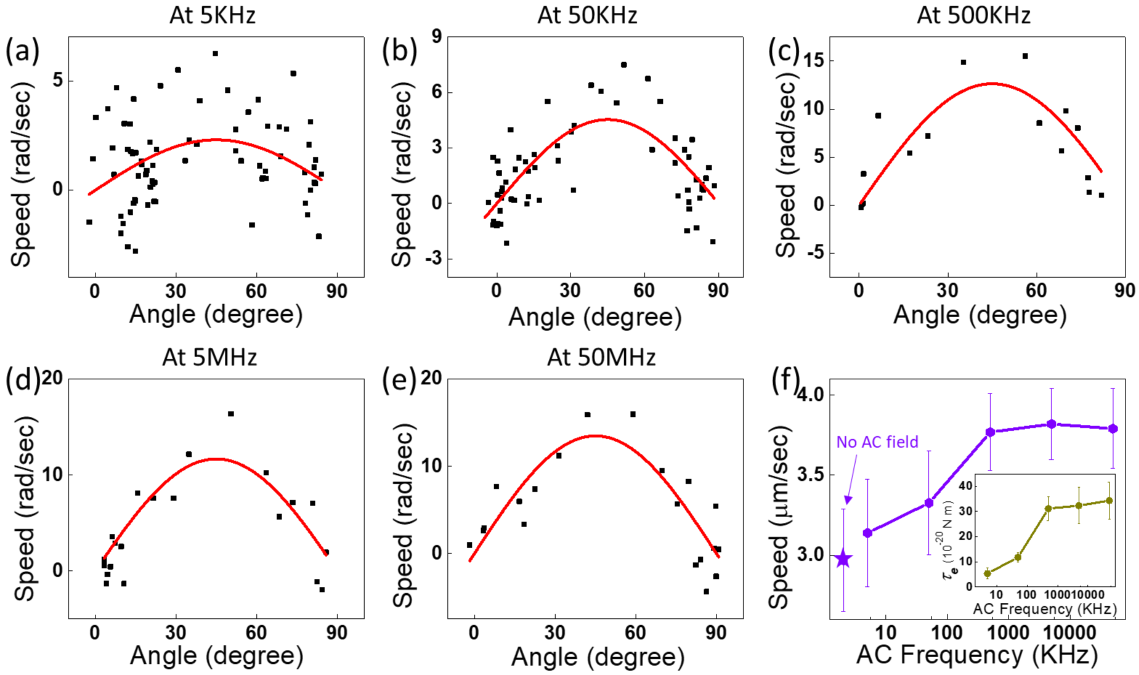

Figure 3.4: (a-e) Angular velocity (ω) of nanomotors *versus* angle (θ) during the alignments at different AC frequencies. (f) Speed *versus* frequency of AC E-fields (20 V) in 7.5 wt% H_2O_2 solution. Inset: electric torque *versus* frequency of AC E-field. Reproduced with permission.[145] Copyright 2018, American Chemical Society.

Note that the present of ionic impurity, such as NaCl, decreases the τ_e due to the change of electric conductivity of suspension medium. As shown in Figure 3.4, the alignment torque of Au/Pt nanorod (4.8 μm in length) by AC E-field is lower at a higher concentration of NaCl. The coefficients of τ_e are calculated as $(31.19 \pm 4.78) \times 10^{-20}\ N \cdot m$ in DI water, $(11.88 \pm 1.45) \times 10^{-20}\ N \cdot m$ in 50 μM NaCl solution, and $(4.01 \pm 1.40) \times 10^{-20}\ N \cdot m$ in 500 μM NaCl solution, respectively. The nanorod could not be aligned any more if the concentration of NaCl solution reach 5 mM.

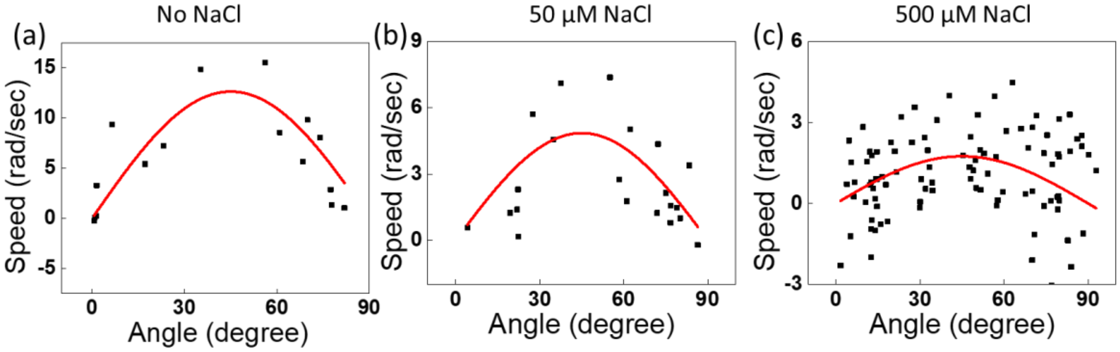

Figure 3.5: Angular velocity (ω) *versus* angle (θ) during the alignment of nanomotors by a AC E-field of 20 V and 500 KHz at different NaCl media. Reproduced with permission.[145] Copyright 2018, American Chemical Society.

With the uniform AC E-fields, we not only improve the alignment and speed of nanomotors as discussed as above, but also successfully guided chemical nanomotors in the vertical direction in a facile and all-on-chip manner. Nanomotors can move along prescribed trajectories in the 2-D X-Y plane, start and stop on demand, and even move vertically as shown in Figure 3.1(a). For nanomotors moving in the X-Y 2-D plane, it is known that the catalytic driving force balances with the drag force, given by:[147]

$$F_{catlytic\ drive} = F_{drag} = \frac{2\pi\eta l}{ln\,(l/r) - 0.5} v = K_2\, v\, (N) \qquad (3.5)$$

where v is the velocity of chemical nanomotors and the geometric factor $K_2 = 8.77 \times 10^{-9}$ for the tested nanomotors (5 μm in length and 250 nm in diameter). Note that the value of viscous coefficient η of suspension medium is estimated from that of pure water at room temperature, knowing that the change of viscous coefficient is less than 3% when the concentration of H_2O_2 is less than 10 wt%.[148] In the vertical direction, a catalytic nanorod made of Pt(2-μm)-Au(3-μm) experiences gravitational and buoyant forces of $4.85 \times 10^{-14} N$ and $0.24 \times 10^{-14} N$, respectively. Therefore, from Equation (3.5) and the experimental results of velocity *versus* fuel concentration (C_{H2O2}) shown in Figure 3.3(a), we can readily determine that the catalytic driving force of nanomotors is sufficiently high to realize the propulsion of the nanomotor in the vertical direction when the concentration of fuel (C_{H2O2}) is above 10 wt%. This analysis is validated by our experimental study. When C_{H2O2} is 12.5 wt%, where a driving force of $5.69 \times 10^{-14} N$ is determined by calculation, the chemical nanomotors indeed aligned and transported vertically, overcoming gravitation forces, and gradually disappeared from the view. While at a lower fuel concentration, *e.g.* when C_{H2O2} is 7.5 wt%, a vertically applied AC *E*-field can instantly align nanomotors vertically and stop the motions in 2-D planes. Here the driving forces due to catalytic reactions, calculated as $3.17 \times 10^{-14} N$, is not sufficient to propel the motors vertically. Both the demonstrations of 3-D manipulation at high fuel concentrations and “on/off” control of 2-D motion at low fuel concentrations offer considerable promise for versatile operations of these chemical nanomotors, opening many opportunities for applications. Such a strategy could also be applied for controlling photocatalytic nanomotors[126, 140] and self-propelled enzyme nanomotors.[60, 130]

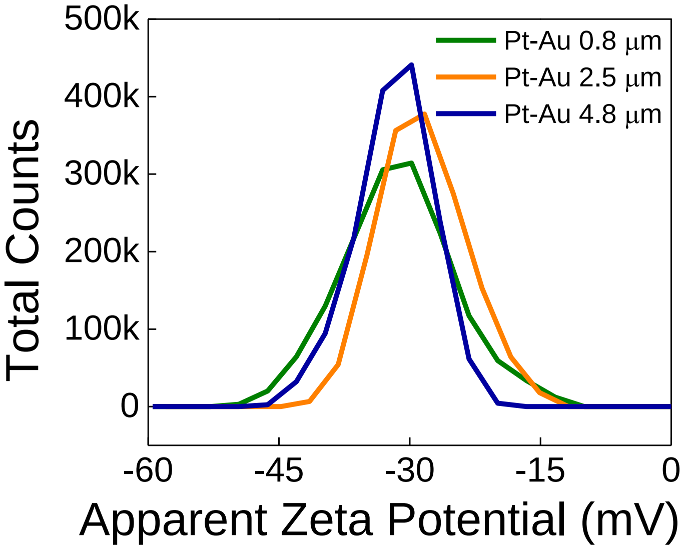

Figure 3.6: The Zeta potential measurement of Pt-Au nanorod chemical nanomotors of different lengths in DI water. The measurements were conducted by Dynamic Light Scattering Zetasizer Nano ZS, Malvern. The size range is from 1 nm to 5 μm. The Zeta potentials for nanomotors with lengths of 0.82, 2.50 and 4.78 μm are -31.28±6.64 mV, -28.50±5.03 mV and -31.77±4.43 mV, respectively. Reproduced with permission.[145] Copyright 2018, American Chemical Society.

3.3 SIZE-DEPENDENCE STUDY OF CHEMICAL NANOMOTORS

The high precision in the alignment of nanomotors by AC E-fields offers opportunities in studying and understanding the working mechanism of the self-propelled chemical nanomotors. The dominant propulsion mechanism of chemical nanomotors is suggested as self-electrophoresis based on the electro-catalytic decomposition of hydrogen peroxide.[149-150] In a recent model of a chemical nanomotor made of bimetallic nanorods, the velocity (v) due to self-electrophoresis is given by:[62]

$$v \sim \frac{\zeta_p \varepsilon \varepsilon_0}{\eta} E_{int} \sim \frac{\zeta_p \varepsilon \varepsilon_0 \Delta\phi}{\eta l} \qquad (3.6)$$

where ε is the relative dielectric constant of the suspension medium and ε_0 is the dielectric permittivity of free space. The self-generated E-field E_{int} is approximated as the potential drop $\Delta\phi$ divided by the length of the nanorods l and $\Delta\phi$ is determined by the chemical potential of the two metal segments of a nanomotor, which is considered as a constant with different lengths; ζ_p is Zeta potential of a nanomotor, independent of the size of the nanomotor (Figure 3.6). Therefore, we can readily find that the self-electrophoretic velocity (v) of a nanomotor should be inversely proportional to its length (l) according to Equation (3.6) as suggested by this model.

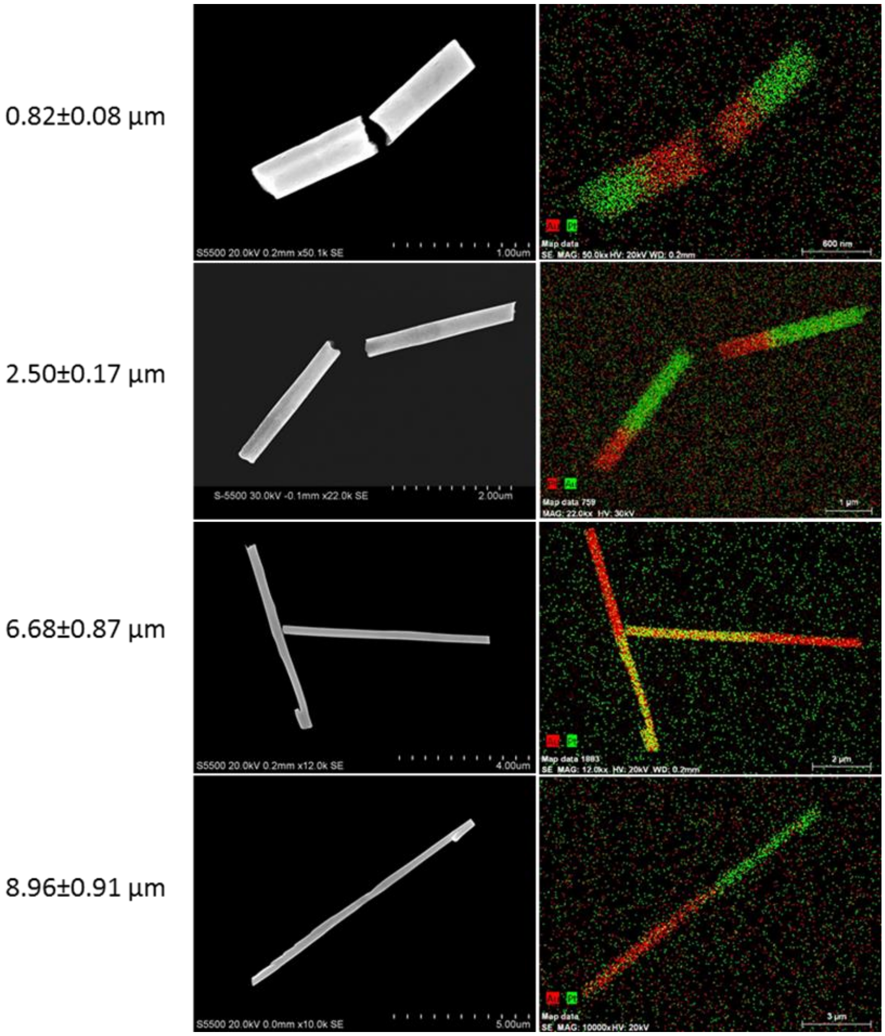
0.82±0.08 µm
2.50±0.17 µm
6.68±0.87 µm
8.96±0.91 µm
1.00um
600 nm
2.00um
1 µm
4.00um
2 µm
5.00um
3 µm

Figure 3.7: SEM (left) and EDS (right) images of chemical nanomotors of different lengths. Reproduced with permission.[145] Copyright 2018, American Chemical Society.

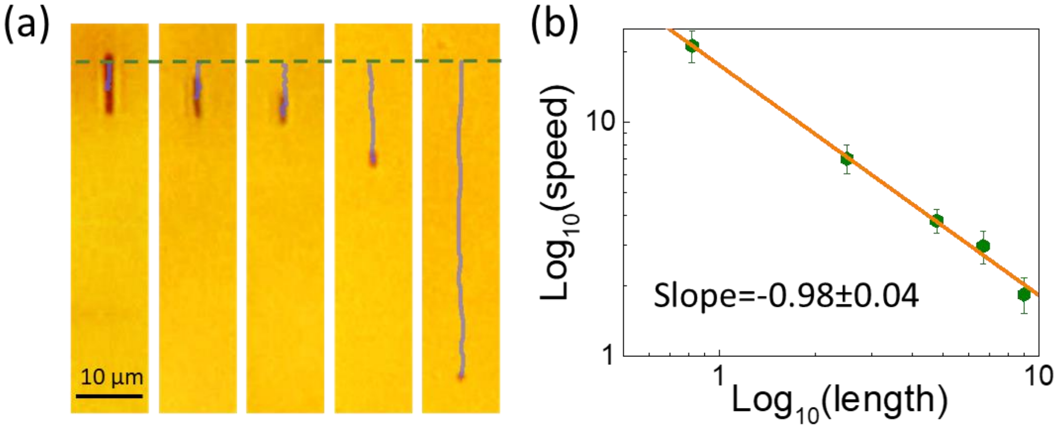

Figure 3.8: (a) Trace of chemical nanomotors of different length in 7.5 wt% H_2O_2 solution with AC *E*-fields (5 MHz, 15 V) in 2 seconds. The lengths of nanomotors (from right to left) are 0.82, 2.50, 4.78, 6.68 and 8.96 µm, respectively. The green dashed line shows the starting position. (b) Log-log plot of speed *versus* length of nanomotors in (a). The slope is -0.98. Reproduced with permission.[145] Copyright 2018, American Chemical Society.

Although in previous studies, it has been shown that the smaller the chemical nanomotors, the higher the moving speed, quantitative study has yet been carried out on the chemical nanomotors as predicted by the model.[62, 151] To experimentally determine the dependence of speed on size of nanomotors, the key is to precisely align nanomotors with controlled moving trajectories and to suppress noises due to Brownian motion. As shown in the above studies, AC *E*-field alignment provides a facile and effective tool, where the alignment is determined by the overall shape anisotropy of a nanomotor. Indeed, with AC *E*-fields, we can synchronously align chemical nanomotors with sizes ranging from 0.82 to 8.96 µm (Figure 3.7). These nanomotors with different sizes are designed with an identical length ratio of Pt:Au (~2:3). When suspending in H_2O_2 solutions, the shorter nanomotors exhibit higher moving speeds compared to longer ones [Figure 3.8(a)]. The speed and length of nanomotors follows an inverse proportional relationship as shown in the log-log plot with a slope of -0.98±0.04 in Figure 3.8(b). It indicates that the power law dependence of speed on size of nanomotors is approximately -1, which provides quantitative proof of the working mechanism proposed previously for nanomotors in the size range of 0.82 to 8.96 μm. This result points towards the great advantages of chemical nanomotors in achieving ultrahigh propulsion speed when made into ultra-small dimensions.[124, 152-153] The involved nanoforces, energy conversion efficiency, and influencing factors, such as impurities, of the chemical nanomotors have been well studied.[62, 87, 149-150] For instance, the velocity of nanomotors is inversely proportional to the electric conductivity of the suspension. Given the feasibility of the self-electrophoresis model, we expect the same ionic effect for the chemical nanomotors guided by the *E*-fields. Therefore, in some biological suspension media with high ionic concentrations and electric conductivities, *e.g.* cell culture media and cell washing media such as phosphate buffered saline, the chemical nanomotors have decreased (or even diminished) velocity and weakened electric alignment. It is critical to explore the use of alternative biological media with low electric conductivities. For instance, as we demonstrated previously, in sucrose-based biological media, nanowires have been manipulated effectively in both propulsion and alignment by the applied combined AC and DC *E*-fields, which is compatible with live cell experimentation.[154]

3.4 SPEED MODULATION OF CHEMICAL NANOMOTORS

Next, we exploit the effect of DC *E*-fields on nanomotors. The speed of the Pt-Au chemical nanomotors due to DC *E*-fields are tested in pure water and 5-10 wt% H_2O_2 fuels. Au nanorods of the same dimension are fabricated and tested at the same conditions for control experiments. AC *E*-fields are superimposed to align the nanomotors in their long axis direction when applying DC voltages of -1 to 1 V on 500 µm-gapped microelectrodes. The speed of chemical nanomotors linearly depends on DC *E*-fields and can be controlled to instantly increase, decrease and even reverse directions, depending on the magnitude and direction of DC *E*-fields as shown in Figure 3.9(a). A DC voltage as low as 1 V can lead to a velocity change of ~20 µm/sec of the chemical nanomotors, which is effective in modulating speed of nanomotors for various applications.

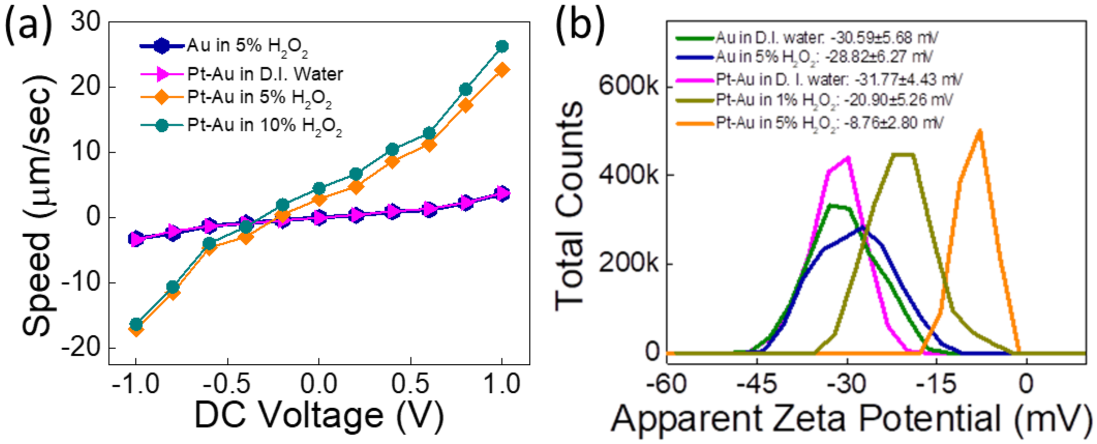

Figure 3.9: (a) Speed of Au nanorods and Pt-Au chemical nanomotors of same dimensions *versus* DC *E*-fields in different suspension mediums. (b) Zeta potentials of Au nanorods and Pt-Au chemical nanomotors in different suspensions. Reproduced with permission.[145] Copyright 2018, American Chemical Society.

We also observe that the speeds of both chemical nanomotors in fuel solutions and those in control experiments always increase in the direction of DC *E*-fields. While the Zeta potentials of both Pt-Au nanomotors and Au nanorods are negative as shown in the measurements in Figure 3.9(b). Furthermore, although the speed of the chemical nanomotors show much stronger responses to the DC *E*-field, the value of their Zeta potential in fuel solutions is significantly lower than those of control samples, *i.e.* for Pt-Au nanomotors in 5% H_2O_2 fuel, the Zeta potential of -8.76 mV is around 1/4 of those of control samples. Sen group has reported a similar decrease of Zeta potential of Pt on Janus spheres in H_2O_2 solution due to catalytic reactions.[155] The reduced Zeta potential of nanomotors can be attributed to the substantial increase of protons on the surface of the nanomotors due to the catalytic reactions in H_2O_2,[156] which reduces the overall negative charges and the absolute value of Zeta potentials of chemical motors.

The above phenomena cannot be explained simply by electrophoresis (EP). Nanoentities, such as nanomotors, experience an electrophoretic force in the presence of an external DC *E*-field due to the formation of an electric double layer at the solid/liquid interface with opposite local charges. The speed of nanoentities ($\boldsymbol{v}_{EP}$) due to electrophoretic force is proportional to the dielectric constant of suspension medium (ε), Zeta potential of nanomotor (ζ), and DC *E*-field (E_{ext}), given by:[157]

$$\boldsymbol{v}_{EP} = \frac{\varepsilon\varepsilon_0\zeta}{\eta}\boldsymbol{E}_{ext} \qquad (3.7)$$

Given that the Zeta potentials of the chemical nanomotors and control samples are all negative, if only because of the electrophoretic effect, the moving speed should increase in the opposite direction of the DC *E*-field and scale with the magnitude of the Zeta potential. However, the experiments show the behaviors of nanomotors opposite to this analysis. The in-depth study shows that in addition to electrophoretic (EO) forces, electroosmosis flows generated on the surface of glass substrates are important as well, which is given by:[157]

$$\boldsymbol{v}_{EO} = -\frac{\varepsilon\varepsilon_0\zeta_s}{\eta}\boldsymbol{E}_{ext} \qquad (3.8)$$

The Zeta potential of glass substrates (ζ_s) is negative and can reach -80 mV.[158] As a result, the direction of electroosmosis flow on glass substrates is in the same direction of DC E-field according to Equation (3.8), opposite to that of the electrophoretic effect on nanomotors in Equation (3.7). Therefore, the speed of a nanomotor ($\boldsymbol{v}_E$) in DC E-field is governed by the combined effects of electrophoretic force on the nanomotor ($\boldsymbol{v}_{EP}$) in Equation (3.7) and electroosmosis flows on the glass substrate ($\boldsymbol{v}_{EO}$) in Equation (3.8). Considering the zeta potentials and the moving direction of nanomotors, it can be found that the electroosmosis flows ($\boldsymbol{v}_{EO}$) dominate the motions of nanomotors. These results and conclusions are consistent with the reported electroosmosis-based micropumps, where the E-fields are generated by catalytic reactions on different materials.[149, 159-160] Therefore, lower absolute values of the negative zeta potential of the nanomotors lead to higher speed modulations by the DC E-field. This well agrees with the experimental results in Figure 3.9(a), where the speed of chemical nanomotors can be strongly tuned by the external DC E-field. The DC modulation effect of the chemical nanomotors in 5 wt% and 10 wt% H_2O_2 solution do not show a significant difference in Figure 3.9(a). This agrees with the understanding that Zeta potential (ζ_p) of nanoparticles increases slowly with the proton concentration with a linear dependence on the logarithm of the proton concentration.[156] In all these experiments, the change of viscous coefficient and dielectric permittivity of suspension due to the presence of H_2O_2 fuels (less than 10 wt%) is minimum, *i.e.* within 3% of that of DI water.[148]

3.5 REVERSIBLE COLLECTION BEHAVIORS OF CHEMICAL NANOMOTORS

Unlike uniform AC electric fields which only generate aligning torques on the nanoentities, non-uniform AC electric fields, interacting with the dipoles induced in the nanoentities, would lead to the emergence of DEP force. Nanoentities that are more polarizable than the water media, in our case, bimetallic nanorods, would be pulled along the gradient into the areas of highest field intensities (positive DEP). The reversible collection behaviors of the nanomotors are realized by relying on the attraction force of the positive DEP effect. To induce the DEP effect, arrays of conductive Au microislands are specially designed on the substrate between a pair of parallel microelectrodes in the microfluidic channels. The original uniform electric field distribution between the parallel microelectrodes is changed by these conductive microislands, and becomes non-uniform and much denser on the edges of these microislands. Therefore, the nanomotors in the microfluidic channels would experience a positive DEP force resulting from the electric field gradient, which drives them toward the regions of highest field intensities, *i.e.* the edges of conductive microislands. The attractive effect can immediately disappear upon the removal of the applied AC electric field.

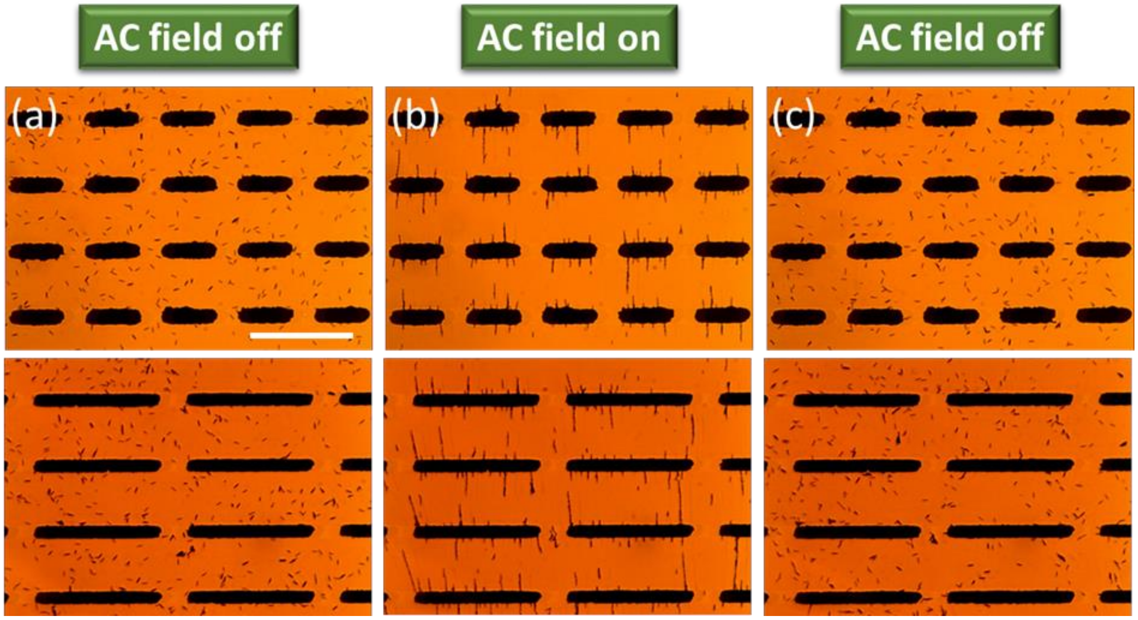

Figure 3.10: Reversible collection and dispersion behaviors of chemical nanomotors. (a) Autonomous motion of nanomotors before AC electric fields are applied. (b) Rapid attraction and assembly of nanomotors when AC electric fields are on. (c) Re-dispersion after turning off AC electric fields. Applied AC field is 50 KHz and 10 Vpp, and the concentration of H_2O_2 is 7.5 wt%. Top: 10 μm×50 μm microislands arrays with 20 μm and 50 μm gaps in X and Y directions, respectively. Bottom: 10 μm×120 μm microislands arrays with 20 μm and 50 μm gaps in X and Y directions, respectively. Scale bar: 100 μm.

Such reversible collection behavior of chemical nanomotors is presented in Figure 3.10. Initially, in the presence of H_2O_2 and absence of the electric field, the chemical nanomotors display their typical autonomous movements as shown in in Figure 3.10(a). The application of the AC electric field rapidly migrates nanomotors toward the conductive microislands and fixes them on the microislands within 10 seconds as shown in Figure 3.10(b). Such collection of nanomotors persists while the electric field is applied. Once the electric field is turned off, the catalytic propulsion dominates again and rapidly disperses nanomotors with autonomous motion as shown in Figure 3.10(c). The self-dispersal process also only takes less than 10 seconds. The frequency of applied AC electric fields is optimized as 50 KHz here to avoid the electroosmotic effect at low frequency, and also to offer a suitable attraction that is sufficiently powerful for effective assembly. Note that if the attraction force is too strong, some of the nanomotors may remain aggregated even after the electric field is turned off. The reversible collection of chemical nanomotors is repeated for 10 cycles and remains functional in our experiments. No physical or chemical principles prevent the operation of this process with more cycles before they run out of the chemical fuel. The demonstration of fully and rapidly reversible collection and dispersion of the nanomotors represents a significant improvement towards various practical applications, such as, replacing fuel medium for nanomotors, and collecting and removing nanomotors after applications.

3.6 APPLICATION I: TARGETED CARGO DELIVERY

With the demonstration and understanding of the prowess of AC and DC *E*-fields for manipulation of chemical nanomotors with high facileness, precision, and efficiency, we exploited two applications of these chemical nanomotors: targeted cargo delivery and assembling of chemical nanomotors for powering rotary NEMS devices.

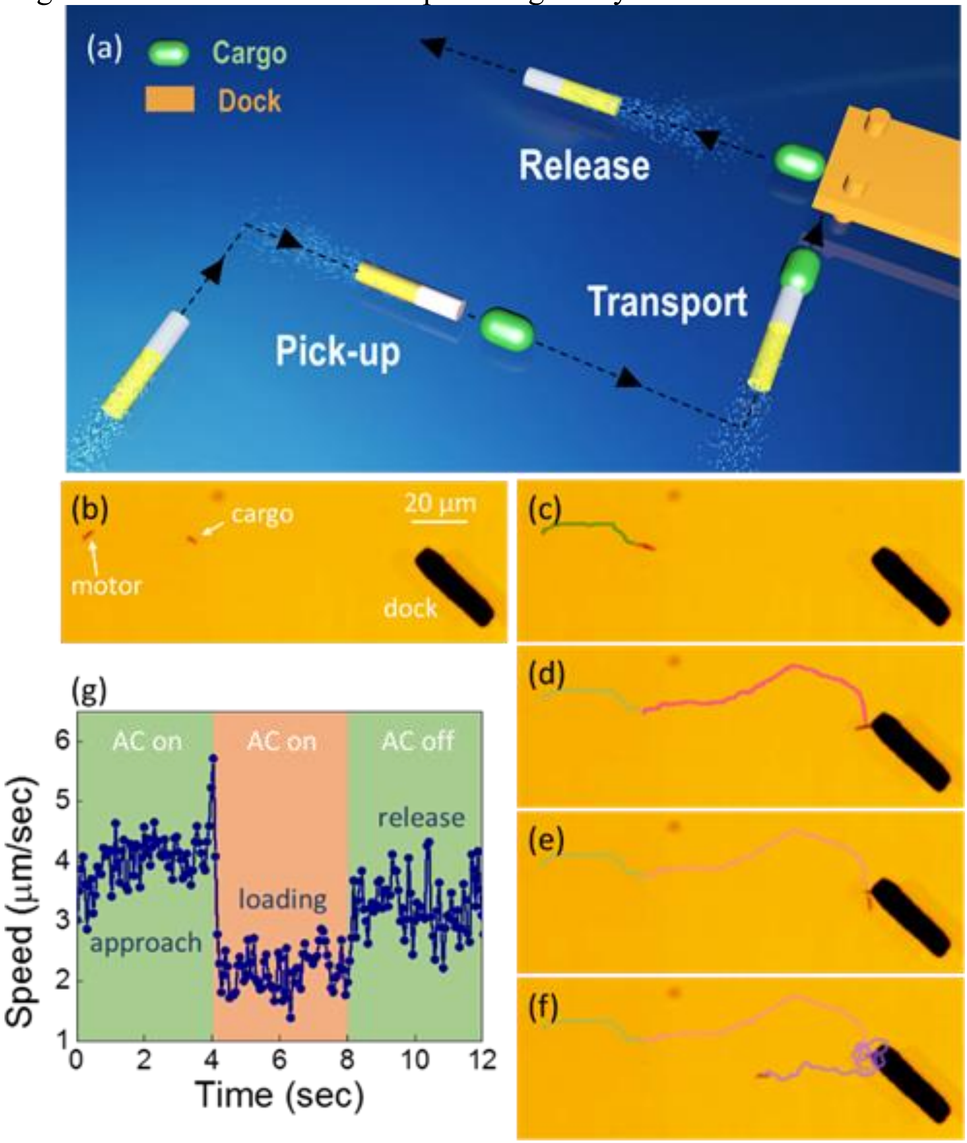
(a)
Cargo
Dock
Release
Transport
Pick-up
(b)
cargo
20 μm
motor
dock
(c)
(d)
(e)
(f)
(g)
AC on
AC on
AC off
release
loading
approach
Speed (μm/sec)
Time (sec)
1
2
3
4
5
6
0
2
4
6
8
10
12

Figure 3.11: (a) Scheme of targeted cargo delivery. (b-f) Optical microscopy images show the dynamic process of a Pt-Au chemical nanomotor when picking up, pushing, and delivering a nanorod cargo to the designated microdock. (g) Speed of the nanomotor in the cargo delivery process. Reproduced with permission.[145] Copyright 2018, American Chemical Society.

In the first demonstration [Figure 3.11(a)], Au nanorods (250 nm in diameter and 3.6 μm in length), fabricated by electrodeposition into nanoporous templates, serve as cargos. They are mixed with Pt-Au chemical nanomotors in 7.5 wt% H_2O_2 fuel solution. Without AC *E*-field, the chemical nanomotors move randomly, while the Au cargos only exhibit weak Brownian motions. By applying a uniform AC *E*-field, both nanomotors and cargo nanorods are aligned. The nanomotors move in the alignment direction. While, the cargo stays essentially at the original location during the transport of the nanomotor guided by the AC *E*-field as shown in Figure 3.11(b-c). When the nanomotor is close to the cargo, the induced *E*-fields can readily assemble them tip to tip. Here, the interaction between the induced dipoles of nanomotor and cargo ensures a simple procedure to upload the cargo on the nanomotor and the assembly is robust during the transport in AC *E*-fields. Next, guided by the AC *E*-field, the nanomotor propels the cargo to a patterned metallic microdock as shown in Figure 3.11(c-d). When the cargo is in the vicinity of the microdock, it can rapidly anchor to the edge of the metallic microdock due to the interaction between induced electric dipoles. Then the nanomotor can start its next journey to seek other targets as shown in Figure 3.11(e-f). Here, the on-demand release of cargos from the chemical nanomotors is facilely accomplished by turning off the AC *E*-field swiftly, *e.g.* for a few seconds [Figure 3.11(e)].

The above process is further determined quantitatively by analyzing the instantaneous speed of nanomotors as shown in Figure 3.11(g). When the nanomotor moves towards the cargo, the average speed is around 3.9 μm/sec. The speed swiftly increases to 5.7 µm/sec when it gets close and attaches to the cargo due to the strong mutual attraction. After capturing the cargo, the speed decreases to 2.2 µm/sec due to the load, which agrees with our estimation of 2.6 µm/sec from Equation (3.5). After releasing the cargo, the nanomotor immediately restores to a speed up to 3.3 µm/sec, which is slightly lower than the speed of 3.6 µm/sec before loading the cargo. Note that at this moment the nanomotor is not aligned by the AC *E*-field which could account for the lowered speed. The above demonstration of targeted cargo delivery by nanomotors under the control of *E*-field shows simplicity and reliability for diverse lab-on-a-chip applications.

3.7 APPLICATION II: ASSEMBLY OF ROTARY NANOMOTORS DRIVEN BY CHEMICAL REACTIONS

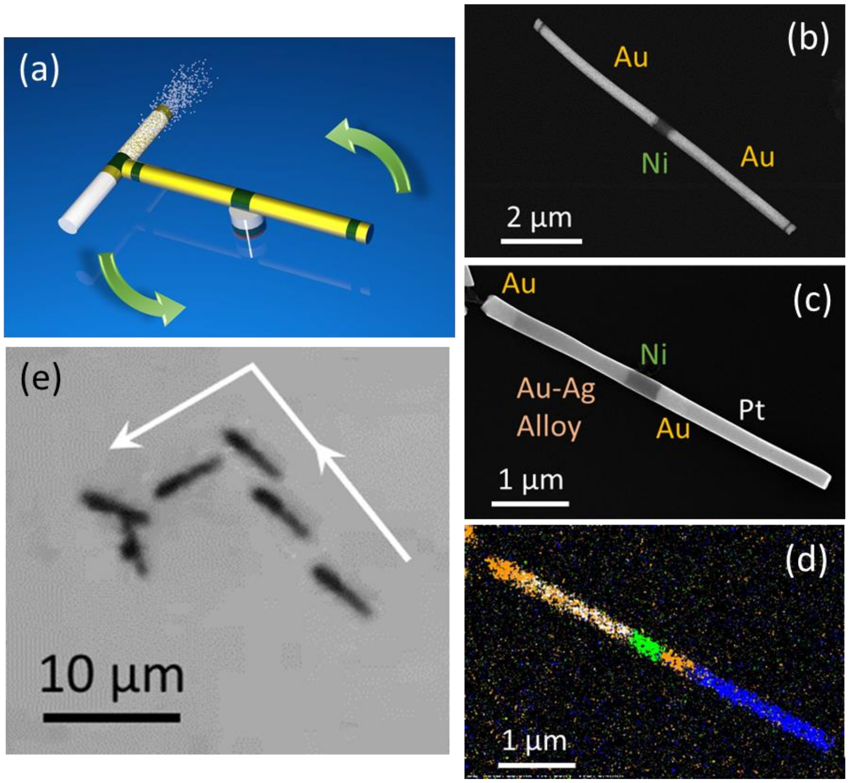

Figure 3.12: (a) Schematic diagram of the rotary NEMS device with chemical nanomotor assembled as the powering component. (b) SEM images of the multi-segment nanowire rotor. The segments from left to right are 200 nm Au, 50 nm Ni, 3.5 μm Au, 500 nm Ni, 3.5 μm Au, 50 nm Ni and 200 nm Au. (c-d) SEM and EDS images of the Pt-Ag/Au chemical nanomotor. The segments from left to right are 400 nm Au, 1.7 μm Ag-Au alloy, 500 nm Ni, 400 nm Au, and 2 μm Pt. (e) Overlapped snapshots showing the assembling process of a chemical nanomotor on a rotary NEMS device. Reproduced with permission.[145] Copyright 2018, American Chemical Society.

Next, leveraging the precision guidance of chemical nanomotors with *E*-fields, we designed and assembled a chemically powered rotary NEMS by integrating chemical nanomotors with electric manipulation. Firstly, a rotary NEMS is assembled by *E*-fields following previous reports as illustrated in Figure 3.12(a).[147, 161] It consists of a multi-segmented Au/Ni nanorod (250 nm in diameter and 8 μm in length) and a patterned nanomagnet (500 nm in diameter) serving as the rotor and bearing, respectively. Different from previous research, the rotor is designed to consist of three Ni segments embedded in the Au nanorod. The structure is Au(200 nm)/Ni(50 nm)/Au(3.5 μm)/Ni(500 nm)/Au(3.5 nm)/Ni(50 nm)/Au(200 nm) as shown in Figure 3.12(b). The Ni segment in the center of the rotor is used to attach the rotary NEMS on the patterned magnetic bearing. The two Ni segments next to the tips aim to anchor the chemical nanomotors. The patterned nanomagnet has a tri-layer stack of Ti (60 nm)/Ni (80 nm)/Cr (6 nm). By using the electric tweezers, the nanorotor is transported and attached atop of the pattern magnetic bearing, where the magnetic interaction between the Ni segment in the rotor and Ni layer in the magnetic bearing fixes the position of the rotary NEMS while still allows its rotation.[147, 161] Next, we fabricated chemical nanomotors made of Pt-AgAu nanowires. Here, we replaced the Au segments used above with Ag(~80 wt%)/Au(~20 wt%) alloy segments in the Pt-based chemical nanomotors [Figure 3.12(c-d)], which can substantially increase the output power and speed. The increase of the speed can be attributed to the much greater potential differences of Pt *versus* AgAu alloy compared to that of Pt *versus* pure Au as reported.[87, 120] The chemical nanomotors move at a speed up to ~30 µm/sec in 5 wt% H_2O_2 solution. From the speed, we can estimate the driving force as high as 0.26 piconewtons (pN). With the guidance of the AC *E*-field, the chemical nanomotor can be efficiently maneuvered towards the rotary NEMS and then be assembled at one end of the rotor by magnetic attraction as shown in Figure 3.12(e). The assembling process was carried out in 1 wt% H_2O_2 solution to ensure we have sufficient responding time to control and assemble.

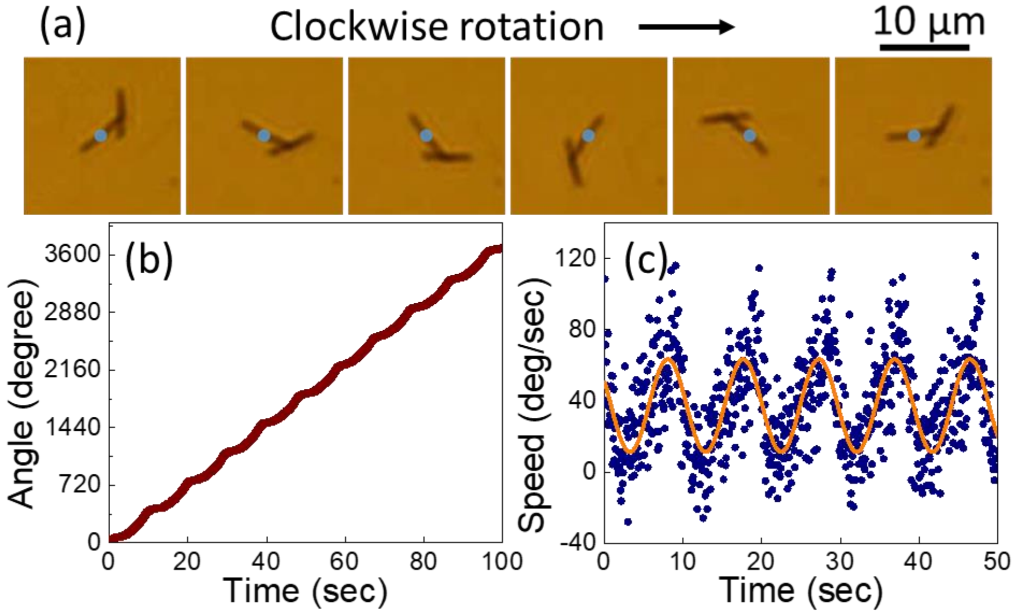

Figure 3.13: (a) Snapshots of a rotating NEMS device driven by a chemical nanomotor taken every 2 seconds. (b) Rotation angle *versus* time of the rotating NEMS device. (c) Rotation speed *versus* time of the rotating NEMS device. Reproduced with permission.[145] Copyright 2018, American Chemical Society.

After assembling, we increased the concentration of the H_2O_2 solution to 5 wt%. The nanomotor instantly propelled the NEMS into continuous rotation as shown in Figure

3.13(a). The driving torque of the nanomotors in Figure 3.13(a) can be readily determined as $1.04 \times 10^{-18} N \cdot m$, which is sufficient to overcome the friction and magnetic torques between the rotor and bearing as shown in Figure 3.13(b-c). Here, we can observe the effects of the angle-dependent magnetic force and torque that result in the oscillation of rotation speeds of the rotor with a 360° periodicity as a function of the angular position, agreeing with previous works.[162] The average rotation speed of the NEMS device is determined as 0.64 rad/sec.

3.8 CONCLUSIONS

In summary, in this chapter we report a highly versatile and precision approach to guide and modulate the propulsions of chemical nanomotors with E-fields, which allows motion control in 2-D and 3-D. The fundamental interactions involved in the electric manipulation have been investigated. Leveraging the precision of manipulation, we experimentally confirmed the inverse linear dependence of speed and size of chemical nanomotors, supporting the previous modeling. For applications, the manipulation strategy provides facile operations of these chemical nanomotors to realize cargo capture, transport, and delivery to designated microdock. The prowess of the manipulation is also demonstrated by assembling chemical motors as powering component of rotary NEMS. This work could be inspiring for constructing various nanorobots and functional NEMS/MEMS devices for diverse tasks in electronics and biomedical research.

Chapter 4: Plasmonic nanomotors for tunable biochemical release and *in-situ* sensing[§]

Controlled release of biomolecules from nanoparticles have received substantial attention from interdisciplinary research communities of chemistry, materials, biology, and engineering.[163-165] The great interest in utilizing nanoparticles as molecule carriers arises due to their molecular and cellular relevant size, which allows precision loading of biochemicals and subsequent release at targeted locations, such as to a single live cell amidst many.[78, 166-168] It is even more potent to actively control the release of biomolecules from nanoparticles. Innovative approaches have been reported to trigger the release of biochemicals from nanoparticles by designed surface functionalization and unique responses of nanoparticles to their environment.[163-165] For instance, the controllable release of molecules by near-infrared light based on the photothermal effect of gold nanocages was recently reported.[169] A similar approach was also used for the intracellular release of oligonucleotides.[170-173] The release of molecules can also be triggered by magnetic fields, which induce mechanical deformation of magnetic hydrogel composites or generate heat due to Néel and Brownian relaxation.[174-175] Controlling electric potential is another method to control the molecule release dynamically based on the electrochemical reduction-oxidation process on the electrode surface.[176] Ultrasound waves have also been reported to trigger the release of molecules through mechanical effects generated by cavitation phenomena or radiation forces.[177-178] Nevertheless, it remains a grand challenge to control the release dynamics of biomolecules in a tunable fashion and monitor the release process *in-situ* and in real time with ultrasensitivity.

[§] Portions of this chapter have been previously published in J. Liu[#], **J. Guo**[#], G. Meng, D. Fan, Chemistry of Materials, DOI: 10.1021/acs.chemmater.8b01979 (2018). J. Guo and J. Liu carried out the research, including experiments and simulation, and wrote the first draft of the manuscript. They contributed equally to this work. Professor G. Meng, J. Liu's supervisor, commented and revised the manuscript. Professor D. Fan conceived this research and supervised the project. She analyzed data and revised the manuscript.

In this chapter, we report a plasmonic nanomotors that not only detects molecules with ultrasensitivity and high reproducibility, but also provides enhanced capacitance to carry biomolecules and actively control their release dynamics. The nanomotor is made of a nanoporous superstructural composite, consisting of an Au nanorod core, a nanoporous superstructural silica shell, and large arrays of plasmonic Ag nanoparticles as shown in Figure 4.1(a-f). The nanoporous silica superstructure with vast embedded nanocavities is strategically created by alternately coating silica and assembling nanospheres on the Au nanorod cores. After calcination, the polystyrene (PS) nanospheres are removed. This process generates high-density nanocavities in silica, arranged concentrically in 3D around the Au nanorod. The nanocavities provide enhanced 3D nanospaces for sustaining biomolecules, as well as large surface areas for the growth of the plasmonic Ag nanoparticles. A three-fold enhancement of molecule loading is achieved compared to that of a solid control sample. The large number of Ag nanoparticles grown on both the inner nanocavities and outer surface of the silica shell [Scheme 1(f-g)], offers substantially enhanced Raman sensitivity, owing to the increased number of hotspots and their near-field electromagnetic coupling. In an external AC electric field, the Ag nanoparticles also actively manipulate molecules and tune the release rate due to the induced electrokinetic effect. Finally, the dual functional superstructural plasmonic nanomotors are manipulated, *i.e.* transported to a specific location and rotated at a controlled speed, making them desirable for location-predicable sensing and biomolecule delivery for many potential applications in precision medicine,[2, 168] mechano-biology,[179-180] cell-cell communications,[181] and system biology.[182-183]

4.1 INTRODUCTION OF SURFACE-ENHANCED RAMAN SPECTROSCOPY (SERS)

Surface-enhanced Raman scattering/spectroscopy (SERS) is one of the most promising sensing techniques that can reveal both the chemistry and quantity of multiplex molecules in a non-invasive, sensitive, and label-free manner.[89, 184-188] The coherent oscillation of electrons in the conduction band of metallic nanoparticles boosts the electromagnetic fields (E) in the vicinity of nanoparticles and their narrow junctions. The locations with ultrahigh electromagnetic field are the so-called plasmonic hotspots. When molecules reside at the hotspots, their Raman spectra are greatly enhanced, with an approximately E^4 dependence.[189-191] It has been of great interest to design and fabricate high-performance SERS substrates. To date, a variety of noble metallic substrates have been fabricated for SERS detection, including nanoparticles,[192-196] nanorods,[197-200] core-shell nanostructures,[201-202] and highly symmetric nanostars.[203-204] Well reproducible plasmonic nanomotors with an enhancement factor as high as 10^9-10^{11} have been reported.[205-206] Nevertheless, current research efforts largely focus on improving the sensing performance of plasmonic nanomotors in terms of enhancement factors and reproducibility. To fully realize the potential of SERS techniques, it has triggered substantial interest to investigate new device paradigm of Raman sensing devices that provide multiple integrated functions.[90, 207-210] Particularly, a dual-functional device scheme that offers Raman sensing capability integrated with active manipulation of molecules is challenging, while of great potential for many applications.[95, 211]

4.2 DESIGN AND FABRICATION OF PLASMONIC NANOMOTORS

The design of each component in the porous superstructural plasmonic nanomotor serves for a purpose. The long metallic core can be readily polarized and manipulated in external electric fields. The nanoporous silica shell supports the growth of a large number of plasmonic Ag nanoparticles with 3D arrangement, separating them from the metallic core to avoid plasmonic quenching, and effectively increasing the plasmonic couplings of the Ag nanoparticles in 3D. The nanoporous silica superstructure also provides large specific surface areas for the loading of molecules. The high-density Ag nanoparticles not only substantially increase the enhancement factor of SERS, but also generate strong electrokinetic effects for tuning the release rate of molecules.

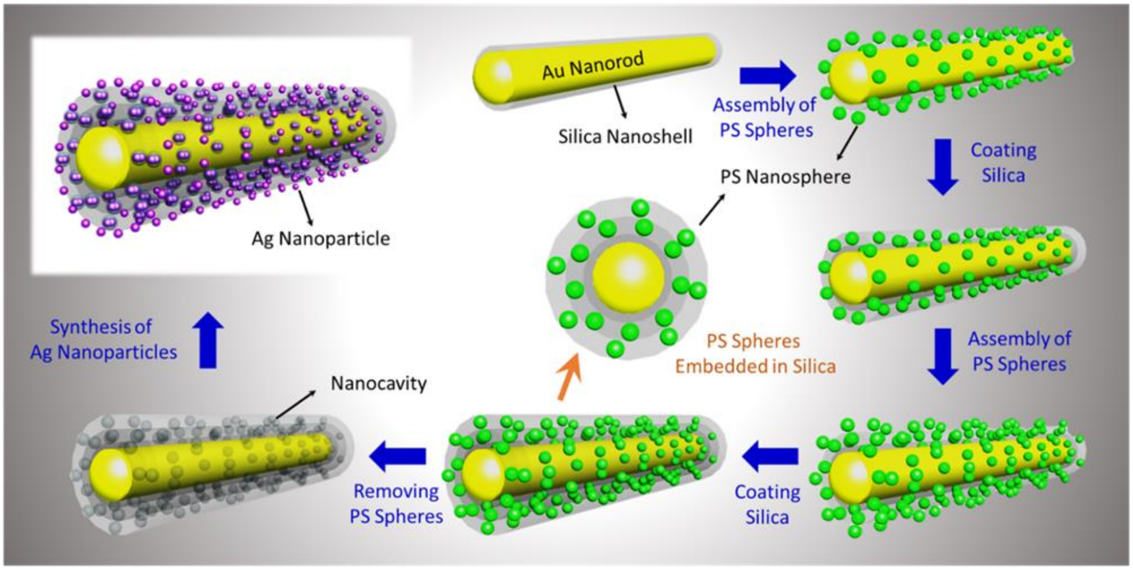
Ag Nanoparticle
Au Nanorod
Silica Nanoshell
Assembly of PS Spheres
PS Nanosphere
Coating Silica
PS Spheres Embedded in Silica
Assembly of PS Spheres
Synthesis of Ag Nanoparticles
Nanocavity
Removing PS Spheres
Coating Silica

Figure 4.1: Flowchart of the fabrication process of the nanoporous superstructural plasmonic nanomotors. Reproduced with permission. Copyright 2018, American Chemical Society.

The fabrication of the superstructural plasmonic nanomotors starts with the growth of Au nanorods of ~ 5 µm in length and ~ 280 nm in diameter by electrodeposition into nanoporous anodic aluminum oxide (AAO) templates as shown in Figure 4.1.[7, 212] Then, a uniform thin layer of silica is conformally coated on the surface of the Au nanorods *via* hydrolysis of tetraethyl orthosilicate (TEOS) in ammonia solution [Figure 4.2(a)]. A suspension of Au nanorods (~10^8/mL, 1 mL) is mixed with a solution made of 3 mL ethanol, 0.8 mL D.I. water, 100-200 μL ammonia (30 wt%) and 400-800 μL TEOS, and subjected to sonication for one hour at room temperature. To obtain high porosity and a large surface-to-volume ratio, the thickness of the first silica nanoshell is optimized to 20-30 nm. This thickness guarantees a uniform and well reproducible coating.

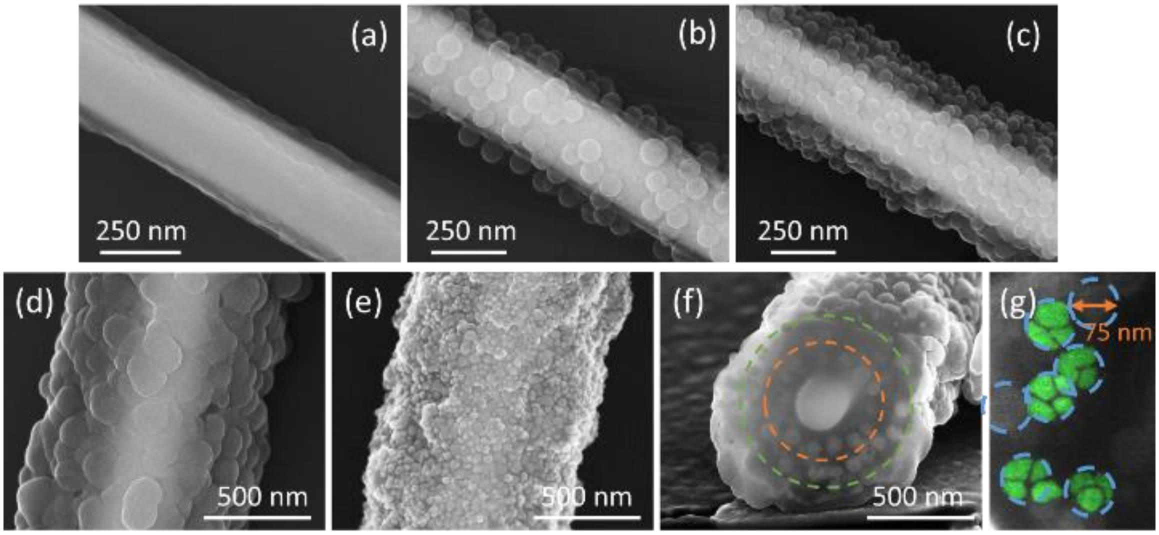

Figure 4.2: SEM images of (a) Au nanorod with a silica nanoshell. (b) Assembling of the first layer of PS nanospheres on the Au/silica core-shell nanostructure. (c) Assembling of the second layer of PS nanospheres on the Au/silica core-shell nanostructure. (d) 3D nanoporous superstructure with large arrays embedded nanocavities. (e) Ag-nanoparticles on the outer surface of the superstructure. (f) Cross-sectional view of the superstructure with Ag nanoparticles in the embedded nanocavities arranged in two concentric nanorings. (g) Close-up view of a few nanocavities with filled Ag nanoparticles (in pseudocolor) of narrow junctions of a few nanometers. Reproduced with permission. Copyright 2018, American Chemical Society.

To generate 3D nanocavities in the silica shell, we assemble large arrays of PS nanospheres on the surface of the silica. Firstly, we modify the outmost surface of the silica layer in the Au/silica core-shells with positively charged molecules by functionalizing polyelectrolytes of poly(diallyl-dimethyl-ammonium chloride) (PDDA, positively charged) and poly(sodium-p-styrene sulfonate) (PSS, negatively charged), alternatively.

Next, the core-shell nanostructures are dispersed in a PS nanosphere suspension. These negatively charged nanospheres can swiftly assemble on the positively-charged outer surfaces of silica with a high density and individual separations due to electrostatic interactions [Figure 4.2(b)]. The diameter of the PS nanospheres is controlled to be 70-80 nm and the density is ~ $95/\mu m^2$. Then, by repeating the process of silica coating and nanosphere assembling, multiple layers of nanospheres can be rationally embedded in the silica forming into a 3D superstructure. As shown in Figure 4.2(c), the second layer of PS nanospheres with a density of ~ $103/\mu m^2$ is successfully assembled on the outer surface of the silica shell, which has the first impregnated layer of nanospheres in Figure 4.2(b). To fully cover the PS nanospheres assembled on the Au/silica core-shells, the thickness of the silica nanoshells is increased to 40-50 nm. After coating the outmost layer of silica, the PS nanospheres are removed at 550 ˚C in the air, forming nanoporous superstructures with mono-dispersed nanocavities [Figure 4.2(d)]. The final diameter of the porous silica superstructures is around 850 nm.

The corrugated surface due to the embedment of nanocavities could enhance the loading of plasmonic Ag nanoparticles [Figure 4.2(d)]. Finally, the Ag nanoparticles are grown both in the inner nanocavities and on the outer surfaces of the porous silica superstructures by catalytic reduction of silver nitrate ($AgNO_3$) [Figure 4.2(e-g)]. Firstly, the nanoporous superstructures are incubated and stirred in a mixture of $AgNO_3$ (0.06 M, 500 μL) and ammonia (0.12 M, 250 μL) for sufficient adsorption of Ag ions. Then polyvinylpyrrolidone (PVP, 10 mL of 2.5×10^{-5} M in ethanol) is added to promote the reduction of $AgNO_3$ and growth of Ag nanoparticles at 70 ℃. After 7-hour reaction, dense Ag nanoparticles are grown on both the outer surfaces and inner cavities of the nanoporous superstructures. Characterization with ImageJ (software) shows that the average size of Ag nanoparticles and nanojunctions between them on the outmost surface of the nanoporous superstructural plasmonic nanomotors are 27.38±6.73 nm and 2.51±1.01 nm, respectively. The histograms are shown in Figure 4.3. We know that electromagnetic fields increase dramatically with the narrowing of the junctions of Ag nanoparticles. If we only consider the nanojunctions of <2 nm as hotspots for significantly enhancing Raman signals of molecules, the density of hotspots is estimated as ~800 /μm^2 on the outer surfaces of the nano superstructures. Since the reaction occurs in aqueous solutions, the reactant ions can readily diffuse and react inside the nanocavities, resulting in the growth of Ag nanoparticles on the inner surfaces of nanocavities.

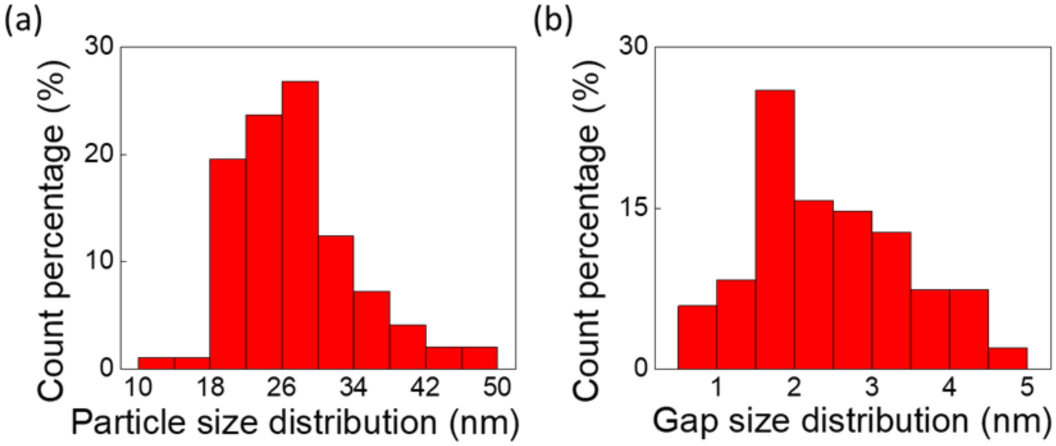

Figure 4.3: Size distribution of (a) Ag nanoparticles and (b) nanojunctions between them. Reproduced with permission. Copyright 2018, American Chemical Society.

The Ag nanoparticles embedded in the nanocavities are characterized by milling and exposing the cross-section of the superstructures with Focused Ion Beam (FIB). The cross-sectional image of the nano superstructure in Figure 4.2(f) reveals two concentric rings, around the Au nanorod core, made of nanocavities filled with Ag nanoparticles. The high-magnification image in Figure 4.2(g) shows that each nanocavity is filled with three to four Ag nanoparticles with ultra-narrow junctions of a few nanometers. We assumed there are 4 Ag nanoparticles in each nanocavity, positioned at tetrahedral sites. Then, 6 hotspots can be contributed by each nanocavity. In another word, the density of the hotspots in the two concentric layers of nanocavities are 570 and 618 hotspots/μm^2 respectively. These embedded Ag nanoparticles provide an additional ~80% hotspots of those on the outer surface.

4.3 LOADING CAPACITY OF BIOMOLECULES ON PLASMONIC NANOMOTORS

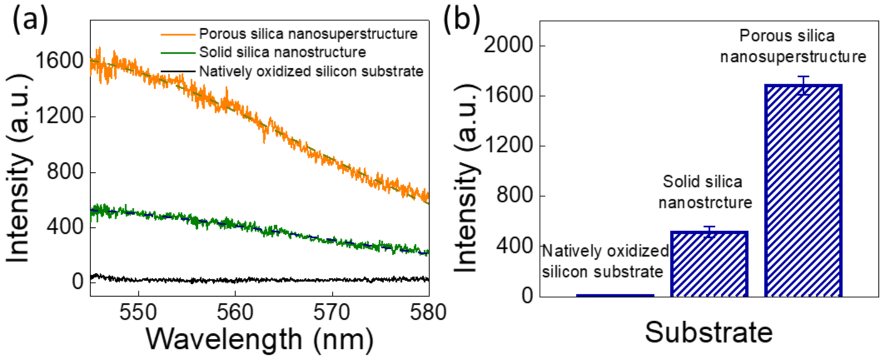

Figure 4.4: (a) Fluorescence spectra and (b) average fluorescent intensity of R-6G molecules obtained from the porous Au/silica nano superstructures, solid control samples and natively oxidized silicon substrate. Reproduced with permission. Copyright 2018, American Chemical Society.

Owing to the embedded nanocavities in the unique superstructures, the loading capacitance of molecules on the superstructural plasmonic nanomotors is enhanced by more than 3 times compared to that of solid samples. To determine the enhancement of loading in the nanoporous structures quantitatively, we employed Rhodamine 6G (R-6G) as a fluorescence probe. To avoid plasmonic enhancement effects, the tests are carried out before the growth of Ag nanoparticles. Nanostructures consisting of Au nanorod cores and silica shells of the same thickness without nanocavities (Au nanorod: ~280 nm in diameter, silica shell: ~285 nm) are fabricated as control samples. The nanostructures are incubated in 10^{-5} M R-6G aqueous solutions for 2 hours before testing. After rinsing in DI water, they are dispersed and dried on glass substrates. Measurements of fluorescent intensity are taken by using a 532-nm laser with a spot size of 6 μm and power of 0.5 μW. The exposure time for each test is 5 seconds. As shown in Figure 4.4, the fluorescent measurement of R-6G molecules loaded on the porous nano superstructure is approximately 3.3 times that of the control samples. It could be attributed to the excess surface areas provided by the embedded nanocavities in the superstructures.

The experimentally obtained enhancement of 3.3 is comparable to that obtained from calculations of ~2.5. The slightly higher value obtained from experiments can be largely attributed to the greater retention of R-6G molecules by the embedded nanocavities than that of the outer surfaces. We notice that the surface areas of the silica superstructures can be further increased by integrating more layers of nanocavities by cycling the nanosphere-assembling-silica-coating process. Indeed, this unique strategy opens a rational way in creating nanoporous superstructures with controlled arrangement of nanocavities in 3D, which offers much enhanced specific surface areas and loading capacity of molecules.

4.4 CHARACTERIZATION AND SIMULATION OF SERS

Furthermore, the Ag nanoparticles grown on the outer surface and inner nanocavities provide substantially enhanced Raman sensitivity for biochemical detection. Raman signals of probing molecules R-6G ranging from 10^{-11} M to 10^{-15} M can be detected as shown in Figure 4.5(a). A 532-nm laser with a spot size of 6 μm and power of 50 μW is used for SERS measurements. The exposure time for each test is 5 seconds. The sensing limit is as low as 10^{-15} M with a signal-to-noise ratio of 3.97 at 608 cm^{-1} and 3.67 at 771 cm^{-1}, respectively, which is at least one order of magnitude improvement of that obtained from the control samples made of Ag-coated solid Au/silica nanorods [Figure 4.5]. The porous plasmonic nanomotors also detect the non-resonant probing molecules 1,2-bis(4-pyridyl) ethylene (BPE) at an ultralow concentration of 10^{-13} M with a signal-to-noise ratio of 6.12 at the characteristic peak of 1198 cm^{-1} as shown in Figure 4.6. The enhancement factor (EF) is determined as 3.78×10^{9} by following a widely-used method,[89, 213-214] which is more than two-time higher than that of the solid plasmonic nanomotors (1.75×10^{9}).

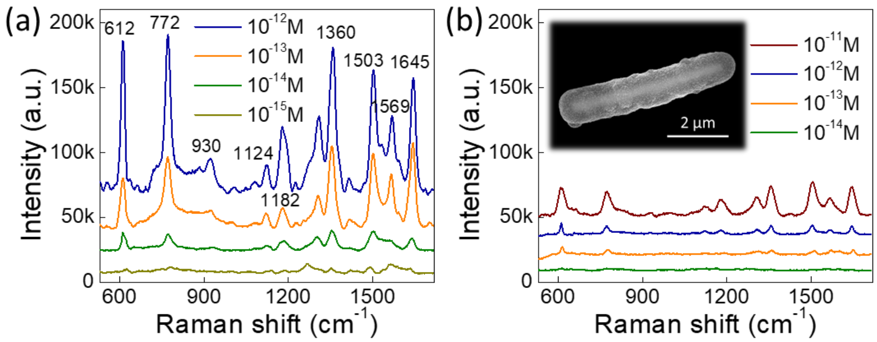

Figure 4.5: SERS spectra of R-6G molecules of different concentrations determined from the porous superstructural plasmonic nanomotors (a) and the control samples made of solid plasmonic nanomotors (b). Inset in (bb): SEM image of the control samples. Reproduced with permission. Copyright 2018, American Chemical Society.

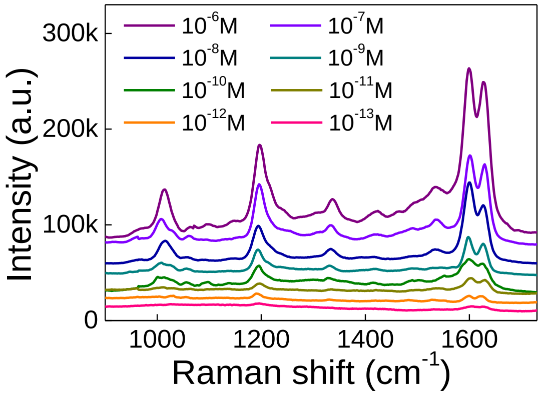

Figure 4.6: SERS spectra of BPE molecules with different concentrations detected from the porous plasmonic nanomotors. Reproduced with permission. Copyright 2018, American Chemical Society.

Herein the enhancement factor (EF) of plasmonic nanomotor can be calculated by:

$$EF = \frac{I_{SERS}/N_{SERS}}{I_{RS}/N_{RS}} \qquad (4.1)$$

where I_{SERS} and I_{RS} correspond to the Raman intensity at 1200 cm^{-1} of BPE molecules obtained from a SERS substrate and directly from a suspension, respectively. N_{SERS} and N_{RS} are the number of molecules detected from the SERS substrate and suspension without a SERS substrate, respectively.

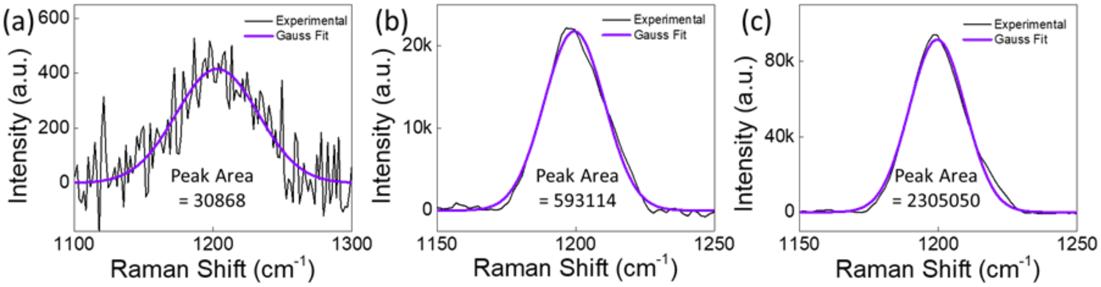

Figure 4.7: (a) Raman spectrum of 1 M BPE in ethanol solution (integration time 10 seconds). SERS spectra on (b) solid and (c) porous plasmonic nanomotors with saturated adsorption of BPE, respectively (integration time 5 seconds). Reproduced with permission. Copyright 2018, American Chemical Society.

The value of I_{RS} is obtained from 1 M BPE ethanol solution excited by a 532-nm laser at 50 µW (integration time 10 seconds). As shown in the Raman spectrum in Figure 4.7(a), I_{RS}=3087 counts/second were achieved.

N_{RS} is given by $N_{RS}=V_{scat}\cdot C_{BPE}\cdot N_A$, where V_{scat} is the volume of BPE that contributes to the Raman signals, C_{BPE} is the concentration of BPE solution (1 M), N_A is Avogadro's number. V_{scat} is determined by $V_{scat}=A_{obj}\cdot H_{obj}$, where A_{obj} is the size of the laser spot, H_{obj} is the effective height of the detection volume of BPE. The diameter of the laser from a 20× objective is 6 µm, thus $A_{obj}=\pi R^2=28.26\ \mu m^2$. By using the method reported previously,[89] $H_{obj}=56.6\ \mu m$ was obtained. Therefore,

$N_{RS}= A_{obj}\cdot H_{obj}\cdot C_{BPE}\cdot N_A$=28.26 µm^2×56.6 µm×1 mol/L×6.02×10^{23}=9.63×10^{11} molecules

To determine the value of I_{SERS} for both the solid and porous plasmonic nanomotors, we immersed the nanostructures in 1 mM BPE ethanol solution for 2 hours and rinsed by pure ethanol. Figure 4.7(b-c) shows the obtained SERS spectra with a 532-nm incident laser. We can see that I_{SERS} for the solid and porous plasmonic nanomotors are 118623 counts/second and 461010 counts/second, respectively.

The value of N_{SERS} is estimated by counting the number of BPE molecules existing in the hot spots which make the major contribution to the obtained SERS intensity. Since the laser spot is larger than the length of the plasmonic nanomotors (5 μm), the effective exposure area on the outer surface of the plasmonic nanomotors is estimated as 1/3(effective factor due to curvature) ×850 nm (diameter)×5 μm (length)=1.42 μm^2. Similarly, the effective exposure areas for the inner nanocavities, where the two concentric layers of PS nanospheres locate at, are estimated as 0.53 μm^2 and 0.97 μm^2, respectively. Therefore, the number of effective hotspots contributed by the outer surface and inner nanocavities are 1.42 $\mu m^2 \times 793/\mu m^2=1126$ hotspots, and 0.53 $\mu m^2 \times 570/\mu m^2$ +0.97 $\mu m^2 \times 618/\mu m^2=902$ hotspots, respectively. Moreover, we can assume the volume of hotspot is ~3.375 nm^3, which is the average gap size as aforediscussed to the power of three. The volume of BPE molecule is 3 Å × 6 Å × 10 Å/molecule=180 $Å^3$/molecule.

Therefore, for solid plasmonic nanomotors:

$$N_{SERS} = 1126 \text{ hotspots} \times 3.375 \text{ nm}^3/(180 \text{ Å}^3/\text{molecule}) = 21113 \text{ molecules}$$

$$EF_{soild\_sensor} = \frac{I_{SERS}/N_{SERS}}{I_{RS}/N_{RS}} = \frac{118623/21113}{3087/(9.63\times10^{11})} = 1.75\times10^{9}$$

For the porous superstructural plasmonic nanomotors:

$$N_{SERS} = (1126+902) \text{ hotspots} \times 3.375 \text{ nm}^3/(180 \text{ Å}^3/\text{molecule}) = 38025 \text{ molecules}$$

$$EF_{porous\_sensor} = \frac{I_{SERS}/N_{SERS}}{I_{RS}/N_{RS}} = \frac{461010/38025}{3087/(9.63\times10^{11})} = 3.78\times10^{9}$$

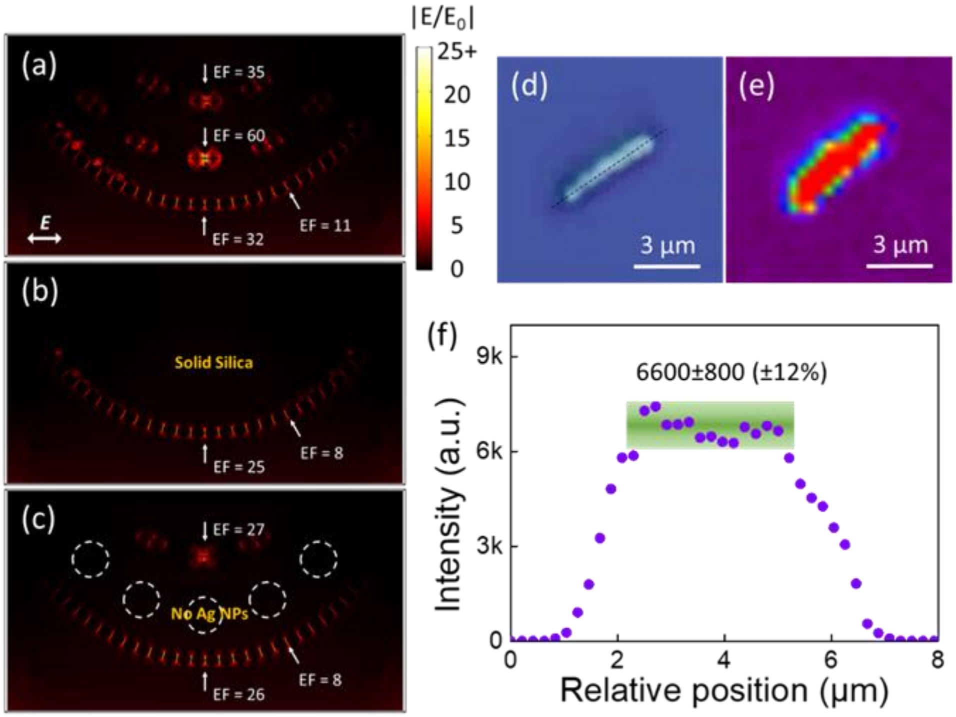

Figure 4.8: (a-c) Simulations of the electric field distribution in (a) a nanoporous superstructural plasmonic nanomotor, (b) a solid plasmonic nanomotor, and (c) a porous superstructural plasmonic nanomotor without Ag nanoparticles in the second layer of embedded nanocavities. The 532-nm laser is in the vertical direction with an in-plane polarization. (d) Optical image of a porous plasmonic nanomotor and (e) Raman mapping of R-6G (10^{-6} M, 1644 cm^{-1}). (f) Intensity of Raman signals along the length of the porous plasmonic nanomotor in (d). Reproduced with permission. Copyright 2018, American Chemical Society.

Note that an EF of 10^8 is sufficient for detecting a variety of biochemicals on the single molecular level.[89, 191, 205, 215] The improved Raman sensitivity of the porous plasmonic nanomotors can be attributed to at least two factors as discussed in the following. As aforediscussed, the plasmonic Ag nanoparticles in the embedded nanocavities of the porous plasmonic nanomotors provide a much greater number of hotspots for detecting molecules at ultralow concentration compared to that of the solid samples. Moreover, the strategical arrangements of the hotspots in different concentric layers of nanocavities offer additional enhancement due to the plasmonic near-field effect.

This is determined by the numerical simulation with COMSOL in Figure 4.8(a-c), where a porous superstructural plasmonic nanomotor is modeled as a coaxial cylinder (Au nanorod: 280 nm in diameter) with embedded layers of spherical nanocavities (80 nm in diameter). The Ag nanoparticles are modeled as 30 nm spheres with junctions of 2 nm. The entire porous plasmonic nanomotor is placed on a glass substrate and excited with an in-plane polarized 532-nm laser. Numerical calculations of the electric fields in the porous plasmonic nanomotors [Figure 4.8(a)] and solid plasmonic nanomotors [Figure 4.8(b)] indicate that the Ag nanoparticles inside the embedded nanocavities not only provide more hotspots with higher volumetric electric field intensity but also effectively increase the electric field intensity at the junctions of Ag nanoparticles on both the outer surfaces and inner layers of cavities. For instance, the numerically calculated electric field is enhanced from 25/26 to as high as 32 on the outer surface, and from 27 to as high as 35 on the inner cavities. It is due to the so-called near-field effect, resulting from the induced resonance coupling of plasmonic nanoparticles.[90, 216] Both of these factors contribute to the high sensitivity achieved from the porous superstructural plasmonic nanomotors.

Not only sensitive, the porous plasmonic nanomotors offer fairly uniform Raman enhancement along the length as shown by the SERS mapping in Figure 4.8(d-f). Signals along the dashed line on the plasmonic nanomotor have a variation within ±12% [Figure 4.8(f)], which is fairly low given the high local-electric-field dependence of SERS. It can be attributed to the uniformly distributed Ag nanoparticles on the porous plasmonic nanomotors as shown in Figure 4.2(e).

4.5 TUNABLE BIOCHEMICAL RELEASE FROM PLASMONIC NANOMOTORS

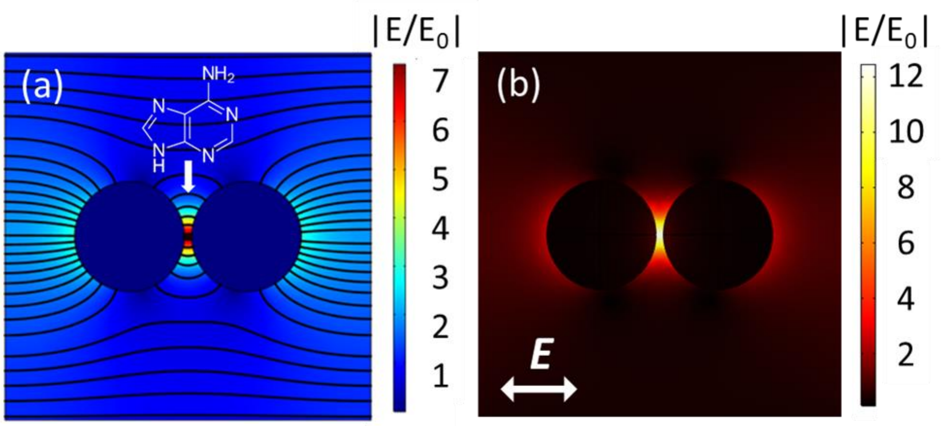

Figure 4.9: Finite Element Modeling with COMSOL: (a) electric field distribution around a pair of Ag nanoparticles and attraction of molecules towards the location with the highest electric field. (b) The distribution of electromagnetic field due to an incidental laser around a pair of Ag nanoparticles. The laser is in the vertical direction with an in-plane polarization. Reproduced with permission. Copyright 2018, American Chemical Society.

Next, by exploiting both the metallic and plasmonic properties of the Ag nanoparticles grown on the porous plasmonic nanomotors, we actively controlled the release of biomolecules at tunable rates by external electric fields and detected the release kinetics in quasi-real-time by Raman spectroscopy. As shown in the simulation in Figure 4.9(a), in a uniformly applied external electric field, the electric field around a pair of metallic Ag nanoparticles is focused at the junction of the metal dimer due to the polarization of Ag nanoparticles, co-localized at the position of the plasmonic sensing hotspot [Figure 4.9(b)]. This induced non-uniform electric field can readily exert an induced DEP force on the molecules in the vicinity of Ag nanoparticles and in suspension. When the electric polarization of the molecules is stronger than that of the suspension medium, the molecules can be facilely attracted and retained at the position of the highest electric field, co-localized with the hotspots as shown in Figure 4.9(a-b). This effect is due to the so-called positive DEP, which depends on AC frequency and dielectric permittivity of both molecules and suspension medium. Therefore, under optimized conditions, the plasmonic Ag nanoparticles can be dually functional, working as molecular tweezers that actively manipulate the release rate of molecules and Raman nanosensors that detect the instantaneous release.

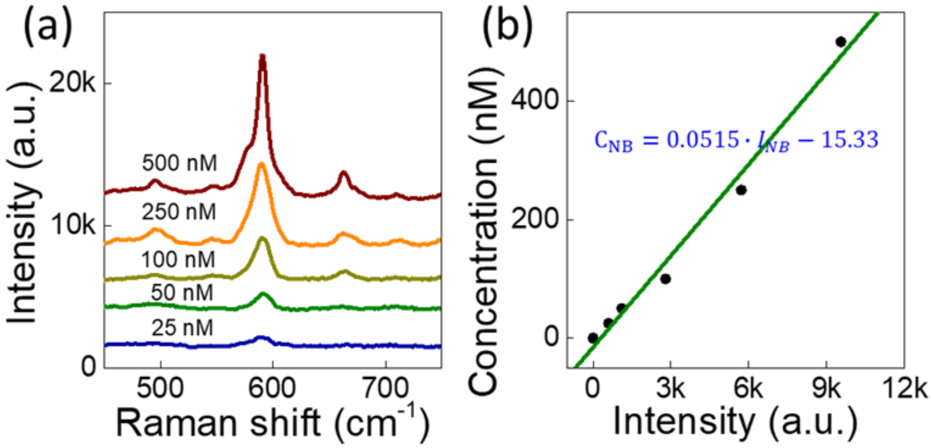

Figure 4.10: (a) Raman intensities of Nile Blue (595 cm^{-1}) at different concentrations detected from the plasmonic nanomotors. (b) The linear dependence of Raman intensity on concentrations of Nile Blue from 25 nM to 500 nM. Reproduced with permission. Copyright 2018, American Chemical Society.

With the above analysis and understanding, we carried out a series of experiments by using Nile Blue (NB) molecules to study the tuning of biomolecule release with an external electric field. NB is a typical SERS probing molecule and has a higher molecular polarizability (~800×10^{-40} F·m^2) than that of water (1.61×10^{-40} F·m^2).[217-218] According to the Fick's diffusion laws, when molecules are released from a substrate to the bulk solution, the time-dependent concentration of molecules on the substrate (C) can be calculated as:[219]

$$C = C'e^{-kt} + C_0 \qquad (4.2)$$

where $C' = C_s - C_0$, C_s is the initial concentration of the molecules adsorbed on the substrate, C_0 is the initial concentration of the molecule in the bulk solution, and k (s^{-1}) is the molecule release rate. The Raman intensity of NB molecules (at 595 cm^{-1}) adsorbed on the plasmonic nanomotors increases linearly with the concentration of NB ranging from 25 nM to 500 nM (Figure 4.10). Therefore, by fitting the Raman signals *versus* time, the release rate (k) of NB from the plasmonic nanomotors can be obtained according to Equation (4.2).

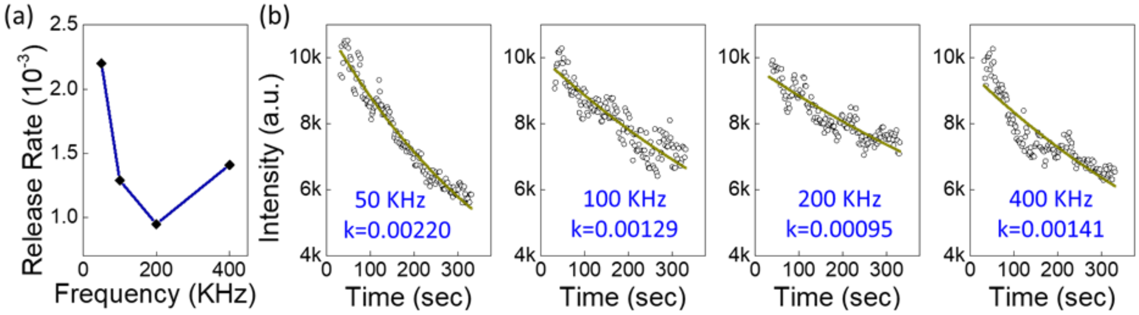

Figure 4.11: (a) Release rate of NB from plasmonic nanomotors at different AC frequencies. (b) Raman detection of the release of NB molecules with time in an external electric field of 50V, 50- 400 kHz. Reproduced with permission. Copyright 2018, American Chemical Society.

We found that the optimal AC frequency for controlling the release rate occurs at 200 KHz, where the decrease of the release rate compared to that without external electric field is the greatest (Figure 4.11). Next, we tested the voltage-dependent release from 0 to 75 V at 200 KHz as shown in Figure 4.12. The strong effect of the electric field in tuning the molecule release rate can be clearly observed, where the release rate (k) monotonically deceases with applied voltage. It can be understood by examining the DEP force applied on molecules due to external electric fields, which depends on both the electric field strength (E) and electric field gradient (∇E). Since both the E and ∇E are the greatest at the vicinity of Ag nanoparticles, the DEP force attracts and retains molecules around the Ag nanoparticles, effectively reducing the release rate. Therefore, by adjusting the applied voltages at optimal AC frequencies, we successfully achieved tunable release rate of molecules from the plasmonic nanomotors.

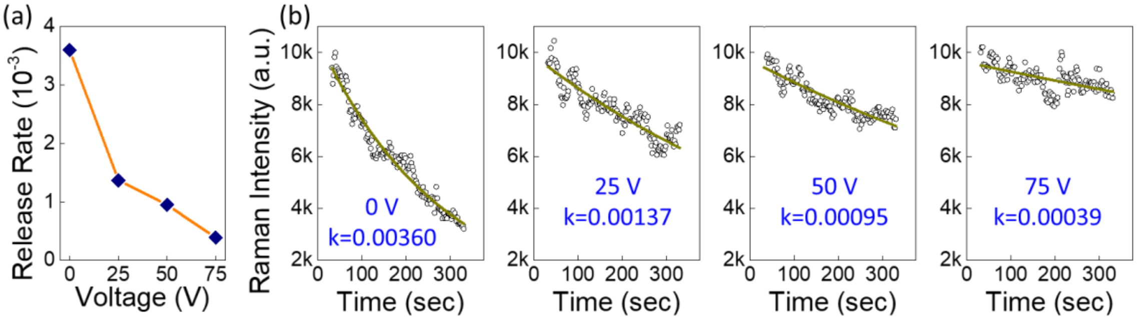

Figure 4.12: (a) Voltage-dependent release rate *versus* applied voltage at 200 kHz and (d) Raman detection of the release of NB molecules with time in an external electric field of 0 to 75 V, 200 kHz. Reproduced with permission. Copyright 2018, American Chemical Society.

The approach is not only feasible for the SERS probing molecules NB. We successfully tuned the release rate of other interesting biomolecules, such as adenine, a basic building block of nucleic acids as shown in Figure 5. The derivatives of adenine, such as adenosine triphosphate (ATP) and cofactors flavin adenine dinucleotide (FAD), are widely present in live beings. As shown in Figure 4.13(a-b), we can detect adenine molecules from the plasmonic nanomotors by Raman spectroscopy, the intensity of which monotonically correlates with the concentration. When turning the AC electric fields on and off, the release rate of adenine can instantly decrease and restore, respectively, monitored in quasi-real time as shown in Figure 4.13(c).

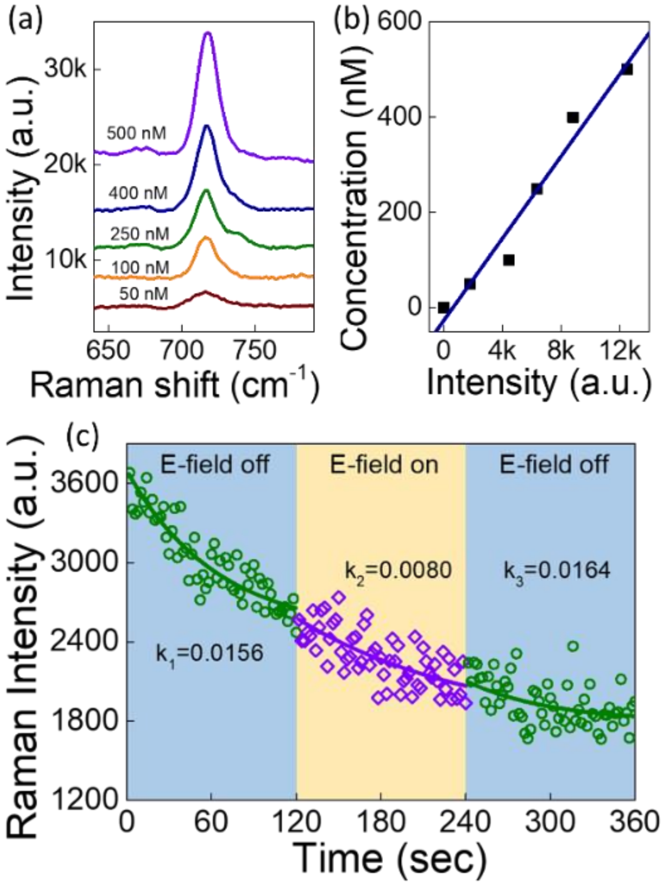

Figure 4.13: (a) Intensity of Raman spectra of adenine at 720 cm^{-1} at different concentrations detected from the plasmonic nanomotors. (b) Raman intensity of adenine is linearly proportional to concentration from 0 to 500 nM. (c) Raman detection of release of adenine molecules *versus* time when an AC electric field of 500KHz 50V is turned on and off. Reproduced with permission. Copyright 2018, American Chemical Society.

4.6 MANIPULATIONS OF PLASMONIC NANOMOTORS

Finally, the plasmonic nanomotors can be efficiently motorized by the electric tweezers.[220] Precise delivery and controllable release of biochemicals with sub-cellular resolution is highly desirable in the study of cell-to-cell communication, single-cell biology, and biomedical toxicology research.[78, 221-222] Robotization of the nanosensor demonstrated here would allow the biomolecule delivery and detection at predetermined location, *e.g.*, a single live cell amidst many.

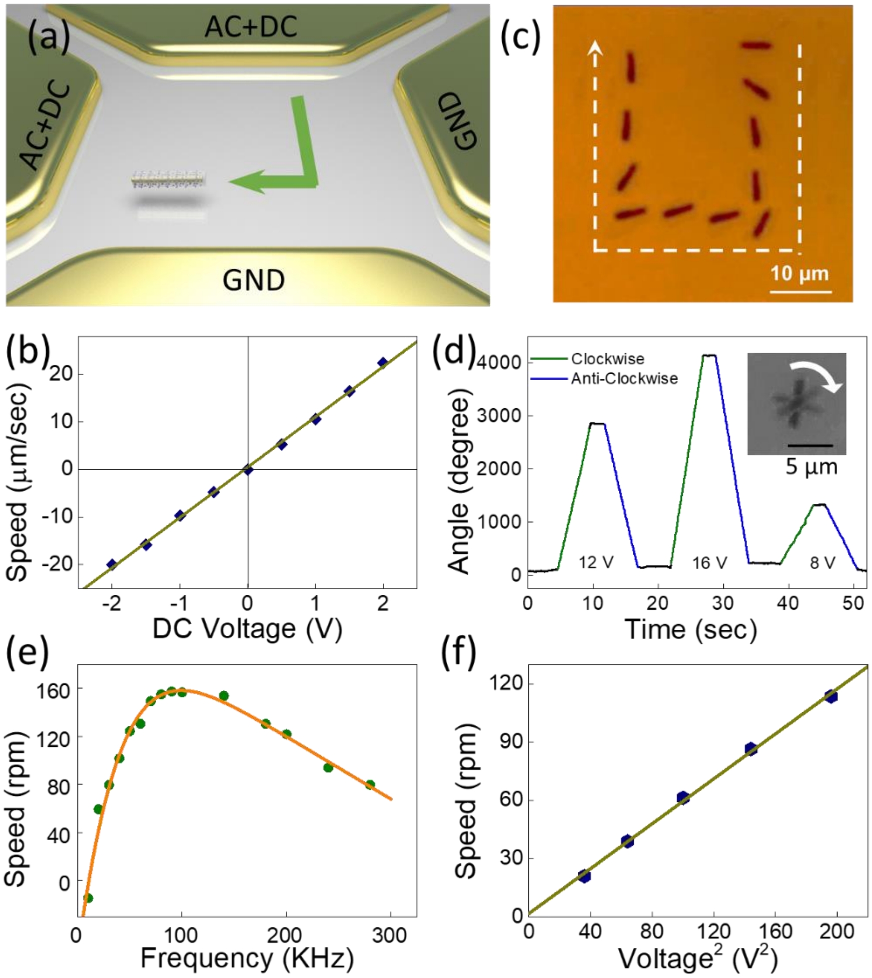

Figure 4.14: (a) Schematic of a plasmonic nanomotor manipulated by the electric tweezers. (b) Transport speed of a plasmonic nanomotor *versus* applied DC voltage. (c) Overlapped snapshots of a plasmonic nanomotor transported along the letter "U". (d) Rotation angle profile at different AC electric field voltages (50 KHz), inset: overlapped snapshots. (e) Rotation speed *versus* frequencies of AC electric fields (14V). (f) Rotation speed *versus* the square of applied voltages (50 KHz). Reproduced with permission. Copyright 2018, American Chemical Society.

As shown in Figure 4.14(a), in a combined AC and DC electric field, a plasmonic nanomotor can be transported along both the X and Y directions. The transport speed of the plasmonic nanomotors linearly increases with the applied DC voltage as shown in Figure 4.14(b) and the alignment is controlled by the AC electric field. The transport can be attributed to electrophoresis (EP) effects as well as the electroosmosis (EO) flows.[8, 145] The alignment is due to the interaction between the induced dipole moment of the longitudinal nanomotor and the AC electric field.[7, 223] By applying combined AC and DC electric fields in both the X and Y directions with controlled duration, the plasmonic nanomotor can go along a designed path, such as a letter "U", as shown in Figure 4.14(c). Further studies also demonstrated the controlled rotation of the plasmonic nanomotors, as shown in the rotation angle profile and the overlapped images in Figure 4.14(d-f). The feasibility in manipulating the porous superstructural plasmonic nanomotors is potent for the development of multifunctional nanorobots that can probe, sense, and release molecules on single cellular levels.

4.7 CONCLUSIONS

In summary, we designed and fabricated an original type of dual-functional plasmonic nanomotors with designed nanoporous superstructures. The unique nano-porosity made from a cyclic nanosphere-assembling-silica-coating process provides three-fold enhancement in specific surfaces areas and loading capacitance of biomolecules. The enhanced specific surface areas, owing to the embedded nanocavities, also support the growth of plasmonic Ag nanoparticles in 3D, offering approximately an order of magnitude improvement in the limit of Raman detection compared to that of non-porous control samples. Numerical simulation further unveiled the near-field electromagnetic coupling between the Ag nanoparticles in the nanocavities on adjacent concentric layers, in addition to the increased number of hotspots. By exploiting both the electric and plasmonic properties of the Ag nanoparticles, we successfully demonstrated a mechanism for actively tuning the release rate of biomolecules, and monitoring the release in quasi-real time. Finally, the plasmonic nanomotors are facilely motorized, including transport along both the X and Y directions, such as tracing letter “U”, and rotation. The concept, fabrication, and performances of the reported dual-functional biosensing-release device could inspire the development of the next-generation multifunctional Raman-sensing nanorobots for probing, stimulation, and detection for precision medicine.

Chapter 5: Bio-photonic-plasmonic micromotors for DNA capture and detection[**]

5.1 INTRODUCTION

Deoxyribonucleic acid (DNA) technology has revolutionized modern life and science. Recent advances in DNA technology including cloning, polymerase chain reaction (PCR), recombinant DNA technology, DNA fingerprinting, and gene therapy have shown great impacts on agriculture, medicine, environmental sciences, and forensic investigations.[224-227] The capture of DNA molecules on solid surfaces, which serves as the underlying mechanism for the vast majority of DNA preconcentration and separation techniques, is commonly used for extraction of DNA from biological samples in these DNA technologies.[228-231] Various solid particles, including silica,[232-234] polymers,[235-236] graphene,[90, 237] and gold nanoparticles,[238-239] have been investigated for DNA capture by either electrostatic interaction or covalent bonding.[240] Among these fascinating materials, silica nanoparticles have emerged as one of the most promising candidates due to their advantageous high surface area, surface functionalization capability, biocompatibility and low cost.[241-242] The mechanism of DNA capture on silica has been deeply investigated and been attributed to the increase in entropy.[243] The capture of DNA on the silica leads to the release of ordered water molecules hydrating on DNA and silica surface. Note that DNA and silica are both negatively charged in general and repel each other electrostatically. A low pH value of the binding buffer can result in the decrease of surface charge density, which reduces the electrostatic repulsion between DNA and silica. Similarly, a high ionic strength can compress the electrostatic double layer on silica surface and thus shield the electrostatic interaction. Therefore, current researches have been mostly focused on the developing of binding buffers with various compositions to facilitate DNA adsorption on silica by tuning the pH and ionic strength.[244-246] Various protocols have been reported and demonstrated with high capture throughput, high elution efficiency and excellent compatibility with downstream applications. However, it remains very challenging to improve the time-efficiency of the DNA capture processes at low concentration. It usually takes tens of minutes or even a few hours for the capture processes to be saturated in most reported protocols. Theoretical studies and reported experiments indicate that both the transport of molecules to the solid surface (including convection and diffusion) and the adsorption/reaction of molecules on the solid surface play critical roles in governing the capture kinetics.[247] Since the use of binding buffers has highly enhanced the adsorption process of DNA, the slow diffusion of DNA to the silica surface becomes the dominant time-limiting factor of the DNA capture kinetics.

[**] Portions of this chapter will be submitted to *Nature Methods*. As the leading author, J. Guo designed and performed the experiments, modelled the system, analyzed the data, and wrote the draft of the manuscript. As the faculty author, Professor D. Fan conceived this research and supervised the project. She analyzed data and modelled the system.

To address the aforementioned challenges, in this chapter we proposed and demonstrated a mechanically accelerating strategy for the capture and detection of DNA molecules by biosilica-based plasmonic micromotors. The main body of the micromotors, periodically nanoporous diatom frustules, forms hybrid photonic-plasmonic modes through the optical coupling with Ag nanoparticles for sensitive SERS detection and quasi-real-time monitoring. Based on a commercial magnetic stirrer, one of the most common equipment in chemistry and biology labs, the magnetic manipulation enabled the micromotors to transport and assemble in microwells and microfluidic channels, and rotated with tunable speed. The DNA capture was significantly accelerated during the rotation of the micromotors. The fundamental mechanism was investigated and attributed to the reduction of Nernst diffusion layer caused by the rotation, which significantly promoted the diffusion of DNA to the silica surface. The detection of DNA molecules at low concentration was also demonstrated to be much faster under rotation. To the best of our knowledge, this effect is demonstrated and applied in the capture and detection of molecules on the surface of micro/nanoparticles for the first time.

5.2 DESIGN AND FABRICATION OF BIO-PHOTONIC-PLASMONIC MICROMOTORS

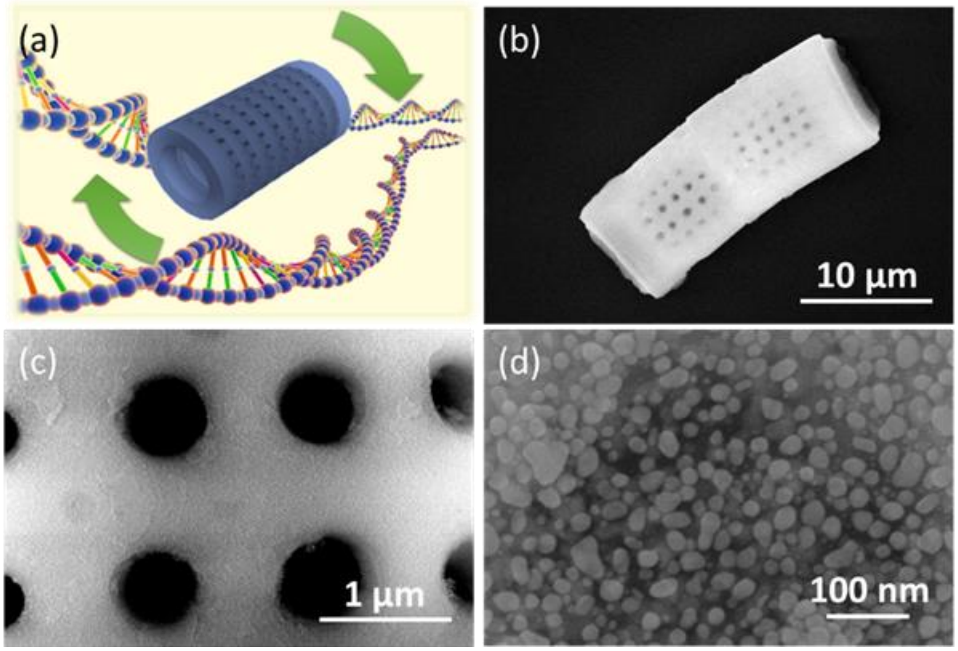

Figure 5.1: (a) Schematic of a rotating bio-photonic-plasmonic micromotor in DNA solutions. (b-d) SEM images of the porous periodic microstructure of diatom frustule at (b) low magnification and (c) high magnification, and (d) Ag nanoparticles synthesized on the surface.

Herein the bio-photonic-plasmonic micromotor is designed to consist of a diatom frustule as main body, with a semi-coated magnetic thin film and uniformly-coated plasmonic Ag nanoparticles [Figure 5.1(a)]. Diatoms are one of the most common and widespread types of photosynthetic microalgae and found abundantly in marine ecosystems. Frustules are the cell wall of diatoms, which have a porous periodic microstructure made of silica [Figure 5.1(b-c)].[248-249] These advanced natural biomaterials provide great opportunities in low-cost micro/nano-manufacturing. The mechanical strength and chemical stability of these diatom frustules suggest the excellence and feasibility of applying them as micromotors. They are also perfect candidates for DNA capture due to their composition of silica and large surface area. Moreover, preliminary calculations and reported works have demonstrated that their periodic nanopore arrays can act as photonic crystals to provide resonances with light and substantially boost localized electromagnetic fields for Raman measurements.[250-251] The diatom frustules used in this work are processed and refined from low-cost commercial diatomaceous earth powder *via* dispersion, sonication, filtration and calcination.[252] The diatomaceous earth powders are purchased from Natural Gardener (Austin, TX) at cheap price of 1 dollar per pound. Impurities and broken pieces of frustules are filtered out by filter papers (VWR® Grade 417 Filter Paper, size of particle retention: 40 µm). Then the diatom frustules are calcinated in air at 500 ˚C for 2 hours to remove organic residues. Most of the obtained diatom frustules have cylindrical microstructures with diameters ranging from 8 to 16 µm and lengths ranging from 20 to 35 µm [Figure 5.1(b)]. And then a bilayer metallic nano-thin-film of Ni/Au is deposited on one side of the diatom frustules for the magnetic manipulation by electron-beam evaporation. Here the Au layer works as a passivation layer that prevents magnetic aggregation of the diatom frustules in suspension. The ferromagnetic responses of Ni to external magnetic fields allows the alignment of diatom frustules in the direction of magnetic fields and their transport along magnetic field gradient toward high-field region. Finally, plasmonic Ag nanoparticles are uniformly synthesized on the surface of diatom frustules for SERS detection [Figure 5.1(d)].[89, 211] The synthesis of Ag nanoparticles has been introduced in Section 4.2. The plasmonic Ag nanoparticles are densely distributed with an average diameter of 23.38±3.30 nm and junctions ranging from 0.5 nm to 5 nm on diatom frustules.

5.3 CHARACTERIZATION AND SIMULATION OF SERS

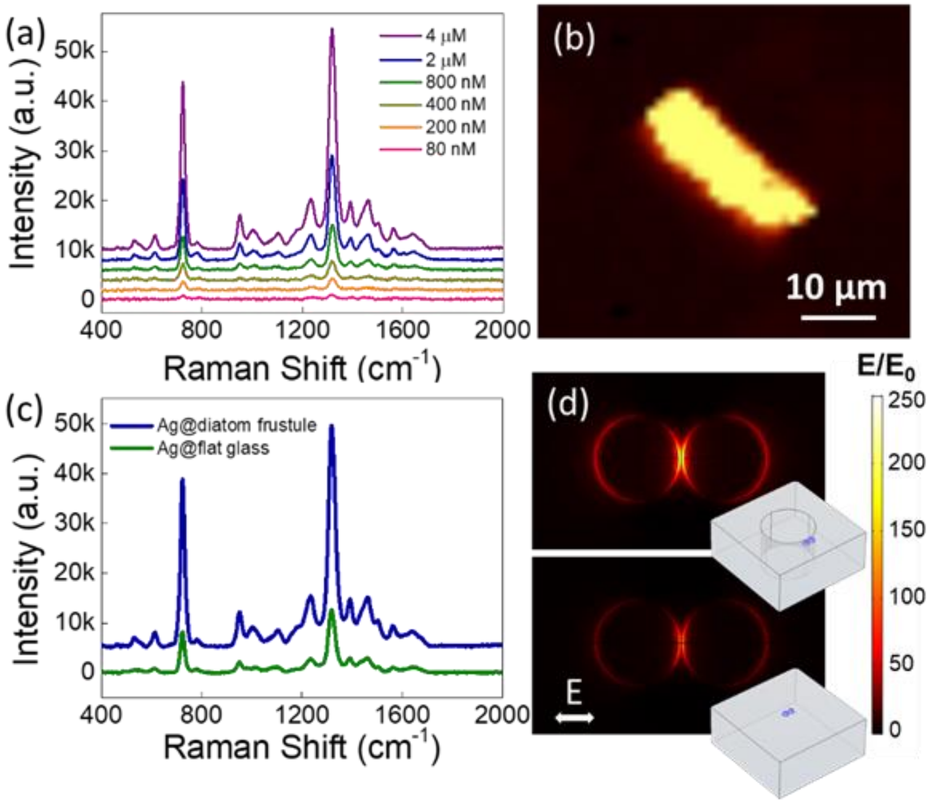

Figure 5.2: (a) SERS spectra of DNA from 80 nM to 4 μM. (b) Raman mapping of DNA (4 μM, 724 cm^{-1}) on a micromotor after 2-hour incubation. (c) SERS spectra of 4 μM DNA on a micromotor (blue) and on a Ag-nanoparticle coated flat glass substrate (green), respectively. (d) Simulations of electric field distributions around a pair of Ag nanoparticle dimer placed on a diatom frustule substrate (top) and a flat glass substrate (bottom), respectively. Insets are the schematics of the simulated structures with Ag nanoparticles highlighted. The out-plane incident laser is polarized horizontally.

In most reported works, the capture dynamics of DNA are revealed by measuring the DNA concentrations in solutions with Ultraviolet (UV) absorbance spectroscopy to determine the amounts of captured DNA with knowing initial DNA concentration.[253-254] DNA solution samples are taken at premeditated time for the measurement during the capture process. This method is invasive and not efficient. Herein we applied SERS measurements to directly detect the DNA captured on the silica surface and monitor their amounts in quasi-real-time. The micromotors were incubated in DNA solutions with concentrations ranging from 80 nM to 4 μM for 2 hours before measurements. A 532-nm laser with a spot of ~25 μm and power of 500 μW was used for SERS measurements. The exposure time for each test was 2 seconds. In Raman mapping, a 532-nm laser with a spot size of 1 μm and power of 100 μW was used. The exposure time for each testing point was 1 second.

The SERS performance of the photonic-plasmonic micromotors is characterized and understood by both experimentation and numerical simulation. Raman signals of DNA are detected as shown in Figure 5.2(a) after incubating in a series of DNA solutions with concentrations ranging from 80 nM to 4 μM for 2 hours. The detection limit is as low as 80 nM with a signal-to-noise ratio of 4.21 at 724 cm^{-1} and 5.79 at 1319 cm^{-1} (both attributed to the vibration of nuclear base adenine), respectively.[255-256] The Raman mapping of DNA molecules shown in Figure 5.2(b) confirms the uniform distribution of hotspots on the micromotors. The Raman signal measured on the micromotors is compared to that measured on a flat glass substrate with same Ag nanoparticles coating [Figure 5.2(c)]. The signal intensity is enhanced by a factor of 3.66 ± 0.31, for major DNA Raman peaks at 724 cm^{-1}, 957 cm^{-1} (attributed to vibration in the deoxyribose moiety), 1235 cm^{-1} (attributed to the vibration of nuclear base thymine and cytosine), 1319 cm^{-1} and1391 cm^{-1} (attributed to the vibration of nuclear base guanine).[255-256] The additional enhancement of Raman signals is attributed to the enhanced localized surface plasmon resonance due to their coupling with the guided-mode resonance of the photonic microstructure of the diatom frustule.[250-251] It is further confirmed by our numerical simulation in Figure 5.2(d). The calculated maximum enhancement factor of the electric field around a pair of Ag nanoparticle dimer placed on a diatom frustule substrate is around two times of that on a flat glass substrate. The great Raman sensitivity allows precision and non-invasive detection for determining both the chemistry and amounts of DNA molecules captured on micromotors simultaneously in the following experiments.

5.4 MAGNETIC MANIPULATION AND INDIVIDUAL SELF-ASSEMBLY OF MICROMOTORS

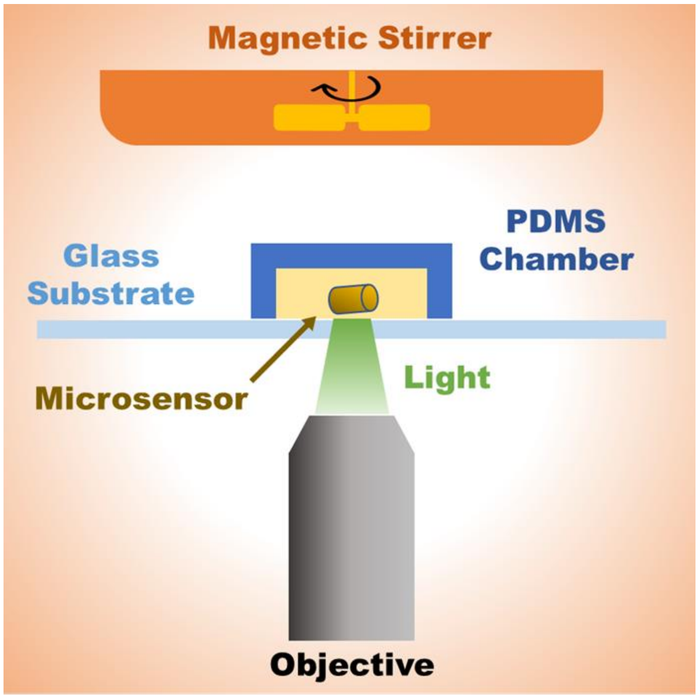

Figure 5.3: Schematic of the experimental setup for robotization.

The robotization of the micromotors in the binding buffer of DNA is much more challenging than that in DI water or non-ionic buffer. The mobility of the micromotors in suspension is mainly hindered by viscosity, friction, and adhesion, which are influenced by the surface interaction between micromotors and substrate, and the gravity of micromotors.[95-96, 145, 252] As aforementioned, the binding buffers with low pH value and high ionic strength significantly reduce the Debye length of electrostatic double layers and diminish the electrostatic repulsion, resulting in much stronger hindering force from friction and adhesion. Moreover, the dramatic decrease in the gap height between micromotors and substrate also induces additional hydrodynamic drag forces.[155]

To overcome this challenge, we strategically apply magnetic fields for the robotization of micromotors. The magnetic fields are generated by a commercial magnetic stirrer placing on the top of the micromotors as shown in Figure 5.3. This setup uses the common equipment in chemistry and biology labs without complicated instrumentation, thus it can be readily accessible and adopted in biological and clinic researches. In the non-uniform external magnetic field (B), the micromotors coated with magnetic film receive an upward force proportional to the field gradient, $\boldsymbol{F_m} = (\boldsymbol{m} \cdot \boldsymbol{\nabla})\boldsymbol{B}$, where m is the magnetic moment of micromotors.[20, 25] Balancing with the gravity of micromotors, the upward magnetic force greatly reduces the friction and adhesion.

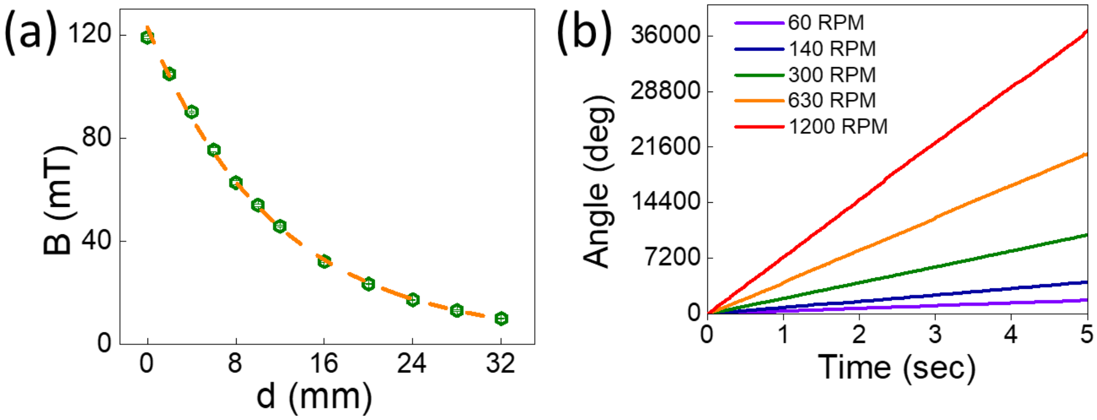

Figure 5.4: (a) Magnetic field strength (B) *versus* the distance (d) between permanent magnet on magnetic stirrer and micromotors. (b) Rotation angle *versus* time at different rotation speed.

After lessening resistance, the micromotors can facilely be transported by the in-plane magnetic-field-gradient force, and be aligned by the magnetic torque, $\boldsymbol{\tau_m} =$

$\boldsymbol{m} \times \boldsymbol{B}$.[23, 257] When the magnetic stirrer starts to rotate, the magnetic torque increases with the angle (θ) between magnetic moment of micromotors m and magnetic field B, and thus speeds up the micromotors until the drag torque $\boldsymbol{\tau_d}$ is equal to the magnetic torque $\boldsymbol{\tau_m}$. Then the magnetic torque could drive the rotation of micromotors at a synchronous speed. When $\boldsymbol{\theta = 90^\circ}$, the theoretical maximum rotation speed is reached, which can be determined by $\boldsymbol{\tau_m = \tau_d}$. The drag torque for micromotors can be calculated by $\boldsymbol{\tau_d = \frac{1}{3}c\pi\eta l^3\omega}$, where η is the viscosity of water, l is the length of the micromotors, ω is the angular rotation speed and c is a constant related to the aspect ratio of micromotors. Specifically, $\boldsymbol{c = 0.53}$ is used in this calculation. The magnetic moment of micromotors can be estimated by $\boldsymbol{m = VM_s = \pi rlhM_s}$, where V is the volume of the Ni film, r is the diameter of the micromotors, h is the thickness of Ni film, and the spontaneous magnetization of Ni film $\boldsymbol{M_s = 485 \times 10^3\ A/m}$. As shown in Figure 5.4 (a), the applied magnetic field strength can be controlled by tuning the height of the magnetic stirrer. In the experiments, the distance (d) between permanent magnet and micromotors is set as 2 cm with a magnetic field of 23.37 ± 0.25 mT. Assuming the size of micromotors is 25 μm in length and 10 μm in diameter, the theoretical maximum rotation speed is calculated as $\boldsymbol{1.06 \times 10^5}$ rpm.[257]

As long as the rotation speed of the magnetic field does not exceed the theoretical maximum value, the micromotors will rotate synchronously with the magnetic field. Otherwise, the rotation of micromotors will have periodic fluctuations in speed. Since the maximum rotation speed of the magnetic stirrer is 1200 rpm, the micromotors always rotate synchronously with the magnetic stirrer at a uniform speed in the experiments [Figure 5.4(b)]. With the guidance of the magnetic field, the micromotors can self-assemble into microwells at targeted location for localized Raman sensing [Figure 5.5(a)], or into microfluidic channels for mixing and pumping purpose [Figure 5.5(b)].

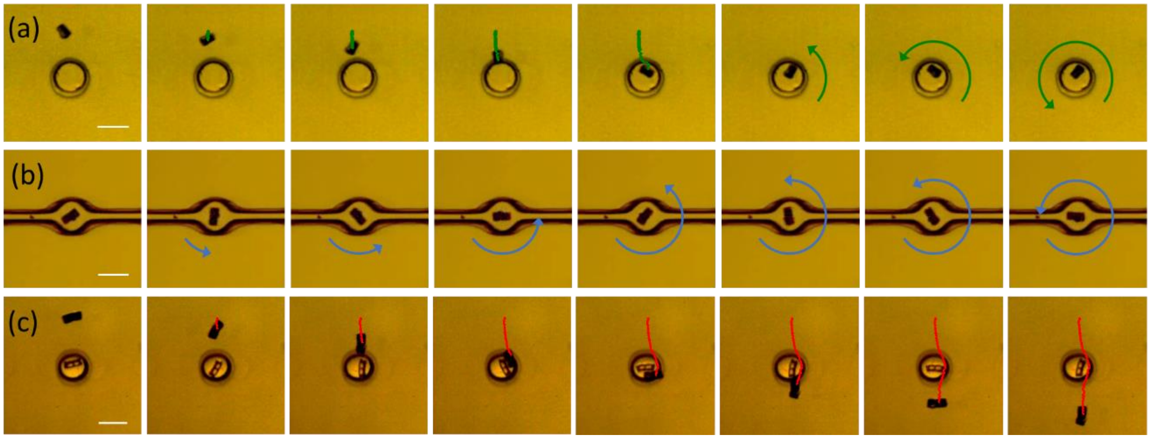

Figure 5.5: (a) Snapshots of a micromotor rotating and self-assembling into a microwell. First 5 snapshots are taken every 1 second and others are taken every 0.05 second. (b) Snapshots of a micromotor rotating in a microfluidic channel every 0.025 second. (c) Snapshots of a micromotor rotating at 300 rpm and passing by an occupied microwell every second. Scalebar in all is 30 μm.

To avoid the magnetic inter-attraction and aggregation of micromotors, the self-assembly process is operated in concurrence with the rotation of micromotors. The synchronously rotating micromotors experience a hydrodynamic repulsion on each other, which increases with the Reynold number and thus the rotation speed.[258] Therefore, the micromotors repel each other at high rotation speeds, no matter whether they are approached end by end (magnetically attracting) or side by side (magnetically repelling). This strategy for assembling single micromotor in individual microwell is demonstrated by both experiment and simulation. As shown in Figure 5.5(c), when the micromotor encounters a microwell that is occupied by another micromotor on its path, it makes a detour around and then moves forward. The orientations of these two micromotors in every frame of Figure 5.5(c) also further confirm that they rotate synchronously all the time. Figure 5.6 shows the COMSOL simulations of the fluidic fields around two approaching micromotors rotated at 0˚, 45˚, 90˚, and 135˚, respectively. The simulation results indicate that the fluid flows generated by two rotating micromotors produce a repulsion force at all configurations when approaching each other. This method can be extended to large array single-particle self-assembling in various applications.[259-260]

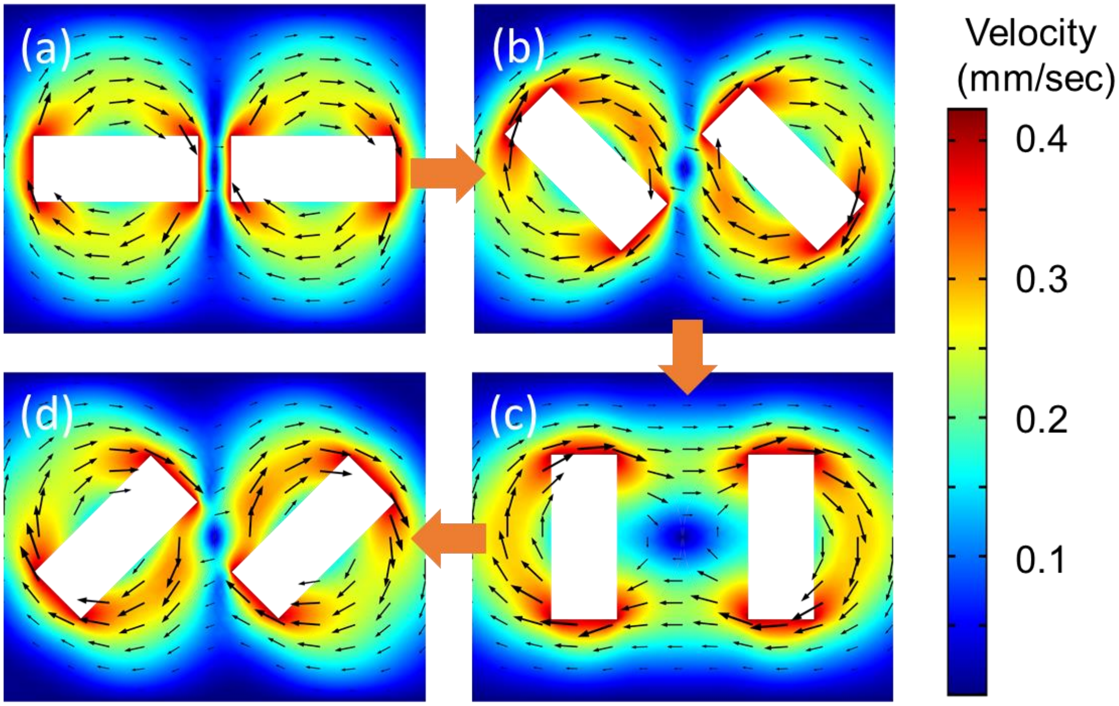

Figure 5.6: Simulation of the fluidic fields around two approaching micromotors rotated at (a) 0° (end by end), (b) 45°, (c) 90° (side by side), and (d) 135°, respectively.

5.5 MECHANICALLY ACCELERATED CAPTURE AND DETECTION OF DNA MOLECULES

After the micromotors are assembled in the designated position, the mechanically accelerated capture of DNA molecules on micromotors and the involved fundamental mechanisms were investigated. Salmon sperm DNA used for the demonstration was purchased from Invitrogen @ Thermo Fisher Scientific (Carlsbad, CA). As stated by the manufacturer, the DNA was extracted by phenol-chloroform and sheared to an average size of < 2000 bp. The composition of the binding buffer used was 50 mM tris(hydroxymethyl)aminomethane (Tris), 0.25 mM acetic acid and 40 mM potassium ions (K^+), with pH equal to 4. Potassium hydroxide (KOH) or hydrochloric acid (HCl) was used to adjust the pH value. The DNA solutions (2× predetermined concentrations) were pipetted and rapidly mixed with the binding buffers (3× predetermined concentrations) and the suspensions of micromotors with a volume ratio of 3:2:1. The capture dynamics at room temperature were characterized by SERS, in which the DNA concentration in the mixture is 500 μg/mL, the total volume of solution after mixing is 18 μL, and the weight percentage of micromotors in suspension is ~ 10 μg/mL. At this concentration, there are only a few micromotors in the mixed solution. In this case, the DNA concentration in the solution remains constant during the capture process because very minor amounts of DNA are captured. The capture dynamics at different temperatures were characterized by UV absorbance spectroscopy, in which the DNA concentration in the mixture is 500 μg/mL, the total volume of solution after mixing is 120 μL, and the weight percentage of micromotors in suspension is ~ 50 mg/mL. In this case, large amounts of DNA are captured so that the concentration change of DNA in the solution is detectable by the UV spectroscopy. The DNA capture dynamics at different temperatures are conducted in refrigerator (at 5 ˚C) or in thermostatic water bath (at 25 ˚C and 45 ˚C, respectively). The DNA solutions, binding buffers and the suspensions of micromotors are all pre-cooled or pre-heated in designated temperatures for 30 minutes before mixing.

For the capture dynamics characterized by SERS, once the DNA solutions and binding buffers are pipetted and rapidly mixed with the suspension of micromotors, the concentrations of DNA captured on the static or rotating micromotors are detected continuously. The laser has a spot size of ~ 25 μm so that the DNA molecules captured on the entire micromotors can be detected. The laser power is 500 μW. The exposure time for each testing point is 10 seconds. Since the plasmonic hotspots for SERS detection exist in the vicinity of Ag nanoparticles and their narrow junctions, only the DNA captured on the surface of micromotors can be detected. As shown in Figure 5.7, Raman intensity of DNA increases almost linearly with the DNA concentrations within the tested concentration ranging. Therefore, the Raman signals obtained in quasi-real-time directly reveal the concentration of DNA captured on the surface. Note that, according to Langmuir adsorption model, the concentration of molecules adsorbed on the surface at equilibrium ($C_{s,eq}$) is related to the concentration of solutions (C_0) by following equation:[261]

$$C_{s,eq} = C_{s,max} \frac{K_{eq} C_0}{1 + K_{eq} C_0} \qquad (5.1)$$

where $C_{s,max}$ is the maximum adsorption capacity of molecules on this material, and K_{eq} is the adsorption equilibrium constant. Therefore, the linear plot of the Raman intensity *versus* DNA concentration indicates that the amounts of DNA adsorbed on diatom frustule are way below the maximum adsorption capacity in this concentration ranging of solutions.

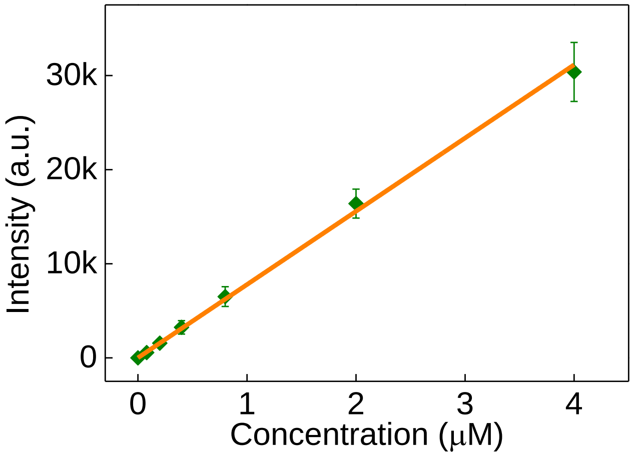

Figure 5.7: Raman intensity of DNA at 724 cm^{-1} *versus* DNA concentration.

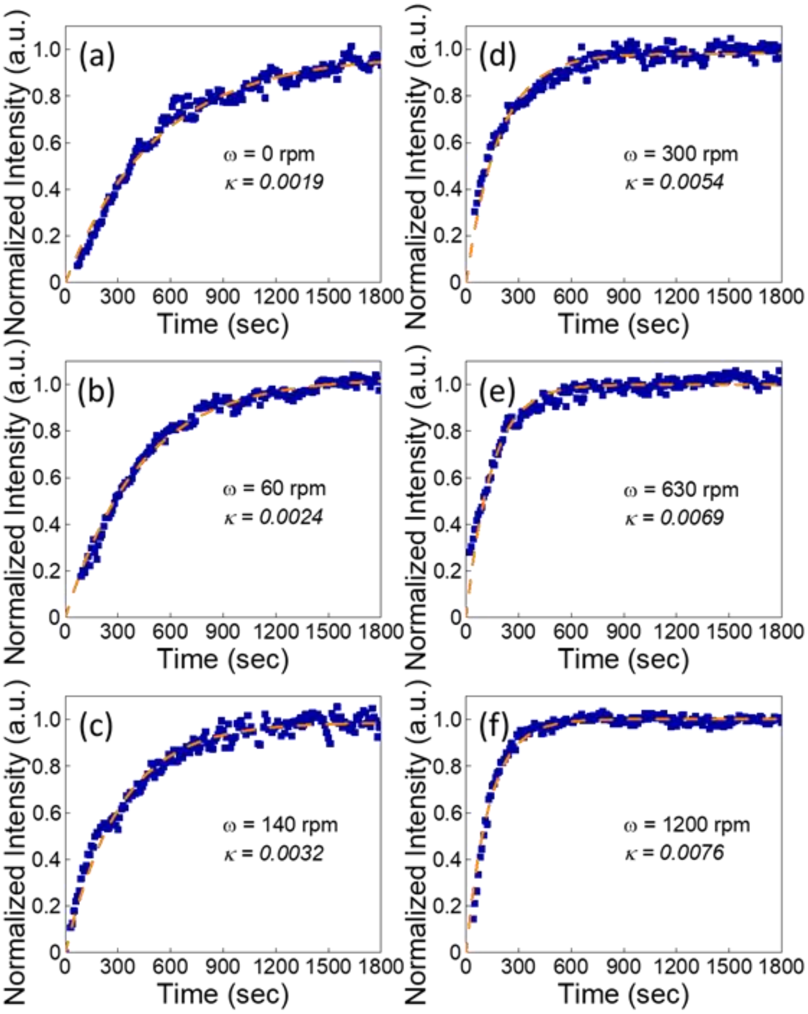

Figure 5.8: Capture dynamics of DNA revealed by SERS on (a) a static micromotor and (b-f) rotating micromotors at 60-1200 rpm, respectively.

The capture dynamics of DNA monitored by quasi-real-time SERS measurements on static or rotating micromotors with rotating speed from 60 to 1200 rpm are presented in Figure 5.8. The DNA concentration measured by the Raman spectroscopy increases with time monotonically until it reaches equilibrium. The rotation of micromotors greatly speeds up the attainment of equilibrium. As shown in Figure 5.9, the time needed to attain 95% of the final equilibrium DNA capturing decreases exponentially with the rotation speed, from

~ 28 minutes at static state to ~ 7 minutes at a rotation speed of 1200 rpm. Even at a low rotation speed of 300 rpm, the capturing process saves two-thirds of time compared to that of a static micromotor. Although the decreasing trend slows down at high rotation speed, the 4-fold enhancement in time-efficiency has been a significant advance for the DNA capture.

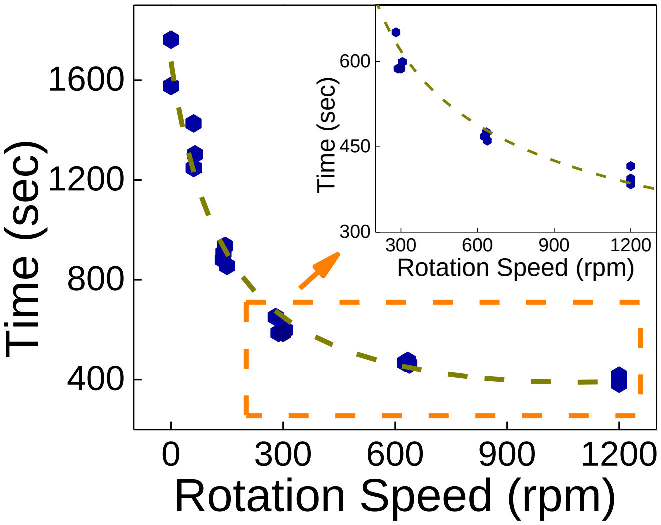

Figure 5.9: Time needed to attain 95% of the final equilibrium DNA capture *versus* rotation speed of micromotors.

Herein the capturing kinetics of DNA on micromotors are understood and modeled by Nernst diffusion theory and Langmuir adsorption theory.[261-262] As shown in Figure 5.10, the capture of DNA molecules from the bulk solution to the silica surface is considered to include three steps: the convection-dominated transport of DNA to the outer boundary of stationary Nernst diffusion layer, the diffusion-dominated transport of DNA inside the Nernst diffusion layer, and the adsorption of DNA on the silica surface.[263] According to the Nernst diffusion theory, the Nernst diffusion layer is the stationary liquid region at the interface of solid surface and liquid medium, in which the mass transport only proceeds in the form of passive diffusion driven by the concentration gradient.[262] Due to the mechanical mixing and the rotation of micromotors, the DNA concentration is considered as constant in the region of strong convention. Therefore, the capturing kinetics are dominated by the diffusion process and adsorption process.

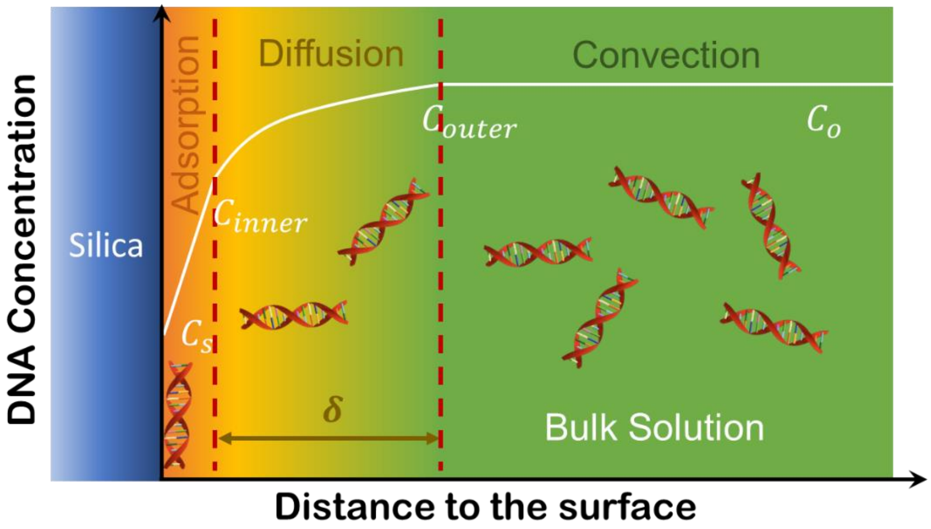

Figure 5.10: Schematic model of the DNA capture dynamics including convection, diffusion, and adsorption.

In the Nernst diffusion layer, the concentration gradient between its outer and inner boundaries motivates the diffusion kinetics of DNA following the Fick's diffusion laws:[262]

$$C_{inner} = C_{outer} - C_{outer} \cdot e^{-k_d t} \qquad (5.2)$$

where C_{inner} and C_{outer} are the DNA concentrations at the inner and outer boundaries, respectively, and C_{outer} equals to the concentration in bulk solutions (C_0). The diffusion rate k_d is inversely proportional to the thickness of Nernst diffusion layer (δ). According to the Levich boundary layer theory,[264] the shear flow on the solid surface resulted from the rotation of micromotors can reduce the thickness of Nernst diffusion layer: $\delta \propto \omega^{-0.5}$, where ω is the rotation speed of micromotors. Therefore, the diffusion kinetics of DNA is influenced by the rotation of micromotors by $k_d \propto \omega^{0.5}$. On the other hand, in the adsorption process modeled by Langmuir adsorption theory, the time dependent concentration of DNA adsorbed on the surface (C_s) is given by the Lagergren equation:[261]

$$C_s = C_{s,eq} - C_{s,eq} \cdot e^{-k_a t} \qquad (5.3)$$

where the adsorption rate k_a is independent of the rotation behavior of micromotors. Here the diffusion kinetics [Equation (5.2)] and adsorption kinetics [Equation (5.3)] associate with each other by the capturing equilibrium [Equation (5.1)], and compete to each other in the domination of capturing kinetics. Since the diffusion kinetics and adsorption kinetics have a similar form of equations, we simplify the modeling of the capture kinetics by the following equation:

$$C_s = C_0 - C_0 \cdot e^{-kt} \qquad (5.4)$$

where k is the capture rate. If the diffusion is the dominant time-limiting factor in the capture kinetic ($k_d < k_a$), k corresponds to k_d; on the contrary, if the adsorption dominates ($k_a < k_d$), k corresponds to k_a.

The dominant process in the capturing kinetics on static micromotors is firstly investigated by capturing the DNA molecules at different temperatures. Since the DNA capture dynamics at different temperatures is conducted in refrigerator or in thermostatic water bath, UV spectroscopy is used here to determine the concentrations of DNA solutions instead of quasi-real-time SERS measurements. DNA solutions (1 μL) are taken at premeditated time for every UV spectroscopy measurement. The DNA concentrations are determined by using NANODROP 1000 spectrophotometer (Thermo Fisher Scientific) and the final results of concentration are the averages of 5 tests. As shown in the plots of DNA concentrations in bulk solution *versus* time (Figure 5.11), the initial slope increases with temperature. Note that the adsorption of DNA on the silica surface in binding buffer with pH lower than 7 is exothermic, while the diffusion process is promoted by thermal energy.[243] This indicates that the capture rate of DNA without rotation is limited by diffusion kinetics.

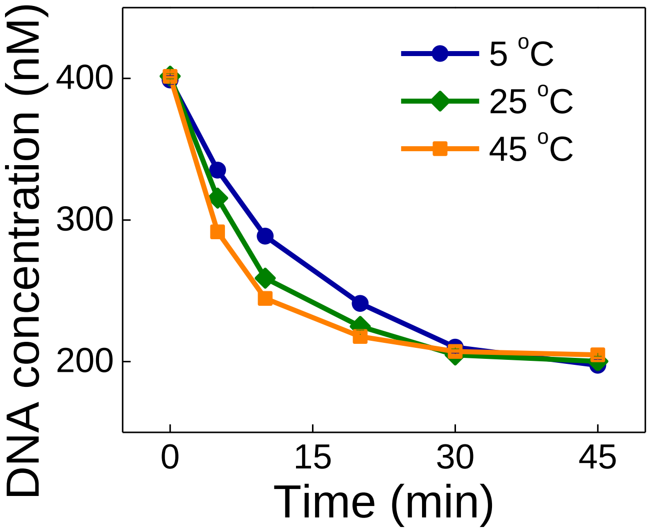

Figure 5.11: Capture dynamics of DNA at different temperatures: DNA concentrations in bulk solution *versus* time measured by UV spectroscopy.

Moreover, the capture rates k at different rotation speeds are obtained by fitting the capture dynamics with Equation (5.4). As shown in the log-log plot of k *versus* ω [Figure 5.12], k monotonically increased with ω ranging from 60 rpm to 300 rpm, with a power-law dependence of 0.49 ± 0.02. The results quantitatively agree with our modeling ($k_d \propto \omega^{0.5}$), and further demonstrate that the diffusion process dominates the capture kinetics at low rotation speed. The deviation of data points from the fitting curve at high rotating speed indicates the competition between the diffusion kinetic and adsorption kinetic. This phenomenon can be understood by our modeling: at low rotation speed, the diffusion process is slow ($k_d < k_a$) and limits the capture process, therefore k corresponds to k_d and has an inverse-square-root dependence on ω; at high rotation speed, the k_d is accelerated and becomes competitive with the k_a, both of which contribute to the capture dynamics.

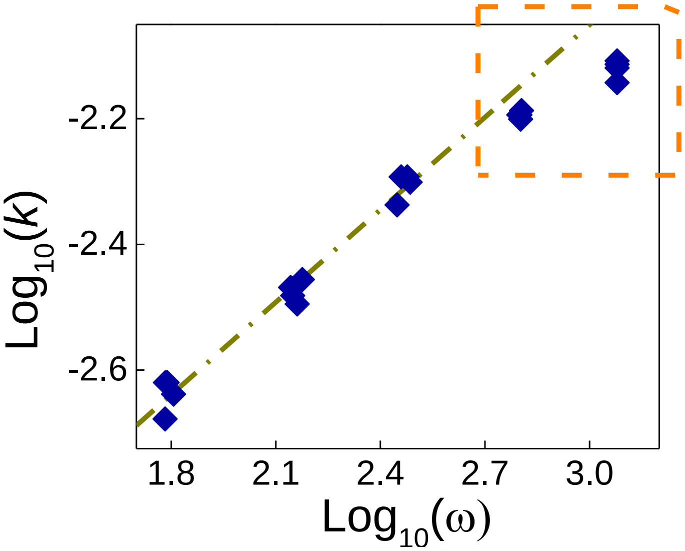

Figure 5.12: Log-log plot of capture rate (k) *versus* rotation speed (ω in rpm) of micromotors. The orange dash line is the linear fitting of data ranging from 60 rpm to 300 rpm.

With the above experimental demonstration and theoretical understanding, we further apply this mechanically accelerated capture strategy in the high-speed SERS detection of low-concentration DNA. Regardless of the detection mechanisms as optical, mechanical, or electrical, the high sensitivity comes at the expense of an adversely long detection time for low-concentration analytes.[265-266] This challenge originates from the slow diffusion of analytes to the surfaces of micro/nanosensors due to the low concentration gradient. Herein, we overcome this problem by thinning the Nernst diffusion layer with mechanical rotation of micromotors to accelerate the diffusion of analytes for detection. The DNA samples with a low concentration of 80 nM are tested on a static micromotor and a micromotor rotating at a speed of 630 rpm, respectively. Figure 5.13

presents the Raman spectra of DNA measured at premeditated moments after mixing on both static and rotating micromotors. The Raman peak at ~780 cm^{-1} attributed to silica on the micromotor is used as a reference peak here. On the static micromotor, the Raman signal of DNA at 724 cm^{-1} is hardly observable at the first 3 minutes, and become gradually clear at ~ 10 minutes. The rotating micromotor detects DNA with same concentration in a much faster manner. It reveals a similar Raman signal intensity in 3 minutes compared to that of 10 minutes on static micromotor, that is, an approximately 3-time improvement in detection time-efficiency. This mechanically accelerated capture strategy demonstrated here is not limited to the detection of DNA molecules. It could be applied in other detection techniques based on surface capture.

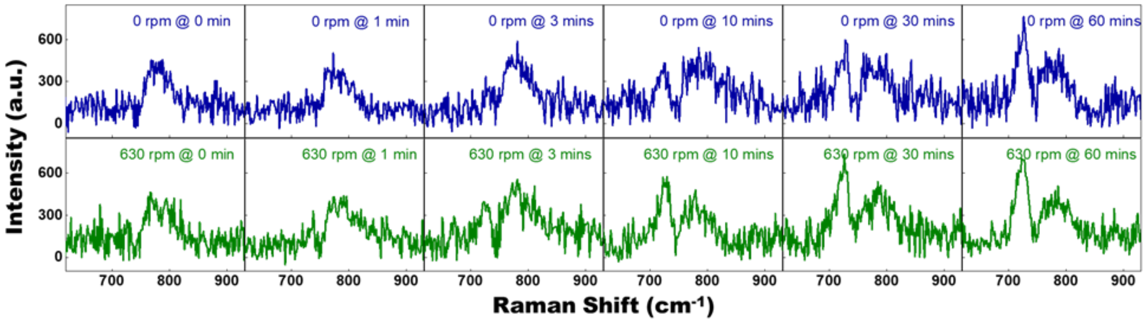

Figure 5.13: Raman spectra of DNA (80 nM) measured at premeditated moments in an hour after mixing on both static and rotating micromotors at a rotation speed of 630 rpm.

5.6 CONCLUSIONS

In summary, an original mechanism for high-speed capture and detection of low-concentration DNA molecules is reported in this chapter. The photonic-plasmonic micromotors made of diatom frustules with low-cost provide biocompatible large surface area of silica for DNA capture, and periodic nanopore arrays coupling with plasmonic hotspots for sensitive SERS measurements and in-quasi-real-time monitoring. The micromotors are transported to specific locations, self-assembled in microwells or microfluidic channels and rotated with tunable speeds by the nano-manipulation based on a commercial magnetic stirrer. By thinning the stationary Nernst diffusion layer through the rotation of micromotors, the capture process of DNA is accelerated by up to 4 times at a rotation speed of 1200 rpm. The high-speed detection of DNA at low concentration is also demonstrated with a 3-fold enhancement in time-efficiency at a rotation speed of 630 rpm. The fundamental mechanism is thoroughly discussed and modeled by Nernst diffusion theory and Langmuir adsorption theory, which could inspire new devices, strategies and advances in accelerating diffusion, molecule enrichment, and high-speed detection for various applications.

Chapter 6: Conclusions

In conclusion, innovative artificial micro/nanomachines with precise manipulation and high performance are reported in this dissertation. Rotary micro/nanomotors are precisely assembled at predetermined locations (nanobearing or microwells) and effectively rotated in a controllable manner. The micro/nanomotors can be powered by diverse input energy, including electric fields, magnetic fields, or chemical reactions. Electric tweezers or magnetic tweezers are applied for the manipulations of micro/nanomotors with fine control. Nanomotors with ultrasmall size, ultrafast velocity and ultradurable lifetimes are demonstrated. Synthesis of plasmonic nanoparticles on the micro/nanomotors allows the integration of sensing and detection function. The powerfulness of these innovative micro/nanomotors is demonstrated in applications of cargo delivery, NEMS assembly, localized biochemical detection, controllable drug delivery and release, accelerated biomolecule capture and detection.

The innovations of artificial micro/nanomachines including concept, design, fabrication, manipulation, and bioapplications in this dissertation, are expected to inspire various research areas including NEMS, nanorobotics, microfluidics, biochemical delivery, and diagnostic sensing.

Appendix: List of publications

Journal publications:

1. K. Kim[#], X. Xu[#], **J. Guo[#]**, D. L. Fan, "Ultrahigh-Speed Rotating Nanoelectromechanical System Devices Assembled from Nanoscale Building Blocks", ***Nature Communications***, 5, 3632 (2014).

2. **J. Guo**, K. Kim, K. W. Lei, D. L. Fan, "Ultra-Durable Rotary Micromotors Assembled from Nanoentities by Electric Fields", ***Nanoscale***, 7, 11363-11370 (2015).

3. **J. Guo**, A. Chan, W. Li, D. L. Fan, "Kirkendall Effect in Creating Three-Dimensional Metal Catalysts for Hierarchically Porous Ultrathin Graphite with Unique Properties", ***Chemistry of Materials***, 29, 4991-4998 (2017).

4. **J. Guo**, J. J. Gallegos, A. R. Tom, D. L. Fan, "Electric-Fields Guided Precision Manipulation of Catalytic Nanomotors for Cargo Delivery and Powering Nanoelectromechanical Devices", ***ACS Nano***, 12, 2, 1179-1187 (2018).

5. **J. Guo**, D. L. Fan, "Electrically Controlled Biochemical Release from Micro/Nanostructures for In-Vitro and In-Vivo Applications: a Review", ***ChemNanoMat***, DOI: 10.1002/cnma.201800157 (2018) (invited review).

6. J. Liu[#], **J. Guo[#]**, G. Meng, D. L. Fan, "Porous Superstructural Raman Nanosensors for Ultrasensitive Biochemical Detection and Electrically Controlled Molecule Release", ***Chemistry of Materials***, DOI: 10.1021/acs.chemmater.8b01979 (2018).

7. **J. Guo**, K. Kim, P. Vandeventer, D. L. Fan, "Remarkable Acceleration of DNA Capture and Detection by Robotizing Bio-Photonic-Plasmonic Microsensors", draft in revision.

8. **J. Guo[#]**, J. Liu[#], G. Meng, D. L. Fan, "Microfluidic Platform with Integrated

Silicon Nanorods for Separation, Preconcentration and SERS Detection", in preparation.

9. **J. Guo**#, T. Liu#, D. L. Fan, "Light-driven Hollow Titania Micromotors for Localized SERS Detection", in preparation.

10. K. Kim, **J. Guo**, X. Xu, D. L. Fan, "Micromotors with Step-Motor Characteristics by Controlled Magnetic Interactions among Assembled Components", ***ACS Nano***, 9, 548-554 (2015).

11. K. Kim, **J. Guo**, X. Xu, D. L. Fan, "Recent Progress on Man-Made Inorganic Nanomachines", ***Small***, 11, 4037-4057 (2015) (invited review).

12. K. Kim, **J. Guo**, Z Liang, F. Q. Zhu, D. L. Fan, "Rotary Nanomotors: A Review of Recent Development", ***Nanoscale***, 8, 10471-10490 (2016) (invited review).

13. C. Zu, L. Li, **J. Guo**, S. Wang, D. L. Fan, A. Manthiram, "Understanding the Redox Obstacles in High Sulfur-Loading Li-S Batteries and Design of an Advanced Gel Cathode", ***Journal of Physical Chemistry Letters***, 7, 1392-1399 (2016).

14. W. Li, **J. Guo**, D. L. Fan, "Three-Dimensional Graphite-Polymer Flexible Strain Sensors with Ultra-sensitivity and Durability for Real-Time Human Vital Sign Monitoring and Musical Instrument Education", ***Advanced Materials Technologies***, 2, 1700070 (2017) (featured on the front cover).

15. W. G. Li, X. B. Xu, C. Liu, M. Tekell, J. Ning, **J. Guo**, J. C. Zhang, D. L. Fan, "Ultralight and Binder-Free All-Solid-State Flexible Supercapacitors for Powering Wearable Strain Sensors", ***Advanced Functional Materials***, 25, 1702738 (2017). (featured on the inside back cover).

16. K. Kim, **J. Guo**, Z. X. Liang, D. L. Fan, "Artificial Micro/Nanomachines for Bio-applications: Biochemical Delivery and Diagnostic Sensing", ***Advanced Functional Materials***, 1705867, (2018) (invited review).

# These authors contribute equally.

Book publications:

1. **J. Guo**, D. L. Fan, "Electromagnetic Wave Enabled Micro/nanorobotic Devices and Their Applications" Light Robotics – Structured-Mediated Nanobiophotonics, Elsevier (2017).

2. Z. Liang, **J. Guo**, D. L. Fan, "Manipulation, Assembling, and Actuation of Nanomotors by the Electric Tweezers", Robotic Systems and Autonomous Platforms, Elsevier (2018).

References

(1) Kim, K.; Guo, J. H.; Xu, X. B.; Fan, D. L., Recent Progress on Man-Made Inorganic Nanomachines. *Small* **2015,** *11*, 4037-4057.

(2) Kim, K.; Guo, J.; Liang, Z.; Fan, D., Artificial Micro/Nanomachines for Bioapplications: Biochemical Delivery and Diagnostic Sensing. *Advanced Functional Materials* **2018,** *0*, 1705867.

(3) A., O. G.; I., M.; S., F. B.; A., A., Dream Nanomachines. *Advanced Materials* **2005,** *17*, 3011-3018.

(4) Happel, J.; Brenner, H., *Low Reynolds number hydrodynamics: with special applications to particulate media*. Springer Netherlands: 2012.

(5) Jones, T. B.; Jones, T. B., *Electromechanics of Particles*. Cambridge University Press: 2005.

(6) Masliyah, J. H.; Bhattacharjee, S., *Electrokinetic and Colloid Transport Phenomena*. Wiley: 2006.

(7) Fan, D. L.; Zhu, F. Q.; Cammarata, R. C.; Chien, C. L., Electric Tweezers. *Nano Today* **2011,** *6*, 339-354.

(8) Fan, D. L.; Cammarata, R. C.; Chien, C. L., Precision Transport and Assembling of Nanowires in Suspension by Electric Fields. *Applied Physics Letters* **2008,** *92*, 093115.

(9) Freer, E. M.; Grachev, O.; Duan, X.; Martin, S.; Stumbo, D. P., High-yield self-limiting single-nanowire assembly with dielectrophoresis. *Nature Nanotechnology* **2010,** *5*, 525.

(10) Raychaudhuri, S.; Dayeh, S. A.; Wang, D.; Yu, E. T., Precise Semiconductor Nanowire Placement Through Dielectrophoresis. *Nano Letters* **2009,** *9*, 2260-2266.

(11) Pohl, H. A., *Dielectrophoresis : the behavior of neutral matter in nonuniform electric fields*. Cambridge University Press: Cambridge; New York, 1978.

(12) Fan, D. L.; Zhu, F. Q.; Cammarata, R. C.; Chien, C. L., Efficiency of Assembling of Nanowires in Suspension by AC Electric Fields. *Applied Physics Letters* **2008,** *92*.

(13) Fan, D. L.; Zhu, F. Q.; Cammarata, R. C.; Chien, C. L., Controllable High-Speed Rotation of Nanowires. *Physical Review Letters* **2005,** *94*, 247208.

(14) Crick, F. H. C.; Hughes, A. F. W., The physical properties of cytoplasm. *Experimental Cell Research* **1950,** *1*, 37-80.

(15) Dreyfus, R.; Baudry, J.; Roper, M. L.; Fermigier, M.; Stone, H. A.; Bibette, J., Microscopic artificial swimmers. *Nature* **2005,** *437*, 862-865.

(16) Gao, W.; Sattayasamitsathit, S.; Manesh, K. M.; Weihs, D.; Wang, J., Magnetically Powered Flexible Metal Nanowire Motors. *Journal of the American Chemical Society* **2010,** *132*, 14403-14405.

(17) Fischer, P.; Ghosh, A., Magnetically actuated propulsion at low Reynolds numbers: towards nanoscale control. *Nanoscale* **2011,** *3*, 557-563.

(18) Tottori, S.; Zhang, L.; Qiu, F.; Krawczyk, K. K.; Franco-Obregon, A.; Nelson, B. J., Magnetic helical micromachines: fabrication, controlled swimming, and cargo transport. *Adv Mater* **2012,** *24*, 811-6.

(19) Mandal, P.; Chopra, V.; Ghosh, A., Independent Positioning of Magnetic Nanomotors. *ACS Nano* **2015,** *9*, 4717-4725.

(20) Timonen, J. V. I.; Grzybowski, B. A., Tweezing of Magnetic and Non-Magnetic Objects with Magnetic Fields. *Advanced Materials* **2017,** *29*, 1603516-n/a.

(21) Sarkar, R.; Rybenkov, V. V., A Guide to Magnetic Tweezers and Their Applications. *Frontiers in Physics* **2016,** *4*.

(22) Peyer, K. E.; Zhang, L.; Nelson, B. J., Bio-inspired magnetic swimming microrobots for biomedical applications. *Nanoscale* **2013,** *5*, 1259-1272.

(23) Zhang, L.; Petit, T.; Lu, Y.; Kratochvil, B. E.; Peyer, K. E.; Pei, R.; Lou, J.; Nelson, B. J., Controlled Propulsion and Cargo Transport of Rotating Nickel Nanowires near a Patterned Solid Surface. *ACS Nano* **2010,** *4*, 6228-6234.

(24) Erb, R. M.; Martin, J. J.; Soheilian, R.; Pan, C.; Barber, J. R., Actuating Soft Matter with Magnetic Torque. *Advanced Functional Materials* **2016,** *26*, 3859-3880.

(25) Neuman, K. C.; Nagy, A., Single-molecule force spectroscopy: optical tweezers, magnetic tweezers and atomic force microscopy. *Nat Methods* **2008,** *5*, 491-505.

(26) Gosse, C.; Croquette, V., Magnetic tweezers: micromanipulation and force measurement at the molecular level. *Biophysical Journal* **2002,** *82*, 3314-3329.

(27) Maier, A. M.; Weig, C.; Oswald, P.; Frey, E.; Fischer, P.; Liedl, T., Magnetic Propulsion of Microswimmers with DNA-Based Flagellar Bundles. *Nano Letters* **2016,** *16*, 906-910.

(28) Ghosh, A.; Fischer, P., Controlled Propulsion of Artificial Magnetic Nanostructured Propellers. *Nano Letters* **2009,** *9*, 2243-2245.

(29) Servant, A.; Qiu, F.; Mazza, M.; Kostarelos, K.; Nelson, B. J., Controlled In Vivo Swimming of a Swarm of Bacteria-Like Microrobotic Flagella. *Advanced Materials* **2015,** *27*, 2981-2988.

(30) Zhang, L.; Abbott, J. J.; Dong, L.; Peyer, K. E.; Kratochvil, B. E.; Zhang, H.; Bergeles, C.; Nelson, B. J., Characterizing the Swimming Properties of Artificial Bacterial Flagella. *Nano Letters* **2009,** *9*, 3663-3667.

(31) Jang, B.; Gutman, E.; Stucki, N.; Seitz, B. F.; Wendel-García, P. D.; Newton, T.; Pokki, J.; Ergeneman, O.; Pané, S.; Or, Y.; Nelson, B. J., Undulatory Locomotion of Magnetic Multilink Nanoswimmers. *Nano Letters* **2015,** *15*, 4829-4833.

(32) Tierno, P.; Golestanian, R.; Pagonabarraga, I.; Sagués, F., Controlled Swimming in Confined Fluids of Magnetically Actuated Colloidal Rotors. *Physical Review Letters* **2008,** *101*, 218304.

(33) Sing, C. E.; Schmid, L.; Schneider, M. F.; Franke, T.; Alexander-Katz, A., Controlled surface-induced flows from the motion of self-assembled colloidal walkers. *Proc Natl Acad Sci U S A* **2010,** *107*, 535-40.

(34) Dholakia, K.; Reece, P.; Gu, M., Optical micromanipulation. *Chemical Society Reviews* **2008,** *37*, 42-55.

(35) Ashkin, A.; Dziedzic, J. M.; Bjorkholm, J. E.; Chu, S., Observation of a single-beam gradient force optical trap for dielectric particles. *Optics Letters* **1986,** *11*, 288-290.

(36) Svoboda, K.; Schmidt, C. F.; Schnapp, B. J.; Block, S. M., Direct observation of kinesin stepping by optical trapping interferometry. *Nature* **1993,** *365*, 721.

(37) Terray, A.; Oakey, J.; Marr, D. W. M., Microfluidic Control Using Colloidal Devices. *Science* **2002,** *296*, 1841-1844.

(38) Pauzauskie, P. J.; Radenovic, A.; Trepagnier, E.; Shroff, H.; Yang, P.; Liphardt, J., Optical trapping and integration of semiconductor nanowire assemblies in water. *Nature Materials* **2006,** *5*, 97.

(39) Higurashi, E.; Ohguchi, O.; Tamamura, T.; Ukita, H.; Sawada, R., Optically induced rotation of dissymmetrically shaped fluorinated polyimide micro-objects in optical traps. *Journal of Applied Physics* **1997,** *82*, 2773-2779.

(40) Higurashi, E.; Ukita, H.; Tanaka, H.; Ohguchi, O., Optically induced rotation of anisotropic micro-objects fabricated by surface micromachining. *Applied Physics Letters* **1994,** *64*, 2209-2210.

(41) Galajda, P.; Ormos, P., Complex micromachines produced and driven by light. *Applied Physics Letters* **2001,** *78*, 249-251.

(42) Beth, R. A., Mechanical Detection and Measurement of the Angular Momentum of Light. *Physical Review* **1936,** *50*, 115-125.

(43) Allen, L.; Beijersbergen, M. W.; Spreeuw, R. J. C.; Woerdman, J. P., Orbital angular momentum of light and the transformation of Laguerre-Gaussian laser modes. *Physical Review A* **1992,** *45*, 8185-8189.

(44) Friese, M. E. J.; Rubinsztein-Dunlop, H.; Gold, J.; Hagberg, P.; Hanstorp, D., Optically driven micromachine elements. *Applied Physics Letters* **2001,** *78*, 547-549.

(45) Friese, M. E. J.; Nieminen, T. A.; Heckenberg, N. R.; Rubinsztein-Dunlop, H., Optical alignment and spinning of laser-trapped microscopic particles. *Nature* **1998,** *394*, 348.

(46) Neale, S. L.; MacDonald, M. P.; Dholakia, K.; Krauss, T. F., All-optical control of microfluidic components using form birefringence. *Nature Materials* **2005,** *4*, 530.

(47) Grier, D. G., A revolution in optical manipulation. *Nature* **2003,** *424*, 810.

(48) O'Neil, A. T.; MacVicar, I.; Allen, L.; Padgett, M. J., Intrinsic and Extrinsic Nature of the Orbital Angular Momentum of a Light Beam. *Physical Review Letters* **2002,** *88*, 053601.

(49) Paterson, L.; MacDonald, M. P.; Arlt, J.; Sibbett, W.; Bryant, P. E.; Dholakia, K., Controlled Rotation of Optically Trapped Microscopic Particles. *Science* **2001,** *292*, 912-914.

(50) Shi, J.; Ahmed, D.; Mao, X.; Lin, S.-C. S.; Lawit, A.; Huang, T. J., Acoustic tweezers: patterning cells and microparticles using standing surface acoustic waves (SSAW). *Lab on a Chip* **2009,** *9*, 2890-2895.

(51) Ding, X.; Lin, S.-C. S.; Kiraly, B.; Yue, H.; Li, S.; Chiang, I.-K.; Shi, J.; Benkovic, S. J.; Huang, T. J., On-chip manipulation of single microparticles, cells, and organisms using surface acoustic waves. *Proceedings of the National Academy of Sciences* **2012,** *109*, 11105-11109.

(52) Guo, F.; Mao, Z.; Chen, Y.; Xie, Z.; Lata, J. P.; Li, P.; Ren, L.; Liu, J.; Yang, J.; Dao, M.; Suresh, S.; Huang, T. J., Three-dimensional manipulation of single cells using surface acoustic waves. *Proceedings of the National Academy of Sciences* **2016,** *113*, 1522-1527.

(53) Chen, Y.; Ding, X.; Steven Lin, S.-C.; Yang, S.; Huang, P.-H.; Nama, N.; Zhao, Y.; Nawaz, A. A.; Guo, F.; Wang, W.; Gu, Y.; Mallouk, T. E.; Huang, T. J., Tunable Nanowire Patterning Using Standing Surface Acoustic Waves. *ACS Nano* **2013,** *7*, 3306-3314.

(54) Wang, W.; Castro, L. A.; Hoyos, M.; Mallouk, T. E., Autonomous Motion of Metallic Microrods Propelled by Ultrasound. *ACS Nano* **2012,** *6*, 6122-6132.

(55) Garcia-Gradilla, V.; Orozco, J.; Sattayasamitsathit, S.; Soto, F.; Kuralay, F.; Pourazary, A.; Katzenberg, A.; Gao, W.; Shen, Y.; Wang, J., Functionalized Ultrasound-Propelled Magnetically Guided Nanomotors: Toward Practical Biomedical Applications. *ACS Nano* **2013,** *7*, 9232-9240.

(56) Li, J.; Li, T.; Xu, T.; Kiristi, M.; Liu, W.; Wu, Z.; Wang, J., Magneto–Acoustic Hybrid Nanomotor. *Nano Letters* **2015,** *15*, 4814-4821.

(57) Guix, M.; Mayorga-Martinez, C. C.; Merkoçi, A., Nano/Micromotors in (Bio)chemical Science Applications. *Chemical Reviews* **2014,** *114*, 6285-6322.

(58) Wang, J., Can Man-Made Nanomachines Compete with Nature Biomotors? *ACS Nano* **2009,** *3*, 4-9.

(59) Wang, W.; Duan, W.; Ahmed, S.; Mallouk, T. E.; Sen, A., Small power: Autonomous nano- and micromotors propelled by self-generated gradients. *Nano Today* **2013,** *8*, 531-554.

(60) Ma, X.; Hortelão, A. C.; Patiño, T.; Sánchez, S., Enzyme Catalysis To Power Micro/Nanomachines. *ACS Nano* **2016,** *10*, 9111-9122.

(61) Wong, F.; Sen, A., Progress toward Light-Harvesting Self-Electrophoretic Motors: Highly Efficient Bimetallic Nanomotors and Micropumps in Halogen Media. *ACS Nano* **2016,** *10*, 7172-7179.

(62) Wang, W.; Chiang, T.-Y.; Velegol, D.; Mallouk, T. E., Understanding the Efficiency of Autonomous Nano- and Microscale Motors. *Journal of the American Chemical Society* **2013,** *135*, 10557-10565.

(63) F., I. R.; Alexander, S.; Ned, B.; M., W. G., Autonomous Movement and Self-Assembly. *Angewandte Chemie International Edition* **2002,** *41*, 652-654.

(64) He, Y.; Wu, J.; Zhao, Y., Designing Catalytic Nanomotors by Dynamic Shadowing Growth. *Nano Letters* **2007,** *7*, 1369-1375.

(65) Yongfeng, M.; Gaoshan, H.; A., S. A.; Bermúdez, U. E.; Ingolf, M.; Fei, D.; Thomas, R.; Y., F. R. K.; K., C. P.; G., S. O., Versatile Approach for Integrative and Functionalized Tubes by Strain Engineering of Nanomembranes on Polymers. *Advanced Materials* **2008,** *20*, 4085-4090.

(66) Shankar, B.; Daniel, K.; Che-Ming, J. H.; Susana, C.; Jesus, L. C. M.; Nicole, L.; Y., K. D.; Maria, Z.; Liangfang, Z.; Joseph, W., Micromachine-Enabled Capture and Isolation of Cancer Cells in Complex Media. *Angewandte Chemie International Edition* **2011,** *50*, 4161-4164.

(67) Qin, L.; Banholzer, M. J.; Xu, X.; Huang, L.; Mirkin, C. A., Rational Design and Synthesis of Catalytically Driven Nanorotors. *Journal of the American Chemical Society* **2007,** *129*, 14870-14871.

(68) Baraban, L.; Makarov, D.; Streubel, R.; Mönch, I.; Grimm, D.; Sanchez, S.; Schmidt, O. G., Catalytic Janus Motors on Microfluidic Chip: Deterministic Motion for Targeted Cargo Delivery. *ACS Nano* **2012,** *6*, 3383-3389.

(69) Ren, L.; Zhou, D.; Mao, Z.; Xu, P.; Huang, T. J.; Mallouk, T. E., Rheotaxis of Bimetallic Micromotors Driven by Chemical–Acoustic Hybrid Power. *ACS Nano* **2017,** *11*, 10591-10598.

(70) Burdick, J.; Laocharoensuk, R.; Wheat, P. M.; Posner, J. D.; Wang, J., Synthetic Nanomotors in Microchannel Networks: Directional Microchip Motion and Controlled Manipulation of Cargo. *Journal of the American Chemical Society* **2008,** *130*, 8164-8165.

(71) R., K. T.; F., P. W.; E., M. T.; Ayusman, S., Catalytic Nanomotors: Remote-Controlled Autonomous Movement of Striped Metallic Nanorods. *Angewandte Chemie International Edition* **2005,** *44*, 744-746.

(72) Duan, W.; Wang, W.; Das, S.; Yadav, V.; Mallouk, T. E.; Sen, A., Synthetic Nano- and Micromachines in Analytical Chemistry: Sensing, Migration, Capture, Delivery, and Separation. *Annual Review of Analytical Chemistry* **2015,** *8*, 311-333.

(73) Gao, W.; Wang, J., The Environmental Impact of Micro/Nanomachines: A Review. *ACS Nano* **2014,** *8*, 3170-3180.

(74) Patra, D.; Sengupta, S.; Duan, W.; Zhang, H.; Pavlick, R.; Sen, A., Intelligent, self-powered, drug delivery systems. *Nanoscale* **2013,** *5*, 1273-1283.

(75) Daniel, K.; Rawiwan, L.; Maria, Z.; Corbin, C.; Shankar, B.; Dae, K.; Daniel, B.; Sirilak, S.; Liangfang, Z.; Joseph, W., Rapid Delivery of Drug Carriers Propelled and Navigated by Catalytic Nanoshuttles. *Small* **2010,** *6*, 2741-2747.

(76) Nelson, B. J.; Kaliakatsos, I. K.; Abbott, J. J., Microrobots for Minimally Invasive Medicine. *Annual Review of Biomedical Engineering* **2010,** *12*, 55-85.

(77) Wang, J.; Gao, W., Nano/Microscale Motors: Biomedical Opportunities and Challenges. *ACS Nano* **2012,** *6*, 5745-5751.

(78) Fan, D. L.; Yin, Z. Z.; Cheong, R.; Zhu, F. Q.; Cammarata, R. C.; Chien, C. L.; Levchenko, A., Subcellular-Resolution Delivery of A Cytokine Through Precisely Manipulated Nanowires. *Nature Nanotechnology* **2010,** *5*, 545-551.

(79) Soichiro, T.; Li, Z.; Famin, Q.; K., K. K.; Alfredo, F. O.; J., N. B., Magnetic Helical Micromachines: Fabrication, Controlled Swimming, and Cargo Transport. *Advanced Materials* **2012,** *24*, 811-816.

(80) Rami, M.; Famin, Q.; Li, Z.; Yun, D.; Kaori, S.; Marcy, Z. W.; J., N. B., Artificial Bacterial Flagella for Remote-Controlled Targeted Single-Cell Drug Delivery. *Small* **2014,** *10*, 1953-1957.

(81) Veronika, M.; Mariana, M. S.; Lukas, S.; Haifeng, X.; Jens, E.; G., S. O., Spermatozoa as Functional Components of Robotic Microswimmers. *Advanced Materials* **2017,** *29*, 1606301.

(82) Esteban-Fernández de Ávila, B.; Ramírez-Herrera, D. E.; Campuzano, S.; Angsantikul, P.; Zhang, L.; Wang, J., Nanomotor-Enabled pH-Responsive Intracellular Delivery of Caspase-3: Toward Rapid Cell Apoptosis. *ACS Nano* **2017,** *11*, 5367-5374.

(83) Orozco, J.; Campuzano, S.; Kagan, D.; Zhou, M.; Gao, W.; Wang, J., Dynamic Isolation and Unloading of Target Proteins by Aptamer-Modified Microtransporters. *Analytical Chemistry* **2011,** *83*, 7962-7969.

(84) Muddana, H. S.; Sengupta, S.; Mallouk, T. E.; Sen, A.; Butler, P. J., Substrate Catalysis Enhances Single-Enzyme Diffusion. *Journal of the American Chemical Society* **2010,** *132*, 2110-2111.

(85) Wu, J.; Balasubramanian, S.; Kagan, D.; Manesh, K. M.; Campuzano, S.; Wang, J., Motion-based DNA detection using catalytic nanomotors. *Nature Communications* **2010,** *1*, 36.

(86) Van Nguyen, K.; Minteer, S. D., DNA-functionalized Pt nanoparticles as catalysts for chemically powered micromotors: toward signal-on motion-based DNA biosensor. *Chemical Communications* **2015,** *51*, 4782-4784.

(87) Kagan, D.; Calvo-Marzal, P.; Balasubramanian, S.; Sattayasamitsathit, S.; Manesh, K. M.; Flechsig, G.-U.; Wang, J., Chemical Sensing Based on Catalytic Nanomotors: Motion-Based Detection of Trace Silver. *Journal of the American Chemical Society* **2009,** *131*, 12082-12083.

(88) Esteban-Fernández de Ávila, B.; Martín, A.; Soto, F.; Lopez-Ramirez, M. A.; Campuzano, S.; Vásquez-Machado, G. M.; Gao, W.; Zhang, L.; Wang, J., Single Cell Real-Time miRNAs Sensing Based on Nanomotors. *ACS Nano* **2015,** *9*, 6756-6764.

(89) Xu, X. B.; Kim, K.; Li, H. F.; Fan, D. L., Ordered Arrays of Raman Nanosensors for Ultrasensitive and Location Predictable Biochemical Detection. *Advanced Materials* **2012,** *24*, 5457-5463.

(90) Xu, X. B.; Li, H. F.; Hasan, D.; Ruoff, R. S.; Wang, A. X.; Fan, D. L., Near-Field Enhanced Plasmonic-Magnetic Bifunctional Nanotubes for Single Cell Bioanalysis. *Advanced Functional Materials* **2013,** *23*, 4332-4338.

(91) Xu, X.; Kim, K.; Liu, C.; Fan, D., Fabrication and Robotization of Ultrasensitive Plasmonic Nanosensors for Molecule Detection with Raman Scattering. *Sensors* **2015,** *15*, 10422.

(92) Kim, K.; Guo, J.; Liang, Z. X.; Zhu, F. Q.; Fan, D. L., Man-Made Rotary Nanomotors: A Review of Recent Developments. *Nanoscale* **2016,** *8*, 10471-10490.

(93) Soong, R. K.; Bachand, G. D.; Neves, H. P.; Olkhovets, A. G.; Craighead, H. G.; Montemagno, C. D., Powering an Inorganic Nanodevice with a Biomolecular Motor. *Science* **2000,** *290*, 1555-1558.

(94) Fennimore, A. M.; Yuzvinsky, T. D.; Han, W.-Q.; Fuhrer, M. S.; Cumings, J.; Zettl, A., Rotational actuators based on carbon nanotubes. *Nature* **2003,** *424*, 408.

(95) Kim, K.; Xu, X. B.; Guo, J. H.; Fan, D. L., Ultrahigh-Speed Rotating Nanoelectromechanical System Devices Assembled from Nanoscale Building Blocks. *Nature Communications* **2014,** *5*, 3632.

(96) Guo, J.; Kim, K.; Leia, K. W.; Fan, D. L., Ultra-Durable Rotary Micromotors Assembled from Nanoentities by Electric Fields. *Nanoscale* **2015,** *7*, 11363-11370.

(97) Kim, K.; Guo, J. H.; Xu, X. B.; Fan, D. L., Micromotors with Step-Motor Characteristics by Controlled Magnetic Interactions among Assembled Components. *ACS Nano* **2015,** *9*, 548-554.

(98) Ghalichechian, N.; Modafe, A.; Beyaz, M. I.; Ghodssi, R., Design, Fabrication, and Characterization of a Rotary Micromotor Supported on Microball Bearings. *Journal of Microelectromechanical Systems* **2008,** *17*, 632-642.

(99) materialoznavstra, I. p.; materialoznavstva, I. p.; Samsonov, G. V., *Handbook of the physicochemical properties of the elements*. Instituto de Fomento Industrial: 1968.

(100) Jones, T. B., *Electromechanics of Particles*. Cambridge University Press: New York, 2005.

(101) Keshoju, K.; Xing, H.; Sun, L., Magnetic field driven nanowire rotation in suspension. *Appl. Phys. Lett.* **2007,** *91*, 3.

(102) Kim, K.; Xu, X. B.; Guo, J. H.; Fan, D. L., Ultrahigh-speed rotating nanoelectromechanical system devices assembled from nanoscale building blocks. *Nat. Commun.* **2014,** *5*, 9.

(103) Coey, J. M. D., *Magnetism and Magnetic Materials*. Cambridge University Press: Dublin, 2010.

(104) Amontons, G., De La Resistance Cause'e Dans Les Machines. *Mem. Acad. R. A* **1699**, 257–282.

(105) Hertz, H., On the Contact of Elastic Solids. *J. Reine Angew. Math.* **1881,** *92*, 156.

(106) Maugis, D., ADHESION OF SPHERES - THE JKR-DMT TRANSITION USING A DUGDALE MODEL. *J. Colloid Interface Sci.* **1992,** *150*, 243-269.

(107) Gao, J. P.; Luedtke, W. D.; Gourdon, D.; Ruths, M.; Israelachvili, J. N.; Landman, U., Frictional forces and Amontons' law: From the molecular to the macroscopic scale. *J. Phys. Chem. B* **2004,** *108*, 3410-3425.

(108) Mo, Y. F.; Turner, K. T.; Szlufarska, I., Friction laws at the nanoscale. *Nature* **2009,** *457*, 1116-1119.

(109) Baker, R. G.; Palumbo, T. A., The Case for End-Point Requirements in Gold Plating Specifications for Electronic Equipment. *Plating* **1971,** *58*, 791-800.

(110) Miyoshi, K.; Buckley, D. H.; Spalvins, T.; United, S., *Friction and hardness of gold films deposited by ion plating and evaporation*. National Aeronautics and Space Administration, Scientific and Technical Information Branch ; For sale by the National Technical Information Service]: Washington, D.C. : [Springfield, Va., 1983.

(111) Liljestrand, L. G.; Sjogren, L.; Revay, L.; Asthner, B., Wear Resistance of Electroplated Nickel-Hardened Gold. *IEEE Transactions on Components, Hybrids, and Manufacturing Technology* **1985,** *8*, 123-128.

(112) Dini, J. W., *Electrodeposition: The Materials Science of Coatings and Substrates*. Noyes Publications: 1993.

(113) Nakano, H.; Tsuji, H.; Oue, S.; Fukushima, H.; Yang, F.; Tian, W., Effect of Organic Additives on the Hardness of Ni Electrodeposited from Sulfamate and Watt's Solutions. *Journal of the Japan Institute of Metals and Materials* **2011,** *75*, 406-411.

(114) Liu, C.; Wang, Z.; Li, E. W.; Liang, Z. X.; Chakravarty, S.; Xu, X. C.; Wang, A. X.; Chen, R. T.; Fan, D. L., Electrokinetic Manipulation Integrated Plasmonic Photonic Hybrid Raman Nanosensors with Dually Enhanced Sensitivity. *ACS Sensors* **2017,** *2*, 346-353.

(115) Lin, X.; Wu, Z.; Wu, Y.; Xuan, M.; He, Q., Self-Propelled Micro-/Nanomotors Based on Controlled Assembled Architectures. *Adv. Mater.* **2016,** *28*, 1060-1072.

(116) Mirkovic, T.; Zacharia, N. S.; Scholes, G. D.; Ozin, G. A., Fuel for Thought: Chemically Powered Nanomotors Out-Swim Nature's Flagellated Bacteria. *ACS Nano* **2010,** *4*, 1782-1789.

(117) Wang, H.; Zhao, G.; Pumera, M., Beyond Platinum: Bubble-Propelled Micromotors Based on Ag and MnO2 Catalysts. *J. Am. Chem. Soc.* **2014,** *136*, 2719-2722.

(118) Paxton, W. F.; Kistler, K. C.; Olmeda, C. C.; Sen, A.; St. Angelo, S. K.; Cao, Y.; Mallouk, T. E.; Lammert, P. E.; Crespi, V. H., Catalytic Nanomotors: Autonomous Movement of Striped Nanorods. *J. Am. Chem. Soc.* **2004,** *126*, 13424-13431.

(119) Wang, H.; Pumera, M., Fabrication of Micro/Nanoscale Motors. *Chem. Rev.* **2015,** *115*, 8704-8735.

(120) Demirok, U. K.; Laocharoensuk, R.; Manesh, K. M.; Wang, J., Ultrafast Catalytic Alloy Nanomotors. *Angew. Chem. Int. Ed.* **2008,** *47*, 9349-9351.

(121) Laocharoensuk, R.; Burdick, J.; Wang, J., Carbon-Nanotube-Induced Acceleration of Catalytic Nanomotors. *ACS Nano* **2008,** *2*, 1069-1075.

(122) Solovev, A. A.; Mei, Y.; Bermúdez Ureña, E.; Huang, G.; Schmidt, O. G., Catalytic Microtubular Jet Engines Self-Propelled by Accumulated Gas Bubbles. *Small* **2009,** *5*, 1688-1692.

(123) Solovev, A. A.; Xi, W.; Gracias, D. H.; Harazim, S. M.; Deneke, C.; Sanchez, S.; Schmidt, O. G., Self-Propelled Nanotools. *ACS Nano* **2012,** *6*, 1751-1756.

(124) Li, J.; Liu, W.; Wang, J.; Rozen, I.; He, S.; Chen, C.; Kim, H. G.; Lee, H.; Lee, H.; Kwon, S.; Li, T.; Li, L.; Wang, J.; Mei, Y., Nanoconfined Atomic Layer Deposition of TiO2/Pt Nanotubes: Toward Ultrasmall Highly Efficient Catalytic Nanorockets. *Adv. Funct. Mater.* **2017,** *27*, 1700598-n/a.

(125) Manjare, M.; Yang, B.; Zhao, Y. P., Bubble Driven Quasioscillatory Translational Motion of Catalytic Micromotors. *Phys. Rev. Lett.* **2012,** *109*, 128305.

(126) Dong, R.; Zhang, Q.; Gao, W.; Pei, A.; Ren, B., Highly Efficient Light-Driven TiO2–Au Janus Micromotors. *ACS Nano* **2016,** *10*, 839-844.

(127) Yoshizumi, Y.; Honegger, T.; Berton, K.; Suzuki, H.; Peyrade, D., Trajectory Control of Self-Propelled Micromotors Using AC Electrokinetics. *Small* **2015,** *11*, 5630-5635.

(128) Gao, W.; Pei, A.; Dong, R.; Wang, J., Catalytic Iridium-Based Janus Micromotors Powered by Ultralow Levels of Chemical Fuels. *J. Am. Chem. Soc.* **2014,** *136*, 2276-2279.

(129) Ma, X.; Wang, X.; Hahn, K.; Sánchez, S., Motion Control of Urea-Powered Biocompatible Hollow Microcapsules. *ACS Nano* **2016,** *10*, 3597-3605.

(130) Dey, K. K.; Zhao, X.; Tansi, B. M.; Méndez-Ortiz, W. J.; Córdova-Figueroa, U. M.; Golestanian, R.; Sen, A., Micromotors Powered by Enzyme Catalysis. *Nano Lett.* **2015,** *15*, 8311-8315.

(131) Jang, B.; Hong, A.; Kang, H. E.; Alcantara, C.; Charreyron, S.; Mushtaq, F.; Pellicer, E.; Büchel, R.; Sort, J.; Lee, S. S.; Nelson, B. J.; Pané, S., Multiwavelength Light-Responsive Au/B-TiO2 Janus Micromotors. *ACS Nano* **2017,** *11*, 6146-6154.

(132) Peng, F.; Tu, Y.; van Hest, J. C. M.; Wilson, D. A., Self-Guided Supramolecular Cargo-Loaded Nanomotors with Chemotactic Behavior towards Cells. *Angew. Chem. Int. Ed.* **2015,** *54*, 11662-11665.

(133) Mou, F.; Chen, C.; Zhong, Q.; Yin, Y.; Ma, H.; Guan, J., Autonomous Motion and Temperature-Controlled Drug Delivery of Mg/Pt-Poly(N-isopropylacrylamide) Janus Micromotors Driven by Simulated Body Fluid and Blood Plasma. *ACS Appl. Mater. Interfaces* **2014,** *6*, 9897-9903.

(134) Li, J.; Shklyaev, O. E.; Li, T.; Liu, W.; Shum, H.; Rozen, I.; Balazs, A. C.; Wang, J., Self-Propelled Nanomotors Autonomously Seek and Repair Cracks. *Nano Lett.* **2015,** *15*, 7077-7085.

(135) Li, J.; Gao, W.; Dong, R.; Pei, A.; Sattayasamitsathit, S.; Wang, J., Nanomotor Lithography. *Nat. Commun.* **2014,** *5*, 5026.

(136) Gao, W.; Dong, R.; Thamphiwatana, S.; Li, J.; Gao, W.; Zhang, L.; Wang, J., Artificial Micromotors in the Mouse's Stomach: A Step toward in Vivo Use of Synthetic Motors. *ACS Nano* **2015,** *9*, 117-123.

(137) Xu, T.; Soto, F.; Gao, W.; Dong, R.; Garcia-Gradilla, V.; Magana, E.; Zhang, X.; Wang, J., Reversible Swarming and Separation of Self-Propelled Chemically Powered Nanomotors under Acoustic Fields. *J. Am. Chem. Soc.* **2015,** *137*, 2163-2166.

(138) Balasubramanian, S.; Kagan, D.; Manesh, K. M.; Calvo-Marzal, P.; Flechsig, G.-U.; Wang, J., Thermal Modulation of Nanomotor Movement. *Small* **2009,** *5*, 1569-1574.

(139) Solovev, A. A.; Smith, E. J.; Bufon, C. C. B.; Sanchez, S.; Schmidt, O. G., Light-Controlled Propulsion of Catalytic Microengines. *Angew. Chem. Int. Ed.* **2011,** *50*, 10875-10878.

(140) Ibele, M.; Mallouk, T. E.; Sen, A., Schooling Behavior of Light-Powered Autonomous Micromotors in Water. *Angew. Chem. Int. Ed.* **2009,** *48*, 3308-3312.

(141) Moo, J. G. S.; Presolski, S.; Pumera, M., Photochromic Spatiotemporal Control of Bubble-Propelled Micromotors by a Spiropyran Molecular Switch. *ACS Nano* **2016,** *10*, 3543-3552.

(142) Calvo-Marzal, P.; Manesh, K. M.; Kagan, D.; Balasubramanian, S.; Cardona, M.; Flechsig, G.-U.; Posner, J.; Wang, J., Electrochemically-Triggered Motion of Catalytic Nanomotors. *Chem. Commun.* **2009**, 4509-4511.

(143) Wang, W.; Duan, W.; Zhang, Z.; Sun, M.; Sen, A.; Mallouk, T. E., A Tale of Two Forces: Simultaneous Chemical and Acoustic Propulsion of Bimetallic Micromotors. *Chem. Commun.* **2015,** *51*, 1020-1023.

(144) Chien, C. L.; Fan, D.; Cammarata, R. C. System and Method for Precision Transport, Positioning, and Assembling of Longitudinal Nano-structures. Patent:9,044,808 B2, 2015.

(145) Guo, J.; Gallegos, J. J.; Tom, A. R.; Fan, D., Electric-Field-Guided Precision Manipulation of Catalytic Nanomotors for Cargo Delivery and Powering Nanoelectromechanical Devices. *ACS Nano* **2018,** *12*, 1179-1187.

(146) Whitney, T. M.; Jiang, J. S.; Searson, P. C.; Chien, C. L., Fabrication And Magnetic Properties of Arrays of Metallic Nanowires. *Science* **1993,** *261*, 1316-1319.

(147) Kim, K.; Xu, X.; Guo, J.; Fan, D. L., Ultrahigh-Speed Rotating Nanoelectromechanical System Devices Assembled from Nanoscale Building Blocks. *Nat. Commun.* **2014,** *5*, 3632.

(148) *Hydrogen Peroxide Physical Properties Data Book*. Becco Chemical Division: 1955.

(149) Paxton, W. F.; Baker, P. T.; Kline, T. R.; Wang, Y.; Mallouk, T. E.; Sen, A., Catalytically Induced Electrokinetics for Motors and Micropumps. *J. Am. Chem. Soc.* **2006,** *128*, 14881-14888.

(150) Paxton, W. F.; Sen, A.; Mallouk, T. E., Motility of Catalytic Nanoparticles through Self-Generated Forces. *Chem. Eur. J.* **2005,** *11*, 6462-6470.

(151) Liu, R.; Sen, A., Autonomous Nanomotor Based on Copper–Platinum Segmented Nanobattery. *J. Am. Chem. Soc.* **2011,** *133*, 20064-20067.

(152) Wang, H.; Moo, J. G. S.; Pumera, M., From Nanomotors to Micromotors: The Influence of the Size of an Autonomous Bubble-Propelled Device upon Its Motion. *ACS Nano* **2016,** *10*, 5041-5050.

(153) Lee, T.-C.; Alarcón-Correa, M.; Miksch, C.; Hahn, K.; Gibbs, J. G.; Fischer, P., Self-Propelling Nanomotors in the Presence of Strong Brownian Forces. *Nano Lett.* **2014,** *14*, 2407-2412.

(154) Fan, D.; Yin, Z.; Cheong, R.; Zhu, F. Q.; Cammarata, R. C.; Chien, C. L.; Levchenko, A., Subcellular-Resolution Delivery of A Cytokine Through Precisely Manipulated Nanowires. *Nat. Nanotechnol.* **2010,** *5*, 545.

(155) Das, S.; Garg, A.; Campbell, A. I.; Howse, J.; Sen, A.; Velegol, D.; Golestanian, R.; Ebbens, S. J., Boundaries can steer active Janus spheres. *Nature Communications* **2015,** *6*, 8999.

(156) Kirby, B. J.; Hasselbrink, E. F., Zeta potential of microfluidic substrates: 1. Theory, experimental techniques, and effects on separations. *Electrophoresis* **2004,** *25*, 187-202.

(157) Baker, D. R., *Capillary Electrophoresis*. John Wiley & Sons, Inc.: 1995.

(158) Barz, D. P. J.; Vogel, M. J.; Steen, P. H., Determination of the Zeta Potential of Porous Substrates by Droplet Deflection. I. The Influence of Ionic Strength and pH Value of an Aqueous Electrolyte in Contact with a Borosilicate Surface. *Langmuir* **2009,** *25*, 1842-1850.

(159) Kline, T. R.; Paxton, W. F.; Wang, Y.; Velegol, D.; Mallouk, T. E.; Sen, A., Catalytic Micropumps: Microscopic Convective Fluid Flow and Pattern Formation. *J. Am. Chem. Soc.* **2005,** *127*, 17150-17151.

(160) Esplandiu, M. J.; Afshar Farniya, A.; Bachtold, A., Silicon-Based Chemical Motors: An Efficient Pump for Triggering and Guiding Fluid Motion Using Visible Light. *ACS Nano* **2015,** *9*, 11234-11240.

(161) Guo, J.; Kim, K.; Lei, K. W.; Fan, D. L., Ultra-Durable Rotary Micromotors Assembled from Nanoentities by Electric Fields. *Nanoscale* **2015,** *7*, 11363-11370.

(162) Kim, K.; Guo, J.; Xu, X.; Fan, D., Micromotors with Step-Motor Characteristics by Controlled Magnetic Interactions among Assembled Components. *ACS Nano* **2015,** *9*, 548-554.

(163) Timko, B. P.; Dvir, T.; Kohane, D. S., Remotely Triggerable Drug Delivery Systems. *Adv. Mater.* **2010,** *22*, 4925-4943.

(164) Mura, S.; Nicolas, J.; Couvreur, P., Stimuli-responsive nanocarriers for drug delivery. *Nat. Mater.* **2013,** *12*, 991-1003.

(165) Stuart, M. A. C.; Huck, W. T. S.; Genzer, J.; Muller, M.; Ober, C.; Stamm, M.; Sukhorukov, G. B.; Szleifer, I.; Tsukruk, V. V.; Urban, M.; Winnik, F.; Zauscher, S.;

Luzinov, I.; Minko, S., Emerging applications of stimuli-responsive polymer materials. *Nat. Mater.* **2010,** *9*, 101-113.

(166) Salem, A. K.; Searson, P. C.; Leong, K. W., Multifunctional Nanorods for Gene Delivery. *Nat. Mater.* **2003,** *2*, 668-671.

(167) Kagan, D.; Laocharoensuk, R.; Zimmerman, M.; Clawson, C.; Balasubramanian, S.; Kang, D.; Bishop, D.; Sattayasamitsathit, S.; Zhang, L.; Wang, J., Rapid Delivery of Drug Carriers Propelled and Navigated by Catalytic Nanoshuttles. *Small* **2010,** *6*, 2741-2747.

(168) Xu, X.; Hou, S.; Wattanatorn, N.; Wang, F.; Yang, Q.; Zhao, C.; Yu, X.; Tseng, H.-R.; Jonas, S. J.; Weiss, P. S., Precision-Guided Nanospears for Targeted and High-Throughput Intracellular Gene Delivery. *ACS Nano* **2018**.

(169) Yavuz, M. S.; Cheng, Y.; Chen, J.; Cobley, C. M.; Zhang, Q.; Rycenga, M.; Xie, J.; Kim, C.; Song, K. H.; Schwartz, A. G.; Wang, L. V.; Xia, Y., Gold Nanocages Covered by Smart Polymers for Controlled Release with Near-Infrared Light. *Nat. Mater.* **2009,** *8*, 935.

(170) Lee, S. E.; Liu, G. L.; Kim, F.; Lee, L. P., Remote Optical Switch for Localized and Selective Control of Gene Interference. *Nano Lett.* **2009,** *9*, 562-570.

(171) Goodman, A. M.; Hogan, N. J.; Gottheim, S.; Li, C.; Clare, S. E.; Halas, N. J., Understanding Resonant Light-Triggered DNA Release from Plasmonic Nanoparticles. *ACS Nano* **2017,** *11*, 171-179.

(172) Cao, Z. Y.; Ma, Y. C.; Sun, C. Y.; Lu, Z. D.; Yao, Z. Y.; Wang, J. X.; Li, D. D.; Yuan, Y. Y.; Yang, X. Z., ROS-Sensitive Polymeric Nanocarriers with Red Light-Activated Size Shrinkage for Remotely Controlled Drug Release. *Chem. Mater.* **2018,** *30*, 517-525.

(173) Cao, S. P.; Pei, Z. C.; Xu, Y. Q.; Pei, Y. X., Glyco-Nanovesicles with Activatable Near-Infrared Probes for Real-Time Monitoring of Drug Release and Targeted Delivery. *Chem. Mater.* **2016,** *28*, 4501-4506.

(174) Qin, J.; Asempah, I.; Laurent, S.; Fornara, A.; Muller, R. N.; Muhammed, M., Injectable Superparamagnetic Ferrogels for Controlled Release of Hydrophobic Drugs. *Adv. Mater.* **2009,** *21*, 1354-1357.

(175) Ruiz-Hernández, E.; Baeza, A.; Vallet-Regí, M., Smart Drug Delivery through DNA/Magnetic Nanoparticle Gates. *ACS Nano* **2011,** *5*, 1259-1266.

(176) Mali, P.; Bhattacharjee, N.; Searson, P. C., Electrochemically Programmed Release of Biomolecules and Nanoparticles. *Nano Lett.* **2006,** *6*, 1250-1253.

(177) Hernot, S.; Klibanov, A. L., Microbubbles in Ultrasound-Triggered Drug and Gene Delivery. *Adv. Drug Deliv. Rev.* **2008,** *60*, 1153-1166.

(178) Javadi, M.; Pitt, W. G.; Belnap, D. M.; Tsosie, N. H.; Hartley, J. M., Encapsulating Nanoemulsions Inside eLiposomes for Ultrasonic Drug Delivery. *Langmuir* **2012,** *28*, 14720-14729.

(179) Fu, J.; Wang, Y.-K.; Yang, M. T.; Desai, R. A.; Yu, X.; Liu, Z.; Chen, C. S., Mechanical Regulation of Cell Function with Geometrically Modulated Elastomeric Substrates. *Nature Methods* **2010,** *7*, 733.

(180) Shao, Y.; Fu, J. P., Integrated Micro/Nanoengineered Functional Biomaterials for Cell Mechanics and Mechanobiology: A Materials Perspective. *Adv. Mater.* **2014,** *26*, 1494-1533.

(181) Levchenko, A.; Nemenman, I., Cellular Noise and Information Transmission. *Curr. Opin. Biotechnol.* **2014,** *28*, 156-164.

(182) Chen, W.; Villa-Diaz, L. G.; Sun, Y.; Weng, S.; Kim, J. K.; Lam, R. H. W.; Han, L.; Fan, R.; Krebsbach, P. H.; Fu, J., Nanotopography Influences Adhesion,

Spreading, and Self-Renewal of Human Embryonic Stem Cells. *ACS Nano* **2012,** *6*, 4094-4103.

(183) Lu, Y.; Xue, Q.; Eisele, M. R.; Sulistijo, E. S.; Brower, K.; Han, L.; Amir, E.-a. D.; Pe'er, D.; Miller-Jensen, K.; Fan, R., Highly Multiplexed Profiling of Single-Cell Effector Functions Reveals Deep Functional Heterogeneity in Response to Pathogenic Ligands. *Proc. Natl. Acad. Sci. U.S.A.* **2015,** *112*, E607-E615.

(184) Wang, Y.; Yan, B.; Chen, L., SERS Tags: Novel Optical Nanoprobes for Bioanalysis. *Chem. Rev.* **2013,** *113*, 1391-1428.

(185) Abramczyk, H.; Brozek-Pluska, B., Raman Imaging in Biochemical and Biomedical Applications. Diagnosis and Treatment of Breast Cancer. *Chem. Rev.* **2013,** *113*, 5766-5781.

(186) Bailo, E.; Deckert, V., Tip-Enhanced Raman Scattering. *Chem. Soc. Rev.* **2008,** *37*, 921-930.

(187) Zhang, Y.; Zhen, Y.-R.; Neumann, O.; Day, J. K.; Nordlander, P.; Halas, N. J., Coherent Anti-Stokes Raman Scattering with Single-Molecule Sensitivity Using a Plasmonic Fano Resonance. *Nat. Commun.* **2014,** *5*, 4424.

(188) Tang, H.; Meng, G.; Huang, Q.; Zhang, Z.; Huang, Z.; Zhu, C., Arrays of Cone-Shaped ZnO Nanorods Decorated with Ag Nanoparticles as 3D Surface-Enhanced Raman Scattering Substrates for Rapid Detection of Trace Polychlorinated Biphenyls. *Adv. Funct. Mater.* **2012,** *22*, 218-224.

(189) Baumberg, J. J.; Kelf, T. A.; Sugawara, Y.; Cintra, S.; Abdelsalam, M. E.; Bartlett, P. N.; Russell, A. E., Angle-Resolved Surface-Enhanced Raman Scattering on Metallic Nanostructured Plasmonic Crystals. *Nano Lett.* **2005,** *5*, 2262-2267.

(190) Fang, Y.; Seong, N.-H.; Dlott, D. D., Measurement of the Distribution of Site Enhancements in Surface-Enhanced Raman Scattering. *Science* **2008,** *321*, 388-392.

(191) Rycenga, M.; Xia, X.; Moran, C. H.; Zhou, F.; Qin, D.; Li, Z.-Y.; Xia, Y., Generation of Hot Spots with Silver Nanocubes for Single-Molecule Detection by Surface-Enhanced Raman Scattering. *Angew. Chem. Int. Ed.* **2011,** *50*, 5473-5477.

(192) Thacker, V. V.; Herrmann, L. O.; Sigle, D. O.; Zhang, T.; Liedl, T.; Baumberg, J. J.; Keyser, U. F., DNA Origami Based Assembly of Gold Nanoparticle Dimers for Surface-Enhanced Raman Scattering. *Nat. Commun.* **2014,** *5*, 3448.

(193) Li, W. Y.; Camargo, P. H. C.; Lu, X. M.; Xia, Y. N., Dimers of Silver Nanospheres: Facile Synthesis and Their Use as Hot Spots for Surface-Enhanced Raman Scattering. *Nano Lett.* **2009,** *9*, 485-490.

(194) Lu, Y.; Liu, G. L.; Lee, L. P., High-Density Silver Nanoparticle Film with Temperature-Controllable Interparticle Spacing for A Tunable Surface Enhanced Raman Scattering Substrate. *Nano Lett.* **2005,** *5*, 5-9.

(195) Liu, J.; Meng, G. W.; Li, Z. B.; Huang, Z. L.; Li, X. D., Ag-NP@Ge-Nanotaper/Si-Micropillar Ordered Arrays As Ultrasensitive and Uniform Surface Enhanced Raman Scattering Substrates. *Nanoscale* **2015,** *7*, 18218-18224.

(196) Lu, X. F.; Huang, Y. J.; Liu, B. Q.; Zhang, L.; Song, L. P.; Zhang, J. W.; Zhang, A. F.; Chen, T., Light-Controlled Shrinkage of Large-Area Gold Nanoparticle Monolayer Film for Tunable SERS Activity. *Chem. Mater.* **2018,** *30*, 1989-1997.

(197) Tian, L.; Tadepalli, S.; Fei, M.; Morrissey, J. J.; Kharasch, E. D.; Singamaneni, S., Off-Resonant Gold Superstructures as Ultrabright Minimally Invasive Surface-Enhanced Raman Scattering (SERS) Probes. *Chem. Mater.* **2015,** *27*, 5678-5684.

(198) Huang, Z.; Meng, G.; Huang, Q.; Yang, Y.; Zhu, C.; Tang, C., Improved SERS Performance from Au Nanopillar Arrays by Abridging the Pillar Tip Spacing by Ag Sputtering. *Adv. Mater.* **2010,** *22*, 4136-4139.

(199) Zhu, C. H.; Meng, G. W.; Zheng, P.; Huang, Q.; Li, Z. B.; Hu, X. Y.; Wang, X. J.; Huang, Z. L.; Li, F. D.; Wu, N. Q., A Hierarchically Ordered Array of Silver-Nanorod Bundles for Surface-Enhanced Raman Scattering Detection of Phenolic Pollutants. *Adv. Mater.* **2016,** *28*, 4871-4876.

(200) Scarabelli, L.; Hamon, C.; Liz-Marzan, L. M., Design and Fabrication of Plasmonic Nanomaterials Based on Gold Nanorod Supercrystals. *Chem. Mater.* **2017,** *29*, 15-25.

(201) Yang, M.; Alvarez-Puebla, R.; Kim, H.-S.; Aldeanueva-Potel, P.; Liz-Marzán, L. M.; Kotov, N. A., SERS-Active Gold Lace Nanoshells with Built-in Hotspots. *Nano Lett.* **2010,** *10*, 4013-4019.

(202) Liu, K. K.; Tadepalli, S.; Tian, L. M.; Singamaneni, S., Size-Dependent Surface Enhanced Raman Scattering Activity of Plasmonic Nanorattles. *Chem. Mater.* **2015,** *27*, 5261-5270.

(203) Niu, W.; Chua, Y. A. A.; Zhang, W.; Huang, H.; Lu, X., Highly Symmetric Gold Nanostars: Crystallographic Control and Surface-Enhanced Raman Scattering Property. *J. Am. Chem. Soc.* **2015,** *137*, 10460-10463.

(204) de Aberasturi, D. J.; Serrano-Montes, A. B.; Langer, J.; Henriksen-Lacey, M.; Parak, W. J.; Liz-Marzan, L. M., Surface Enhanced Raman Scattering Encoded Gold Nanostars for Multiplexed Cell Discrimination. *Chem. Mater.* **2016,** *28*, 6779-6790.

(205) Blackie, E. J.; Ru, E. C. L.; Etchegoin, P. G., Single-Molecule Surface-Enhanced Raman Spectroscopy of Nonresonant Molecules. *J. Am. Chem. Soc.* **2009,** *131*, 14466-14472.

(206) Kleinman, S. L.; Ringe, E.; Valley, N.; Wustholz, K. L.; Phillips, E.; Scheidt, K. A.; Schatz, G. C.; Van Duyne, R. P., Single-Molecule Surface-Enhanced

Raman Spectroscopy of Crystal Violet Isotopologues: Theory and Experiment. *J. Am. Chem. Soc.* **2011,** *133*, 4115-4122.

(207) Chourpa, I.; Lei, F. H.; Dubois, P.; Manfait, M.; Sockalingum, G. D., Intracellular Applications of Analytical SERS Spectroscopy and Multispectral Imaging. *Chem. Soc. Rev.* **2008,** *37*, 993-1000.

(208) Song, J.; Zhou, J.; Duan, H., Self-Assembled Plasmonic Vesicles of SERS-Encoded Amphiphilic Gold Nanoparticles for Cancer Cell Targeting and Traceable Intracellular Drug Delivery. *J. Am. Chem. Soc.* **2012,** *134*, 13458-13469.

(209) Du, J.; Zhu, B.; Chen, X., Urine for Plasmonic Nanoparticle-Based Colorimetric Detection of Mercury Ion. *Small* **2013,** *9*, 4104-4111.

(210) Du, J.; Zhu, B.; Leow, W. R.; Chen, S.; Sum, T. C.; Peng, X.; Chen, X., Colorimetric Detection of Creatinine Based on Plasmonic Nanoparticles via Synergistic Coordination Chemistry. *Small* **2015,** *11*, 4104-4110.

(211) Xu, X. B.; Kim, K.; Fan, D. L., Tunable Release of Multiplex Biochemicals by Plasmonically Active Rotary Nanomotors. *Angewandte Chemie International Edition* **2015,** *54*, 2525-2529.

(212) Whitney, T. M.; Searson, P. C.; Jiang, J. S.; Chien, C. L., Fabrication and Magnetic Properties of Arrays of Metallic Nanowires. *Science* **1993,** *261*, 1316-1319.

(213) Hu, M.; Ou, F. S.; Wu, W.; Naumov, I.; Li, X.; Bratkovsky, A. M.; Williams, R. S.; Li, Z., Gold Nanofingers for Molecule Trapping and Detection. *J. Am. Chem. Soc.* **2010,** *132*, 12820-12822.

(214) Schmidt, M. S.; Hübner, J.; Boisen, A., Large Area Fabrication of Leaning Silicon Nanopillars for Surface Enhanced Raman Spectroscopy. *Adv. Mater.* **2012,** *24*, OP11-OP18.

(215) Barhoumi, A.; Halas, N. J., Label-Free Detection of DNA Hybridization Using Surface Enhanced Raman Spectroscopy. *J. Am. Chem. Soc.* **2010,** *132*, 12792-12793.

(216) Wei, Q. H.; Su, K. H.; Durant, S.; Zhang, X., Plasmon Resonance of Finite One-Dimensional Au Nanoparticle Chains. *Nano Lett.* **2004,** *4*, 1067-1071.

(217) Miller, K. J., Additivity Methods in Molecular Polarizability. *J. Am. Chem. Soc.* **1990,** *112*, 8533-8542.

(218) Myslinski, P.; Wieczorek, D., Differential Anisotropy of Polarizability Measured by Picosecond Transient Dichroism and Birefringence. *J. Chem. Phys.* **1990,** *92*, 969-977.

(219) A. J. Brad; Faulkner, L. R., *Electrochemical Methods*. Wiley: New York, 1980.

(220) Chien, C. L.; Fan, D. L.; Cammarata, R. C. System and Method for Precision transport, Positioning, and Assembling of Longitudinal Nano-structures Patent:2017.

(221) Xiang-Zhong, C.; Marcus, H.; Naveen, S.; Tianyun, H.; Berna, Ö.; Qian, L.; Erdem, S.; Fajer, M.; Luca, D. T.; J., N. B.; Salvador, P., Hybrid Magnetoelectric Nanowires for Nanorobotic Applications: Fabrication, Magnetoelectric Coupling, and Magnetically Assisted In Vitro Targeted Drug Delivery. *Adv. Mater.* **2017,** *29*, 1605458.

(222) Han, D.; Fang, Y.; Du, D.; Huang, G.; Qiu, T.; Mei, Y., Automatic molecular collection and detection by using fuel-powered microengines. *Nanoscale* **2016,** *8*, 9141-9145.

(223) Liu, C.; Wang, Z.; Li, E.; Liang, Z.; Chakravarty, S.; Xu, X.; Wang, A. X.; Chen, R. T.; Fan, D., Electrokinetic Manipulation Integrated Plasmonic–Photonic Hybrid Raman Nanosensors with Dually Enhanced Sensitivity. *ACS Sens.* **2017,** *2*, 346-353.

(224) Metzker, M. L., APPLICATIONS OF NEXT-GENERATION SEQUENCING Sequencing technologies - the next generation. *Nat. Rev. Genet.* **2010,** *11*, 31-46.

(225) Kutzler, M. A.; Weiner, D. B., DNA vaccines: ready for prime time? *Nat. Rev. Genet.* **2008,** *9*, 776-788.

(226) Jobling, M. A.; Gill, P., Encoded evidence: DNA in forensic analysis. *Nat. Rev. Genet.* **2004,** *5*, 739-751.

(227) Thomas, C. E.; Ehrhardt, A.; Kay, M. A., Progress and problems with the use of viral vectors for gene therapy. *Nat. Rev. Genet.* **2003,** *4*, 346-358.

(228) Burns, M. A.; Johnson, B. N.; Brahmasandra, S. N.; Handique, K.; Webster, J. R.; Krishnan, M.; Sammarco, T. S.; Man, P. M.; Jones, D.; Heldsinger, D.; Mastrangelo, C. H.; Burke, D. T., An Integrated Nanoliter DNA Analysis Device. *Science* **1998,** *282*, 484-487.

(229) Easley, C. J.; Karlinsey, J. M.; Bienvenue, J. M.; Legendre, L. A.; Roper, M. G.; Feldman, S. H.; Hughes, M. A.; Hewlett, E. L.; Merkel, T. J.; Ferrance, J. P.; Landers, J. P., A fully integrated microfluidic genetic analysis system with sample-in-answer-out capability. *Proc. Natl. Acad. Sci. U. S. A.* **2006,** *103*, 19272-19277.

(230) Breadmore, M. C.; Wolfe, K. A.; Arcibal, I. G.; Leung, W. K.; Dickson, D.; Giordano, B. C.; Power, M. E.; Ferrance, J. P.; Feldman, S. H.; Norris, P. M.; Landers, J. P., Microchip-based purification of DNA from biological samples. *Anal. Chem.* **2003,** *75*, 1880-1886.

(231) Price, C. W.; Leslie, D. C.; Landers, J. P., Nucleic acid extraction techniques and application to the microchip. *Lab Chip* **2009,** *9*, 2484-2494.

(232) Ulrike, L.; Caroline, V.; K., P. V.; M., G. M. A., Droplet-Based DNA Purification in a Magnetic Lab-on-a-Chip. *Angewandte Chemie International Edition* **2006,** *45*, 3062-3067.

(233) Hartono, S. B.; Gu, W. Y.; Kleitz, F.; Liu, J.; He, L. Z.; Middelberg, A. P. J.; Yu, C. Z.; Lu, G. Q.; Qiao, S. Z., Poly-L-lysine Functionalized Large Pore Cubic Mesostructured Silica Nanoparticles as Biocompatible Carriers for Gene Delivery. *ACS Nano* **2012,** *6*, 2104-2117.

(234) Zhang, Y.; Zhang, Y.; Burke, J. M.; Gleitsman, K.; Friedrich, S. M.; Liu, K. J.; Wang, T. H., A Simple Thermoplastic Substrate Containing Hierarchical Silica Lamellae for High-Molecular-Weight DNA Extraction. *Adv. Mater.* **2016,** *28*, 10630-+.

(235) Johnson, P. A.; Gaspar, M. A.; Levicky, R., Polymer-anchored DNA gene monolayers. *J. Am. Chem. Soc.* **2004,** *126*, 9910-9911.

(236) Gaylord, B. S.; Heeger, A. J.; Bazan, G. C., DNA Hybridization Detection with Water-Soluble Conjugated Polymers and Chromophore-Labeled Single-Stranded DNA. *J. Am. Chem. Soc.* **2003,** *125*, 896-900.

(237) Liu, B. W.; Ma, L. Z.; Huang, Z. C.; Hu, H.; Wu, P.; Liu, J. W., Janus DNA orthogonal adsorption of graphene oxide and metal oxide nanoparticles enabling stable sensing in serum. *Mater. Horizons* **2018,** *5*, 65-69.

(238) Vigderman, L.; Zubarev, E. R., Therapeutic platforms based on gold nanoparticles and their covalent conjugates with drug molecules. *Advanced Drug Delivery Reviews* **2013,** *65*, 663-676.

(239) Li, H. X.; Rothberg, L., Colorimetric detection of DNA sequences based on electrostatic interactions with unmodified gold nanoparticles. *Proc. Natl. Acad. Sci. U. S. A.* **2004,** *101*, 14036-14039.

(240) Sapsford, K. E.; Algar, W. R.; Berti, L.; Gemmill, K. B.; Casey, B. J.; Oh, E.; Stewart, M. H.; Medintz, I. L., Functionalizing Nanoparticles with Biological Molecules: Developing Chemistries that Facilitate Nanotechnology. *Chemical Reviews* **2013,** *113*, 1904-2074.

(241) Park, J.-H.; Gu, L.; von Maltzahn, G.; Ruoslahti, E.; Bhatia, S. N.; Sailor, M. J., Biodegradable luminescent porous silicon nanoparticles for in vivo applications. *Nature Materials* **2009,** *8*, 331.

(242) Xia, T.; Kovochich, M.; Liong, M.; Meng, H.; Kabehie, S.; George, S.; Zink, J. I.; Nel, A. E., Polyethyleneimine Coating Enhances the Cellular Uptake of Mesoporous Silica Nanoparticles and Allows Safe Delivery of siRNA and DNA Constructs. *ACS Nano* **2009,** *3*, 3273-3286.

(243) Melzak, K. A.; Sherwood, C. S.; Turner, R. F. B.; Haynes, C. A., Driving forces for DNA adsorption to silica in perchlorate solutions. *J. Colloid Interface Sci.* **1996,** *181*, 635-644.

(244) Smeets, R. M. M.; Keyser, U. F.; Krapf, D.; Wu, M.-Y.; Dekker, N. H.; Dekker, C., Salt Dependence of Ion Transport and DNA Translocation through Solid-State Nanopores. *Nano Letters* **2006,** *6*, 89-95.

(245) Vandeventer, P. E.; Lin, J. S.; Zwang, T. J.; Nadim, A.; Johal, M. S.; Niemz, A., Multiphasic DNA Adsorption to Silica Surfaces under Varying Buffer, pH, and Ionic Strength Conditions. *The Journal of Physical Chemistry B* **2012,** *116*, 5661-5670.

(246) Huang, F. J.; Liang, H. J., Adsorption Behaviors of DNA/Cation Complexes on Amino and Silica Chip Surfaces: A Dual Polarization Interferometry Study. *ACS Appl. Mater. Interfaces* **2013,** *5*, 5025-5033.

(247) Squires, T. M.; Messinger, R. J.; Manalis, S. R., Making it stick: convection, reaction and diffusion in surface-based biosensors. *Nature Biotechnology* **2008,** *26*, 417.

(248) K.H., S.; M.B., D.; P.M., H.; M.A., C.; J.D., C.; T.A., B.; T.J., H.; W.R., O.; M.E.A., S., Novel, Bioclastic Route to Self-Assembled, 3D, Chemically Tailored Meso/Nanostructures: Shape-Preserving Reactive Conversion of Biosilica (Diatom) Microshells. *Adv. Mater.* **2002,** *14*, 429-433.

(249) Bao, Z.; Weatherspoon, M. R.; Shian, S.; Cai, Y.; Graham, P. D.; Allan, S. M.; Ahmad, G.; Dickerson, M. B.; Church, B. C.; Kang, Z.; Abernathy Iii, H. W.; Summers, C. J.; Liu, M.; Sandhage, K. H., Chemical reduction of three-dimensional silica micro-assemblies into microporous silicon replicas. *Nature* **2007,** *446*, 172.

(250) Clayton, J.; Raj, S.; Yaswanth, R.; Wei, W.; Chih-hung, C.; L., R. G., Electroluminescence and Photoluminescence from Nanostructured Diatom Frustules Containing Metabolically Inserted Germanium. *Adv. Mater.* **2008,** *20*, 2633-2637.

(251) Ren, F.; Campbell, J.; Wang, X.; Rorrer, G. L.; Wang, A. X., Enhancing surface plasmon resonances of metallic nanoparticles by diatom biosilica. *Opt. Express* **2013,** *21*, 15308-15313.

(252) Kim, K.; Lang, Z. X.; Liu, M. L.; Fan, D. L., Biobased High-Performance Rotary Micromotors for Individually Reconfigurable Micromachine Arrays and Microfluidic Applications. *ACS Applied Materials & Interfaces* **2017,** *9*, 6144-6152.

(253) Liu, J.; Wang, B.; Budi Hartono, S.; Liu, T.; Kantharidis, P.; Middelberg, A. P. J.; Lu, G. Q.; He, L.; Qiao, S. Z., Magnetic silica spheres with large nanopores for nucleic acid adsorption and cellular uptake. *Biomaterials* **2012,** *33*, 970-978.

(254) Li, X.; Zhang, J.; Gu, H., Adsorption and Desorption Behaviors of DNA with Magnetic Mesoporous Silica Nanoparticles. *Langmuir* **2011,** *27*, 6099-6106.

(255) Lee, G. J.; Kwon, Y.-W.; Kim, Y. H.; Choi, E. H., Raman spectroscopic study of plasma-treated salmon DNA. *Applied Physics Letters* **2013,** *102*, 021911.

(256) Xu, L.-J.; Lei, Z.-C.; Li, J.; Zong, C.; Yang, C. J.; Ren, B., Label-Free Surface-Enhanced Raman Spectroscopy Detection of DNA with Single-Base Sensitivity. *Journal of the American Chemical Society* **2015,** *137*, 5149-5154.

(257) Keshoju, K.; Xing, H.; Sun, L., Magnetic field driven nanowire rotation in suspension. *Applied Physics Letters* **2007,** *91*, 123114.

(258) Aragones, J. L.; Steimel, J. P.; Alexander-Katz, A., Elasticity-induced force reversal between active spinning particles in dense passive media. *Nature Communications* **2016,** *7*, 11325.

(259) Ma, L.-C.; Subramanian, R.; Huang, H.-W.; Ray, V.; Kim, C.-U.; Koh, S. J., Electrostatic Funneling for Precise Nanoparticle Placement: A Route to Wafer-Scale Integration. *Nano Letters* **2007,** *7*, 439-445.

(260) Ni, S.; Leemann, J.; Buttinoni, I.; Isa, L.; Wolf, H., Programmable colloidal molecules from sequential capillarity-assisted particle assembly. *Science Advances* **2016,** *2*.

(261) Masel, R. I., *Principles of adsorption and reaction on solid surfaces*. Wiley: 1996.

(262) Bard, A. J.; Faulkner, L. R., *Electrochemical methods: fundamentals and applications*. Wiley: 1980.

(263) Hu, Y.; Li, D., Modeling of nucleic acid adsorption on 3D prisms in microchannels. *Analytica Chimica Acta* **2007,** *581*, 42-52.

(264) Munson, B. R.; Young, D. F.; Okiishi, T. H., *Fundamentals of fluid mechanics: Student solutions manual*. Wiley: 1998.

(265) Sheehan, P. E.; Whitman, L. J., Detection Limits for Nanoscale Biosensors. *Nano Letters* **2005,** *5*, 803-807.

(266) Arlett, J. L.; Myers, E. B.; Roukes, M. L., Comparative advantages of mechanical biosensors. *Nature Nanotechnology* **2011,** *6*, 203.

Vita

Jianhe Guo was born in Putian, Fujian, China. He received his B.S. degree in Material Chemistry from the University of Science and Technology of China (USTC), China in 2012. He published 1 first authored and 2 co-authored papers during his undergraduate studies. He joined Prof. Donglei Fan's group in the Materials Science and Engineering Program and Department of Mechanical Engineering at the University of Texas at Austin as a graduate student on Ph.D. track in 2012. His research includes design, fabrication and bioapplications of micro/nanomachines, nanosensors, microfluidics, and nanomaterials. He has published 6 first/co-first authored and 7 co-authored journal papers on leading journals, including Nature Communications, ACS Nano, Advanced Functional Materials, Chemistry of Materials, Small, and Nanoscale. He has co-authored 2 book chapters, and co-invented one granted patent and 2 pending patents since joining Prof. Fan's group. He received numerous prestigious awards, including HHMI (Howard Hughes Medical Institute) International Student Research Fellowship, Harris L. Marcus Graduate Fellowship, GRC (Gordon Research Conference) Graduate Student Academic Scholarship, NSF (National Science Foundation) Student Travel Award for ASME NEMB Conference, MRS (Materials Research Society) Symposium Best Poster Award, Graduate Student Assembly Travel Grant Award, four Graduate Student Professional Development Awards, and two Departmental Research Poster Contest Awards from UT Austin.